

**Improving liposomal therapeutic oligonucleotide carriers: from physical design
and characterization to gene silencing and delivery applications**

Joshua O'Grady
Department of Chemistry
McGill University
August 2022

A Thesis submitted to McGill University in partial fulfilment of the requirements of the
degree of
Master of Science

Preface

Intellectual conception and funding for the project presented in this thesis were provided by Professor Nathan Luedtke. Outside of my contributions to the experimental procedures and writing, I would like to thank the following individuals for their contributions to my thesis:

In **Chapter 2**, Dr. William Copp synthesized, purified, and quantified mVG-F fully fluorinated siRNAs for further liposome formulation and characterization. Matthias Thijs aided in liposome formulation and characterization procedures including synthesis of MoChol, microfluidic formulation and RiboGreen RNA quantification. Dr. Amal Seffouh conducted and provided all Cryo-TEM images.

Abstract

The unique properties of the fluorine atom have long been exploited in medicinal chemistry for various purposes. Low polarizability and high polarity of fluorine leads to fluorine-fluorine interactions; a trait that also correlates to perfluorinated compounds. This phenomenon of preferential fluorine-fluorine interaction is termed the **fluorous effect**. While originally used as a purification method based on a triphasic system, this novel characteristic of perfluorinated compounds provides a plethora of opportunity for formation of interactions on the microscopic scale. Our primary goal was to apply this effect to liposomes for oligonucleotide drug delivery in hopes of improving particle physical and functional characteristics. Based on previous literature pertaining to liposomal systems for saRNA delivery, we rationally designed and synthesized several ionizable cholesteryl carbamate derivatives with to be formulated into liposomes. Among these, two were synthesized with varying levels of fluorination to help evaluate the fluorous effect when formulated with unmodified or fully fluorinated siRNA. To observe changes as a result of the fluorous effect, particles were analyzed based on their physical characteristics including effective diameter, polydispersity index, zeta potential, morphology, and RNA encapsulation efficiency. In vitro assessment included observation of uptake by MDA-MB-231 cancer cells and gene silencing using siRNA's for mVenus/GFP knockdown in MDA-MB-231 and MOLM-14 cells. We first showed that the linkage type in this system is interchangeable between carbamate and succinyl types. Liposomes formulated using fluorinated lipids showed particle sizes approximately 30 nm larger than their non-fluorinated counterparts as well as slightly increased polydispersity indices. Fluorinated particles showed comparable zeta potential values but siRNA encapsulation efficiencies 21-25% lower than non-fluorinated liposome samples. Further, our particles showed good uptake and a low toxicity profile. Fluorinated liposomes encapsulating fluorinated siRNA showed negligible changes in any of the aforementioned characteristics, with the exception of increased toxicity. While we were unable to show significant knockdown activity from delivered siRNA cargo, further investigation is required to make conclusions surrounding the delivery efficiency of the developed liposomes. In addition, it was suggested that the low fluorination state

of utilized lipids was not sufficient to generate the desired fluororous phase that we proposed could improve/alter the liposomal properties.

Résumé

Les propriétés uniques de l'atome de fluor ont longtemps été exploitées en chimie médicinale à des fins diverses. La faible polarisabilité et la polarité élevée du fluor entraînent des interactions fluor-fluor; un trait qui est également transféré aux composés perfluorés. Ce phénomène d'interaction préférentielle fluor-fluor est appelé **effet fluoré**. Bien qu'utilisée à l'origine comme méthode de purification basée sur un système triphasique, cette nouvelle caractéristique des composés perfluorés offre une pléthore d'opportunités pour la formation d'interactions à l'échelle microscopique. Notre objectif principal était d'appliquer cet effet aux liposomes pour l'administration de médicaments à base d'oligonucléotides dans l'espoir d'améliorer les caractéristiques physiques et fonctionnelles des particules. Sur la base de la littérature antérieure en référence aux systèmes liposomaux pour la distribution des petits ARN autoactivés, nous avons rationnellement conçu et synthétisé plusieurs dérivés ionisables de carbamate de cholestérol à formuler en liposomes. Parmi ceux-ci, deux ont été synthétisés avec différents niveaux de fluoration pour aider à évaluer l'effet fluoré lorsqu'ils sont formulés avec des petits ARN interférents non modifiés ou entièrement fluorés. Pour observer les changements résultant de l'effet fluoré, les particules ont été analysées en fonction de leurs caractéristiques physiques, notamment le diamètre effectif, l'indice de polydispersité, le potentiel zêta, la morphologie et l'efficacité d'encapsulation de l'ARN. L'évaluation in vitro comprenait l'observation de l'absorption par les cellules cancéreuses MDA-MB-231 et l'extinction génique à l'aide de petits ARN interférents pour l'inactivation de mVenus/GFP dans les cellules MDA-MB-231 et MOLM-14. Nous avons d'abord démontré que le type de liaison dans ce système est interchangeable entre les types carbamate et succinyle. Les liposomes formulés à l'aide de lipides fluorés ont montré des tailles de particules d'environ 30 nm plus grandes que leurs homologues non fluorés ainsi que des indices de polydispersité légèrement augmentés. Les particules fluorées ont montré des valeurs de potentiel zêta comparables, mais des efficacités d'encapsulation de petits ARN interférents de 21 à 25 % inférieures à celles des échantillons de liposomes non fluorés. De plus, nos particules ont montré une bonne absorption et un profil de faible toxicité. Les liposomes fluorés encapsulant des petits ARN interférents fluorés ont montré des changements

négligeables dans l'une quelconque des caractéristiques mentionnées précédemment, à l'exception d'une toxicité accrue. Bien que nous n'ayons pas été en mesure de montrer une activité de renversement significative de la cargaison de petits ARN interférents délivrée, une investigation plus approfondie est nécessaire pour tirer des conclusions concernant l'efficacité de livraison des liposomes développés. De plus, il a été suggéré que le faible état de fluoration des lipides utilisés n'était pas suffisant pour générer la phase fluorée souhaitée qui, selon nous, pourrait améliorer/modifier les propriétés liposomiques.

Acknowledgements

I would first like to express my gratitude to Professor Nathan Luedtke for enabling me to complete my work in his lab while supporting me through my research journey over the past two years. The guidance and advice you have provided during this time played a crucial role in the optimization and progression of this work as we explored a project outside the scope of what the group has done in the past. I can't thank you enough for all you have taught me. Additionally, I would like to thank Professors Hanadi Sleiman and Christopher Thibodeaux for serving on my committee and providing valuable feedback on my project. Thank you to Professor Masad Damha for all the advice you have provided.

During my time at McGill, several individuals have had a positive impact on my experience. I would like to thank Dr. Violeta Toader for sharing her expertise in particle characterization and providing me with the appropriate training to proceed with further experiments. I would also like to thank Robin Stein for training and advice with NMR characterization, as well as Dr. Alex Wahba and Nadim Saadeh for mass spectrometry analysis of my lipid compounds. Thank you to Dr. Amal Seffouh and Professor Joaquin Ortega for the effort and the time you offered to generate the fantastic TEM images. I send my appreciation to Professor McKeague and students in her group including Serhii Hirka, Lucia Wang, Bruktawit Maru and Micaela Belleperche for helping with supplies and providing advice. Thank you to Professor Janine Mauzeroll and Dr. Isabelle Beaulieu for allowing me to carry out many experiments in their cell laboratory and for their facility management. Lastly, I would like to express my appreciation for Chantal Marotte and all the administrative staff in the department for help in navigating various aspects of my degree.

I would like to thank Matthias, Kaleena, Will and Morten, who all took the time to read my thesis and provide valuable feedback. I would also like to thank Alicia Montulet for translating my abstract into French.

While much of my time as a graduate student here was hindered by the ongoing pandemic, I have had the opportunity to meet several spectacular people. Thank you to

Jeremy Dawkins for offering your advice to a new graduate student on the ins and outs on Montreal before I even arrived. When I arrived at McGill in the fall of 2020, I was immediately taken in by the fantastic individuals of both the Luedtke and Damha labs. Kaleena, thank you for all your advice even when you may have been at nerves end. More importantly, thank you for being my person here in Montreal, I truly would have been a struggle without you there with me. To Ashkan, you brought a fun and energetic atmosphere to the lab every day. This coupled with your drive for success was highly contagious. Thank you for laughs and memories we made together over the last few years. To Morten, I greatly enjoyed our consistent banter, enjoying a nice pint and the time we shared together in the lab. I am grateful to have gotten the opportunity to learn from you, especially in the beginning when I was nothing but lost.

This original group eventually expanded to include Will, Kaifeng and John in 2021. I am sincerely appreciative for the time we had together, whether it was in the lab, out for coffee, or at happy hour. Thank you to Will for your interest and tremendous help with my project, and for your companionship in and out of the lab. Thank you, Kaifeng, for all your advice on biological experiments and all of the laughs we had about sus results or reaction eruptions. Thank you to John for offering your help and expertise, as well as your companionship in the lab, and fun times on group outings.

I was fortunate to work alongside several undergraduate students in the lab including Round, Michael, Daria, Ayo, Martin, Muriel, and Katie. Thank you all for your kindness and support. I also had the pleasure of mentoring and working with an undergraduate of my own. Matthias, thank you for being my number two, for your various contributions and just being in my corner. I know you'll be fantastic as you head into graduate studies of your own.

Our group was fortunate enough to work alongside the lab of Dr. Damha. Many of these individuals were of great help and company both in and out of the lab setting. Leo, Ada, Roberto, James, Alicia, Cristina, Halle, Adam and Sunit. Thank you for all contributions, big or small. It has truly been a pleasure to get to know all of you and I cherish the companionship I have found in everyone.

My success as a graduate student would not have been possible without the love and support from my close friends and family. I would like to send my appreciation thank you to Victoria, Stephen, Simon, Abby, Phil, Dave, Chris, Judy, Paolo and Monty. Thank you to my extended family, Maddy, Kate, Stephen, Mandy, Ed, Lana, Courtney, Alison, Shannon and my grandparents for their continuous support throughout my academic career. Lastly, I would like to express my gratitude to my parents and sister. I am forever indebted to you, and I know with 100% certainty that I could never have done it without having you in my corner.

List of Figures

Figure 1.1. Illustration of the cellular RNAi process. Upon entry into the cell, siRNAs are recognized by AGO2 to facilitate the formation of the RISC. The complex then targets specific mRNA transcripts for degradation and is recycled to repeat this process such that gene expression is ultimately inhibited. Figure reprinted with permission from Whitehead et al. [15] with an appropriate copyright licence.....	3
Figure 1.2. Mechanism of saRNA mediated RNA activation. (1) import of saRNA into the cytoplasm. (2) cleavage of saRNA passenger strand and nuclear import. (3) assembly of the saRNA-Ago2 and PAF1 complex to the promoter region to facilitate transcription initiation. (4) export of messenger RNA and subsequent protein production via translation. Figure reprinted from Kwok et al, 2019, [21] under the creative commons attribution license.	5
Figure 1.3. Selected examples of base, linkage, and sugar modifications applicable to therapeutic oligonucleotides.	8
Figure 1.4. Illustration of the various unilamellar and multilamellar liposomes.	11
Figure 1.5. Illustration depicting the various modifications applicable to liposomal systems. Comparison of conventional liposomes, (A) containing only their respective cationic and anionic lipid components with other systems that are PEGylated, (B) or functionalized with other various agents (C) such as aptamers, antibodies, proteins, peptides, carbohydrates or other small molecules. This figure has been modified from Sercombe et al. [46] and reprinted under the creative commons attribution 4.0 licence. Image was constructed using BioRENDER™	12
Figure 1.6. Illustration outlining the process of liposomal endosomal escape. After endocytotic uptake (A), the maturation and associated acidification of the endosome leads to the release of internalized cargo. Figure adapted from Degors et al. [59] under the creative commons attribution license	14
Figure 1.7. Structures of lysophosphatidylcholine occupying a conical shape (top), palmitoyl-2-oleoyl-sn-glycero-3-phosphocholine (POPC) occupying a cylindrical shape (middle) and DOPE occupying an inverted conical shape (bottom). Figure adapted with permission from Karanth et al. [63] with an appropriate copyright licence (Oxford University Press).	16
Figure 1.8. Illustration of the endosomal escape process according to the transient pore model. (A) lipid-based vehicle and endosomal membrane in close proximity, which leads to (B) electrostatic interaction and rearrangement of lipids between the two respective membranes and the delivery vehicle begins its dissociation. This leads to the formation of a pore in the endosomal membrane (C), allowing the nucleic acid cargo to escape into the cytosol (D). Figure reprinted and adapted from Degors et al. [59] under the creative commons attribution license.....	17

Figure 1.9. Illustration of lipid shape as it pertains to higher order membrane structure. The natural cylindrical nature of some lipids results in the formation of a bilayer. The electrostatic interaction with their oppositely charged counterparts supports the formation of an inverted hexagonal phase, which can lead to pore formation during the endosomal escape process, allowing for cargo release. Figure adapted with permission from Semple et al [68] and an appropriate copyright licence.....	18
Figure 2.1. Illustration depicting the utilized liposome formulation process. (A) siRNA of sequence in combination with lipids in ethanol using the 6:24:47:23 ratio. (B) Microfluidic mixing of RNA in aqueous solution and lipids in ethanol followed by subsequent rapid pH adjustment. (B) Extrusion of liposomal solution through 0.2 μ m polycarbonate filters. (D) Dialysis of liposomal solution to facilitate buffer exchange. Components of this figure were printed from BioRENDER™	25
Figure 2.2. Lognormal distribution of particle diameter measurements for liposomes containing the MCLM (2, left) or the MoChol (8, right) lipids (Figure S21, S22). Data are plotted as effective diameter (nm) vs scattering intensity. Measurements were obtained using the NanoBrook OMNI (Brookhaven Instruments) and data were transformed using the CONTIN algorithm for size distribution.	26
Figure 2.3. Cryo-TEM microscopy images of liposomal samples based on (A) MCLM (2), (B) MoChol (8), (C) MCLF (4), and (D) MCLH (5). (E) Commercial NOV340 liposomes. (F) Moderna mRNA liposomal formulation against SARS-CoV2. (G) Doxove liposomes encapsulating doxorubicin.....	30
Figure 3.1. (A) Fluorescence spectra of irradiated and non-irradiated samples of the light catalyzed crosslink reaction (B) 15% polyacrylamide denaturing gel images showing ethidium bromide (lanes 1 and 2), and SYBR Gold (lanes 3 and 4) intensities. Lanes 1 and 3 show non-purified samples while lanes 2 and 4 show spin column treated, irradiated samples.	36
Figure 3.2. Confocal microscopy images showing the presence of eGFP (green) and distribution of EMA-tRNA formulated liposomes (magenta) in MDA-MB-231 cells. Images were obtained using a 488 nm laser for eGFP and 561 nm laser for ethidium bromide detection.....	37
Figure 3.3. Zoomed confocal microscopy images of the merged channel showing (A) untreated, (B) MCLM-based liposome, (C) MoChol-based liposome, and (D) MCLF-based liposomes encapsulating EMA-tRNA. eGFP fluorescent signal is presented in green and modified fluorescent tRNA is presented in magenta. Images were obtained using a 488 nm laser for eGFP and 561 nm laser for ethidium bromide detection.....	38
Figure 3.4. Gene knockdown efficiency of MCLF-based liposomes encapsulating mVG siRNA. Fluorescence (RFU) measurements for (A) mVenus expressing MOLM-14 cells and (B) eGFP expressing MDA-MB-231 cells taken 72 hours post-incubation with siRNA encapsulated liposomes. Fluorescence was measured at 530 nm for both cell lines and error bars represent S.E.M. Fluorescence for mVenus (MOLM-14) was measured at excitation: 480 nm, emission: 500-620 nm, cutoff: 515 nm, while eGFP	

(MDA-MB-231) was measured at excitation: 460 nm, emission: 500-600 nm, cutoff: 495 nm.....40

Figure 3.5. Toxicity of MCLF-based liposomes encapsulating mVG siRNA.

Fluorescence (RFU) measurements for the resazurin assay of (A) mVenus expressing MOLM-14 cells and (B) eGFP expressing MDA-MB-231 cells taken 76 hours post-incubation with siRNA encapsulated liposomes. Fluorescence values are taken at 595 nm. Resorufin fluorescence excitation: 560 nm, emission: 575-700 nm, and cutoff: 590 nm.....41

Figure 3.6. Fluorescence (RFU) measurements for (A) mVenus expressing MOLM-14 cells taken 72 hours post-incubation with siRNA encapsulated liposomes containing the MCLM, MoChol and MCLF ionizable lipids, (B) resorufin fluorescence as a function of cell viability. Samples marked with “-F” are indicative of liposomes encapsulating mVG-F siRNA with unmarked samples encapsulating mVG siRNA. Fluorescence was measured at 530 nm for mVenus and 595 nm for resorufin. Error bars represent S.E.M. Fluorescence for mVenus (MOLM-14) was measured at excitation: 480 nm, emission: 500-620 nm, cutoff: 515 nm, resorufin fluorescence excitation: 560 nm, emission: 575-700 nm, and cutoff: 590 nm.....42

Figure 3.7. Cellular toxicity measurements using each synthesized lipid and encapsulating tRNA. Fluorescence (RFU) measurements for (A) mVenus expressing MOLM-14 cells taken 72 hours post-incubation (B) resorufin fluorescence 76 hours post-incubation as a function of cell viability. Fluorescence was measured at 530 nm for mVenus and 595 nm for resorufin. Error bars represent S.E.M. Fluorescence for mVenus (MOLM-14) was measured at excitation: 480 nm, emission: 500-620 nm, cutoff: 515 nm, resorufin fluorescence excitation: 560 nm, emission: 575-700 nm, and cutoff: 590 nm.43

Figure S1. ¹H NMR (500 MHz, CDCl₃) for MCLM (2).....55

Figure S2. ¹³C NMR (126 MHz, CDCl₃) for MCLM (2).55

Figure S3. ¹H NMR (500 MHz, CDCl₃) for MCLP (3).56

Figure S4. ¹³C NMR (126 MHz, CDCl₃) for MCLP (3).56

Figure S5. ¹H NMR (500 MHz, CDCl₃) for MCLF (4).....57

Figure S6. ¹³C NMR (126 MHz, CDCl₃) for MCLF (4).57

Figure S7. ¹⁹F NMR (471 MHz, CDCl₃) for MCLF (4).....58

Figure S8. ¹H NMR (500 MHz, CDCl₃) for MCLH (5).58

Figure S9. ¹³C NMR (126 MHz, CDCl₃) for MCLH (5).....59

Figure S10. ¹⁹F NMR (471 MHz, CDCl₃) for MCLH (5).59

Figure S11. ¹H NMR (500 MHz, CDCl₃) for MCLB (6).60

Figure S12. ¹³C NMR (126 MHz, CDCl₃) for MCLB (6).....60

Figure S13. ¹H NMR (500 MHz, CDCl₃) for MoChol (8).61

Figure S14. ^{13}C NMR (126 MHz, CDCl_3) for MoChol (8).	61
Figure S15. Deconvoluted HRMS spectrum for MCLM (2). Data was collected and analyzed by Dr. Alexander Wahba (McGill University).	62
Figure S16. Deconvoluted HRMS spectrum for MCLP (3). Data was collected and analyzed by Dr. Alexander Wahba (McGill University).	62
Figure S17. Deconvoluted HRMS spectrum for MCLF (4). Data was collected and analyzed by Dr. Alexander Wahba (McGill University).	62
Figure S18. Deconvoluted HRMS spectrum for MCLH (5). Data was collected and analyzed by Dr. Alexander Wahba (McGill University).	63
Figure S19. Deconvoluted HRMS spectrum for MCLB (6). Data was collected and analyzed by Nadim Saadeh (McGill University).	63
Figure S20. Deconvoluted HRMS spectrum for MoChol (8). Data was collected and analyzed by Dr. Alexander Wahba (McGill University).	63
Figure S21. MCLM-based liposome particle sizing lognormal distribution (left) and correlation function (right).	64
Figure S22. MoChol-based liposome particle sizing lognormal distribution (left) and correlation function (right).	64
Figure S23. MCLF-based liposome particle sizing lognormal distribution (left) and correlation function (right).	65
Figure S24. MCLH-based liposome particle sizing lognormal distribution (left) and correlation function (right).	65
Figure S25. Analytical HPLC trace of unmodified siRNA sense strand Sense: 5'-GCACGACUUCUUCAAGUCCGCCA[dT][dT]-3'.	66
Figure S26. Analytical HPLC trace of unmodified siRNA antisense strand 5'-phos-UGGCGGACUUGAAGAAGUCGUGC[dT][dT] - 3'.	66
Figure S27. Analytical HPLC trace of fluorinated sense strand 5'-GCACGACUUCUUCAAGUCCGCCA[dT][dT]-3'.	67
Figure S28. Analytical HPLC trace of fluorinated antisense strand 5'-phos-UGGCGGACUUGAAGAAGUCGUGC[dT][dT] - 3'.	67
Figure S29. MS spectrum (ESI: MS-IALTQ-05) for unmodified siRNA sense strand 5'-GCACGACUUCUUCAAGUCCGCCA[dT][dT]-3'. Spectrum provided by ID T.	68
Figure S30. MS spectrum (ESI: MS-IALTQ-05) for unmodified siRNA antisense strand 5'-phos-UGGCGGACUUGAAGAAGUCGUGC[dT][dT] - 3'. Spectrum provided by ID T.	68
Figure S31. HRMS (ESI) of fluorinated siRNA sense strand 5'-GCACGACUUCUUCAAGUCCGCCA[dT][dT]-3'. Data was collected and analyzed by Dr. Alexander Wahba (McGill University).	68

Figure S32. Deconvoluted HRMS (ESI) of fluorinated siRNA antisense strand 5'-phos-UGGCGGACUUGAAGAAGUCGUGC[dT][dT] - 3'. Spectrum shows the presence of potassium adducts in the gas phase. Data was collected and analyzed by Dr. Alexander Wahba (McGill University)	69
Figure S33. Standard curve for unmodified siRNA duplex generated using the RiboGreen Assay. Values are plotted concentration (µg/mL) vs fluorescence (RFU) at 530 nm.	69
Figure S34. Standard curve for fluorinated siRNA duplex generated using the RiboGreen Assay. Values are plotted concentration (µg/mL) vs fluorescence (RFU) at 530 nm.	69
Figure S35. Standard curve for unmodified tRNA generated using the RiboGreen Assay. Values are plotted concentration (µg/mL) vs fluorescence (RFU) at 530 nm.	70
Figure S36. Standard curve for EMA-modified tRNA generated using the RiboGreen Assay. Values are plotted concentration (µg/mL) vs fluorescence (RFU) at 530 nm.	70

List of Tables

Table 1.1. Composition of the MTL-CEBPA liposomal and saRNA formulation. [71]	19
Table 2.1. Comparison of particle characteristics between MCLM and MoChol-based liposomes using mVG siRNA.	27
Table 2.2. Comparison of liposome characteristics encapsulating mVG siRNA, using each of the synthesized lipids.	29
Table 2.3. Comparison of particle characteristics between MCLM, MoChol and MCLF-based liposomes encapsulating mVG or mVG-F siRNA.	33
Table S37. DLS, PALS and encapsulation data for control liposomes encapsulating tRNA.....	70

List of Schemes

Scheme 1. Synthesis of MCLM (2) (Figure S1, S2, S15).	22
Scheme 2. Synthesis of MCLP (3) (Figure S3, S4, S16)	22
Scheme 3. Synthesis of MCLF (4) (Figure S5, S6, S7, S17).	23
Scheme 4. Synthesis of MCLH (5) (Figure S8, S9, S10, S18).	23
Scheme 5. Synthesis of MCLB (6) (Figure S11, S12, S19).....	23
Scheme 6. Synthesis of MoChol (8) (Figure S13, S14, S20).	23
Scheme 7. Conversion of resazurin to resorufin from reduction by NADH during cellular respiration in the mitochondria	39

Table of Contents

Preface.....	2
Abstract.....	i
Résumé.....	iii
Acknowledgements.....	v
List of Figures	viii
List of Tables.....	xiii
List of Schemes.....	xiv
List of Abbreviations.....	xvii
1. Introduction	1
1.1. Therapeutic oligonucleotides.....	1
1.1.1. siRNA mediated gene silencing	1
1.1.2. saRNA mediated gene activation	4
1.1.3. Barriers to the development of oligonucleotide therapeutics.....	6
1.1.4. Therapeutic oligonucleotide modifications	7
1.2. Lipid-based therapeutic drug carriers	9
1.2.1. Liposomes and their composition.....	9
1.2.2. Physical and functional characterization	10
1.2.3. Potential barriers in liposomal development	12
1.2.4. Liposome modifications	12
1.2.5. Mechanism of action.....	14
1.3. pH-sensitive liposomal systems.....	15
1.3.1. Dioleoylphosphatidylethanolamine (DOPE).....	16
1.3.2. Cationic amphiphiles.....	17
1.3.3. NOV340	19
1.4. The fluoruous effect	20
2. Development and characterization of pH-sensitive liposomes for encapsulation of oligonucleotide cargo.....	22
2.1. Design and characterization of cationic lipids	22
2.1.1. Rationale and objectives	22
2.1.2. Synthesis and characterization of lipid candidates	22
2.2. Liposomal formulation and Characterization	24
2.2.1. Rationale and objectives	24
2.2.2. Comparison of carbamate and succinyl linkages in cationic amphiphiles.....	26

2.2.4.	Evaluation of the fluorous effect through the use of fluorinated siRNA	33
3.	In vitro assessment of liposomal formulations.....	35
3.1.	Liposome uptake studies	35
3.1.1.	Rationale and objectives	35
3.1.2.	Synthesis of fluorescently labelled tRNA	35
3.1.3.	Visualization of liposome uptake by confocal microscopy	37
3.2.	Knockdown and toxicity assessment of liposome formulations	39
3.2.1.	Rationale and objectives	39
3.2.2.	siRNA knockdown and liposomal toxicity assessment	39
3.3.	Conclusions and future perspectives.....	44
4.	Experimental	46
5.	Supplementary information.....	55
6.	References.....	71

List of Abbreviations

Word or phrase	Abbreviation
6'-phenylpyrrolo cytosine	PhpC
Acetonitrile	ACN
Acute myeloid leukemia	AML
Antisense oligonucleotide	ASO
Argonaute	AGO
carbon catabolite repression 4-negative on TATA-less	CCR4-NOT
C-C chemokine receptor type 4	CCR4
CCAAT enhancer-binding protein alpha	CEBP α
Cholesteryl hemisuccinate	CHEMS
Composite autonomic symptom score	COMPASS
Deoxyribonucleic acid	DNA
Dichloromethane	DCM
Dioleoyl phosphatidylethanolamine	DOPE
Double stranded	ds
Dynamic light scattering	DLS
Enhanced green fluorescent protein	eGFP
Enhanced permeability and retention	EPR
Ethidium bromide monoazide	EMA
Giant unilamellar vesicle	GUV
Hereditary variant transthyretin amyloidosis	ATTRv
High resolution mass spectrometry	HRMS
Histone modifying proteins	HMP
Large unilamellar vesicle	LUV
Low-density lipoprotein receptor	LDLR
Mediator proteins	MED
Messenger RNA	mRNA
Methoxyethyl	MOE
Micro RNA	miRNA
Modified neuropathy impairment score	mNIS
Multilamellar vesicle	MLV
Multivesicular vesicle	MVV
Nuclear magnetic resonance	NMR
palmitoyl-2-oleoyl-sn-glycero-3-phosphocholine	POPC
Perfluorinated compounds	PFC
Phase analysis light scattering	PALS
Phosphorothioate	PS
Polyethylene glycol	PEG
Polymerase associated factor 1	PAF1
Polymerase chain reaction	PCR

Quality of life-diabetic neuropathy	QOL-DN
Quantitative polymerase chain reaction	qPCR
Reticuloendothelial system	RES
Ribonucleic acid	RNA
RNA activation	RNAa
RNA helicase A	RHA
RNA induced silencing complex	RISC
RNA induced transcriptional activation complex	RITA
RNA interference	RNAi
RNA polymerase II	RNAPII
Short activating RNA	saRNA
Short interfering RNA	siRNA
Single stranded oligonucleotide	SSO
Small unilamellar vesicle	SUV
Sodium acetate	NaOAc
Toll-like receptor 8	TLR8
Trans-activation response RNA binding protein	TRBP
Transfer RNA	tRNA
Trinucleotide repeat containing adaptor 6A	TNRC6A
US Food and Drug Administration	FDA

1. Introduction

1.1. Therapeutic oligonucleotides

Oligonucleotides are polymers of varying length, composed of nucleoside units, that come in the form of DNA or RNA. These molecules have been widely studied in the context of therapeutics. This is predominantly due to the ability of these molecules to be rationally designed to target a specific base sequence. Consequently, oligonucleotides can provide certain advantages over traditional small molecule therapeutic drugs such as simple programmability. This field has seen the development of various types of nucleic acid therapeutics including antisense oligonucleotides (ASO's), short interfering RNAs (siRNAs), short activating RNAs (saRNAs), messenger RNAs (mRNAs), and aptamers. Currently, 15 oligonucleotide drugs have been approved by the FDA. This list includes ASO's that treat hypercholesterolaemia, hereditary transthyretin amyloidosis (hATTR) with polyneuropathy, and Duchenne muscular dystrophy, [1,2], siRNAs for hATTR, acute hepatic porphyria, hyperoxaluria type 1, and hypercholesterolaemia, [1,2] an aptamer treating neovascular macular degeneration, and more recently mRNAs as Covid-19 vaccines. [2,3] The traction gained by oligonucleotide drugs in the clinical setting since the early 2000's remains impressive and speaks to their potential for future developments.

1.1.1. siRNA mediated gene silencing

siRNA's are short, duplex RNA composed of a sense (passenger) and antisense (guide) strand and have enabled significant advancement in precision therapeutics. These macromolecules are approximately 21 base pairs in length with 2 nucleotide 3' overhangs. They have widely been used for the modulation of gene expression by a mechanism known as RNA interference (RNAi). [4] This mechanism was initially observed in *C. elegans*. [5] This work by Fire et al. in 1998 showed that the introduction of an exogenous RNA duplex can silence gene expression in vivo through antisense targeting of mRNA. [5] In 2001, Elbashir et al. showed that this mechanism is also active in mammalian cell cultures by targeted, endogenous silencing. [6] Further studies on this mechanism have revealed several of the critical cellular machineries responsible

for RNAi which included, the RNA induced silencing complex (RISC) and argonaute (AGO) proteins. [7,8]

The RNAi process may proceed by endogenous micro-RNAs (miRNAs) or exogenously introduced double stranded RNAs or siRNAs. The first step of gene silencing is the uptake of double stranded RNA (dsRNA) or siRNA into the cell by endocytosis. [9,10] Upon release from the late endosomes, the duplexes are bound to and sometimes cleaved by the dicer protein. [9,11] Progression beyond this point may be Dicer dependent or independent. [9,12,13] If the introduced sequence is longer than 21 base pairs then it may be subject to Dicer processing. [9] In either case, the RNA then becomes incorporated into the RISC loading complex (RLC) which consists of Dicer, transactivation response element RNA-binding protein (TRBP) and one of the four AGO proteins. [9,14] Here, a strand selection step will occur, resulting in the cleavage of the passenger (sense) strand, leaving the guide (antisense) strand bound to AGO. [9,10] This strand may then guide the RLC to mRNA strands for which the siRNA has been rationally designed. Selective hybridization of the guide strand to mRNA by traditional Watson-Crick base pairing leads to the recruitment of the remaining proteins that compose the mature RISC. [9] The slicer activity of AGO2 leads to the degradation of the mRNA sequence, resulting in the inhibition of subsequent protein expression. [9,10]. The complex may then proceed in targeting other mRNA molecules in multiple turnovers.

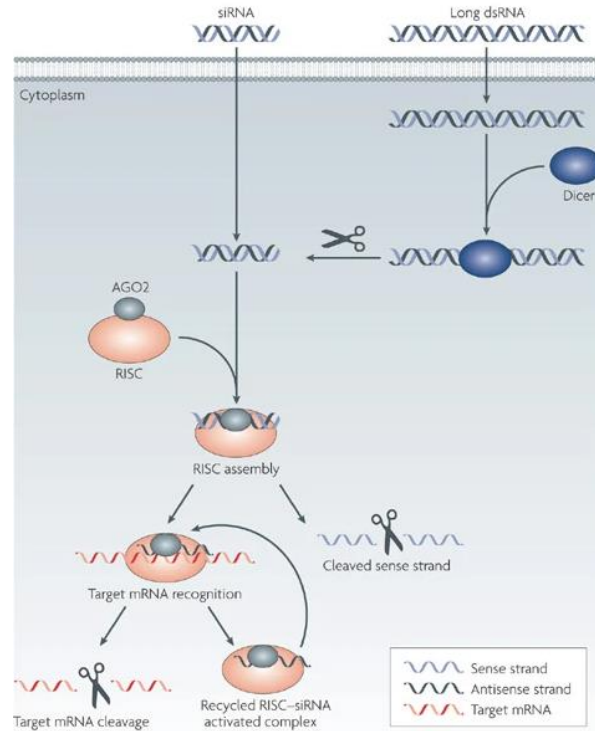


Figure 1.1. Illustration of the cellular RNAi process. Upon entry into the cell, siRNAs are recognized by AGO2 to facilitate the formation of the RISC. The complex then targets specific mRNA transcripts for degradation and is recycled to repeat this process such that gene expression is ultimately inhibited. Figure reprinted with permission from Whitehead et al. [15] with an appropriate copyright licence.

Perhaps one of the most significant advancements in the field of siRNA therapeutics was the development of patisiran (Onpattro) by Alnylam Therapeutics. This drug was developed for the treatment of polyneuropathy caused by hereditary variant transthyretin amyloidosis (ATTRv) and was the first of its kind to gain regulatory approval. Patisiran was designed to selectively target the mutated transthyretin (TTR) gene which encodes for ATTRv that carries an amino acid substitution. This mutation allows the TTR dimer protein to readily dissociate, leading to amyloidosis and subsequent polyneuropathy. [16] Throughout the span of the various stages of clinical testing, a reduction in TTR levels was associated with the 56.1% of patients who showed improvement of their modified neuropathy impairment (mNIS+7) scores. This scale was used to measure patients overall neurological impairment and included evaluation of various bodily nerves, sensory testing, and other factors. In addition, Norfolk quality of life-diabetic neuropathy (QOL-DN) and composite autonomic symptom score (COMPASS-31) scales were used to evaluate improvement of neuropathy. [16] In

both analyses, those who were treated with patisiran exhibited improvement that was statistically significant when compared to their respective baseline scores.

The approval of patisiran made a significant impact on the area of siRNA development. Since the time of its approval, the interest in siRNA development has increased significantly. The field has rapidly broadened to include targeting of different cancer types and various diseases, many of which are thought to have cancer-driving mutations that generate “undruggable” and aberrant proteins that can not be effectively targeted with small-molecule inhibitors or therapeutic antibodies.

1.1.2.saRNA mediated gene activation

saRNAs share many of the same characteristics as siRNA's and can be prepared as ~21 nucleotide duplex RNA containing 2 nucleotide overhangs on the 3' end of the sense and antisense strands. Contrary to siRNA, saRNA acts as a regulator of gene expression by a process termed RNA activation (RNAa). The idea of RNAa was originally proposed in the late 1960s but it wasn't until the early 2000's that Li et al. demonstrated that gene promoter targeted dsRNA sequences could activate gene expression by inducing transcription of p21^{WAF1/CIP1}. This was accomplished by targeting non-CpG sequences laying 215 and 302 bp upstream of the putative transcriptional start site. [17,18] In studies being conducted in parallel by Corey et. al expression of the low-density lipoprotein receptor (LDLR) gene was activated by targeting sequences. [19,20] Most recently, the very first saRNA therapeutic candidate to research clinical trails entered phase II for the treatment of hepatocellular carcinoma (HCC) [NCT04710641].

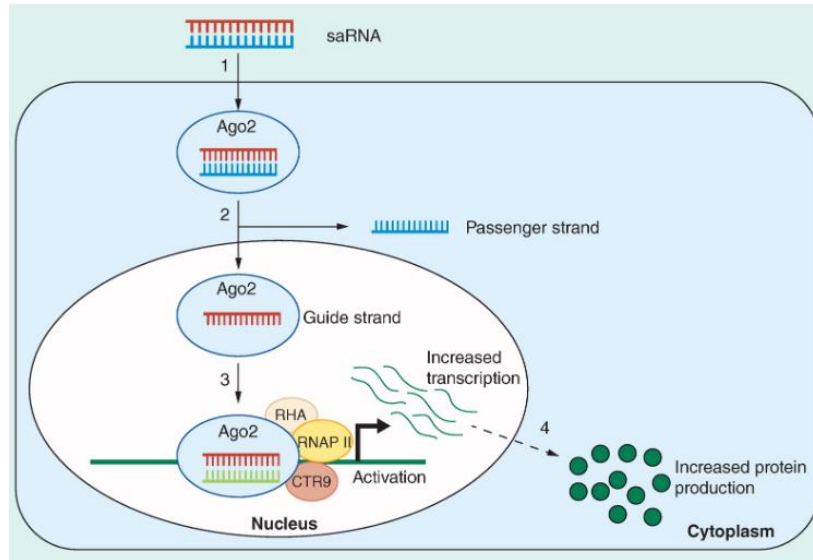


Figure 1.2. Mechanism of saRNA mediated RNA activation. (1) import of saRNA into the cytoplasm. (2) cleavage of saRNA passenger strand and nuclear import. (3) assembly of the saRNA-Ago2 and PAF1 complex to the promoter region to facilitate transcription initiation. (4) export of messenger RNA and subsequent protein production via translation. Figure reprinted from Kwok et al, 2019, [21] under the [creative commons attribution license](#).

The RNAa pathway proceeds in four main steps. A rationally designed, chemically synthesized saRNA sequence is recognized by AGO2 and subsequently loaded in a similar fashion to siRNAs in the RNAi pathway, where the passenger (sense) strand is removed. This complex is then imported into the nucleus by importin-8, [22] where it may target promoter regions, antisense transcripts, and/or long non-coding RNA transcripts outside the promoter region. [17,21,23]. Upon binding of AGO2-saRNA to the desired target DNA, it is met by RNA helicase A (RHA), and the polymerase associated factor 1 (PAF1) complex consisting of PAF1, CTR9 and RNA polymerase II (RNAPII). This newly formed complex is denoted as the RNA induced transcriptional activation complex (RITA). [9,10,21] RITA formation is thought to be accompanied by the binding of TNRC6A to AGO2 which recruits histone modifying proteins (HMPs), mediator (MED) and carbon catabolite repression 4-negative on TATA-less (CCR4-NOT) proteins. [9,10,24] These proteins facilitate chromatin release such that RNA helicase may unwind the DNA as a first step of transcription initiation. [9] Once this large, intricate complex has formed, transcription initiation may begin to result in increased expression of the targeted gene.

The saRNA formulation MTL-CEBPA being developed by MiNA Therapeutics is the first RNAa therapeutic candidate to reach clinical trials. It was designed to target and upregulate the CCAAT enhancer-binding protein alpha (CEBP α) gene. CEBP α is a basic-leucine zipper protein that acts as a transcription factor, playing a vital role in the regulation of proliferation on various tissues including the liver, adipose tissue, and myeloid system. [25,26,27] The initial transfection of the CEBP α -saRNA into hepatoblastoma cells resulted in a greater than 2-fold increase in CEBP α expression according to quantitative polymerase chain reaction (qPCR) analysis. [27] CEBP α can act to activate albumin expression that was found to be elevated upon saRNA transfection. A 50% decrease in cell proliferation was also observed. [27] Application of MTL-CEBPA to rat models revealed downregulation of several protein factors along with upregulation of CEBP α and albumin associated with improved liver function. [27] This study represented an important step towards its current phase II clinical trial [NCT04710641].

1.1.3.Barriers to the development of oligonucleotide therapeutics

Although oligonucleotides serve as a promising alternative to small molecule drugs, they are not without their challenges. Arguably, one of the largest barriers to these therapeutics arises from ribonuclease activity when applied in vivo. Ribonucleases are an extremely diverse class of enzymes that catalyze the degradation of RNA through the cleavage of the phosphodiester linkage. [28] Their nucleolytic activity can either be exo- or endo-, meaning the target oligonucleotide is degraded either externally or internally respectively. The mechanism of this process involves the nucleophilic attack of the phosphorous atom of the linkage, leading to cleavage at either the 3' or 5' end. [28] A typical nucleophile for this reaction is water that is activated through deprotonation and is commonly coordinated with one or two metal ions — such as Mg²⁺ or Ca²⁺ — due to their prominence in the cell. Other nucleophiles may include 2' hydroxyl groups of ribonucleotides, or amino acid side chains. [28,29,30]

Apart from nuclease susceptibility, issues associated with biodistribution, cellular uptake and clearance by the reticuloendothelial system have presented as barriers for oligonucleotide therapeutics. [31,32] Through the continuous development of these

therapeutics, several methods have been employed to address these barriers, with oligonucleotide modifications and delivery systems being the most prominent.

1.1.4. Therapeutic oligonucleotide modifications

The first step in the amelioration of oligonucleotide functional and protective properties is through the introduction of modifications. These modifications may be made to the three main components of an oligonucleotide: the phosphodiester linkage, the deoxyribose/ribose sugar, or the nucleobase. While many of these modifications are applicable to a broad range of oligonucleotide therapeutics, those that are primarily applicable to dsRNA molecules will be discussed here.

Modification of the oligonucleotide backbone has been shown to increase the molecule's nuclease resistance. These modifications involve replacing the linkage completely or just the non-linkage oxygen atoms. [33] A prominent example of this is the replacement of the phosphodiester linkage with a phosphorothioate (PS) linkage. [34] This linkage can be denoted as either PS1 or PS2 where one or both non-linker oxygen atoms are replaced by a sulfur atom, respectively. [33,34] Because of the enhanced nuclease resistance, the circulation lifetime of the oligonucleotide is greatly increased, which is advantageous in the context of its activity. [32-34] This modification, however, can reduce the binding efficiency of the oligonucleotide to its respective target. Consequently, it is often integrated in combination with traditional phosphodiester linkages and is often found at the termini of the oligonucleotide. [33,34]

The nucleobase may also serve as a target for modification. This may occur through the addition of groups to the canonical DNA/RNA bases or substitution of the base with a base mimic. Common examples include pseudouridine base mimic or the modified 2'-thiouridine. [34] Less commonly, N-ethylpiperidine triazole modified adenine analogs have been shown to reduce the immunogenicity of an siRNA by disrupting interactions with TLR8. [34,35] Further, a 6'-phenylpyrrolo cytosine (PhpC) may also be introduced, which has shown to be highly fluorescent. This characteristic enables its use for observation of cellular uptake and tracking, without sacrificing the biological activity of

the siRNA. It also maintains appropriate thermal stability of the molecule when integrated into a siRNA duplex. [34]

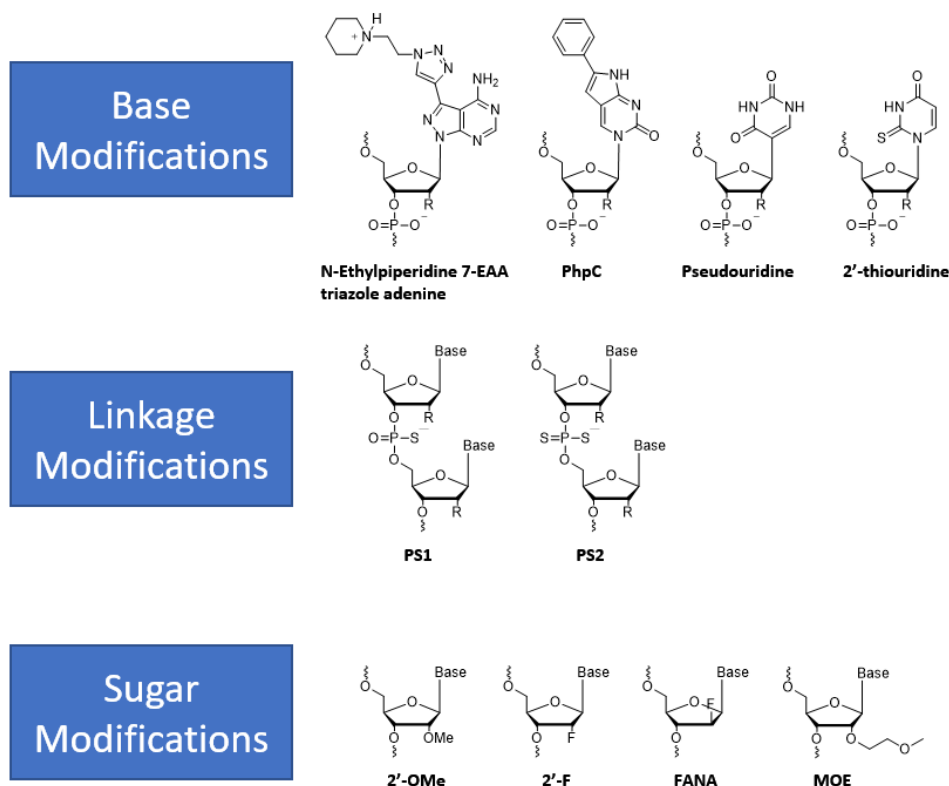


Figure 1.3. Selected examples of base, linkage, and sugar modifications applicable to therapeutic oligonucleotides.

One of the main contributing factors of nuclease degradation of therapeutic oligonucleotides is the 2' hydroxyl group of the ribose sugar. The 2'-OH group may serve as a nucleophile in the process of RNase A catalyzed degradation. [36] Replacement of this group with another atom or ligand has proved to be effective in protecting the RNA molecule from this mechanism of degradation, while also maintaining activity, even in combination with other modifications. [37] With respect to siRNA's, common modifications at this position have included OMe, MOE, fluorine (either 2' F or FANA). [37,38,39] Because the 2'-OH is no longer present, it cannot be deprotonated by a basic residue of the nuclease to then attack the phosphorous. Resultingly, the sessile bond between the phosphorous and either the 5' or 3' oxygen remains intact. [36]

In addition to the aforementioned backbone, base and sugar modifications, addition of a phosphate group to the 5' end of a siRNA antisense strand has become increasingly common. [33] Phosphorylation of siRNA during the RNAi process is pertinent to activity however, not all siRNA sequences are recognized by kinase proteins due to their modifications. [33,40] Many have thus turned to introducing this modification synthetically, such that the risk of decreased activity is avoided.

1.2. Lipid-based therapeutic drug carriers

Lipid-based drug delivery systems (LBDDS) are lipid-containing, nanoscale, colloidal particles used for the delivery of therapeutics with solubility issues or susceptibility to in vivo degradation. In the mid 1960's, Bangham et al. reported observation of particles possessing a lipid bilayer surrounding an aqueous core. This discovery was the first of its kind and ultimately described the particles used today, commonly known as liposomes. [41] In an effort to broaden the applications and functions of this preliminary system, various lipid-based delivery systems have been developed including solid lipid nanoparticles, nanostructured lipid carriers, lipoplexes, and lipid-polymer hybrid nanoparticles. LBDDS's have continued to show their practicality in modern medicine, first with the FDA approval of Doxil® (Janssen) for the treatment of myeloma in the 1990s, [42] Onpattro® (Alnylam) for the treatment of hereditary transthyretin-mediated amyloidosis, [43] and more recently, mRNA vaccines developed by Pfizer and Moderna against SARS-CoV-2. [44] When considering oligonucleotide therapeutics, their success is hindered by several factors including non-specific interactions with in vivo proteins, recognition by the immune system and an inability to passively diffuse across the cell membrane. [45] This is owed to the fact that oligonucleotides are hydrophilic and possess a negative charge. [45] As such, LBDDS can serve as a viable solution as the popularity of oligonucleotide drugs rapidly increases.

1.2.1. Liposomes and their composition

Liposomes are small, uni- or multilamellar vesicles composed of a multicomponent lipid bilayer, with a hydrophilic, aqueous core. [46] These nano/microscale particles may be designed with varying characteristics and sizes based on the lipid composition, lipid

ratios, and formulation method. Liposomes are generally comprised of amphiphilic phospholipids, sphingolipids, sterols, and derivatives thereof, but may also include species such as surfactants, polysaccharides, or glycolipids. [46,47,48] Commonly used phospholipids include various types of phosphatidylcholines or phosphatidylethanolamines that may arise from different natural sources or chemical synthesis. Further, the most prominent example from sphingolipids is sphingomyelin and cholesterol from the sterol category. [48]

Liposomes possess several properties which have given them a reputation as safe and effective drug carriers. The use of amphiphilic lipids in the liposomal bilayer creates a hydrophilic core and a lipophilic membrane. This implies that these particles are capable of encapsulating hydrophilic drugs in the aqueous core or hydrophobic drugs in the non-polar lipid bilayer. [46] Liposomes also offer the versatility to be modified such that they may be targeted to specific systems and attenuate certain disadvantages they have. While there are some exceptions, liposomes are generally considered to be non-toxic, owing to the use of biocompatible components in their formulation. [48] The collective contribution of these advantages makes liposomes a highly competitive drug delivery vehicle in modern therapeutic development.

1.2.2. Physical and functional characterization

As previously stated, liposomes may come in many different sizes and compositions. Their size characteristics can be broken down into two categories: unilamellar (one lipid bilayer) and multilamellar (more than one lipid bilayer). Within the unilamellar category, there are three types: small unilamellar vesicles, large unilamellar vesicles, and giant unilamellar vesicles with diameter ranges of 20-200 nm for SUV, 200 nm to 1 μm for LUV, and $>1 \mu\text{m}$ for GUV respectively. [47] The second category contains multilamellar vesicles and multivesicular vesicles ranging in size from approximately 500 nm to 5 μm in diameter. MLV's have a "particle within a particle within a particle" characteristic whereas MVV's are a singular particle with multiple vesicles inside. [47]

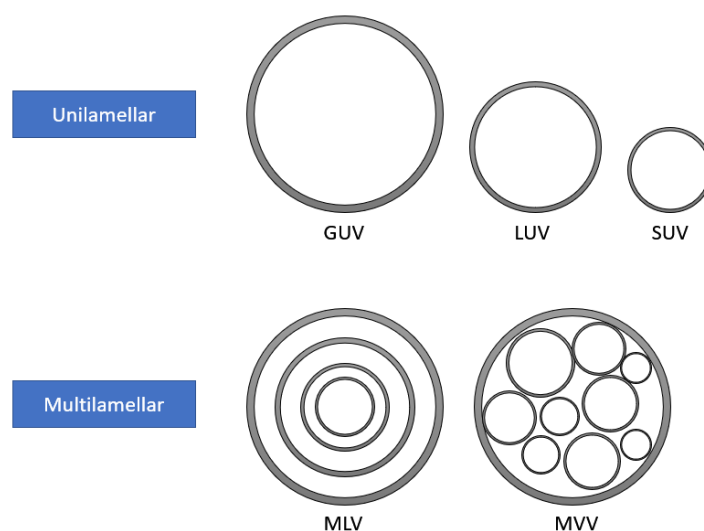


Figure 1.4. Illustration of the various unilamellar and multilamellar liposomes.

Apart from size, liposomes may be classified based on other functional properties, such as charge. Conventional liposomes are composed of various charged and/or neutral (zwitterionic) lipids. Neutrality of the particle comes with some disadvantages such as low circulation time due to destruction by the reticuloendothelial system. [47] Further, net neutral charge of the particle may lead to aggregation due to a lack of electrostatic repulsion between particles in solution. [49] Incorporation of positively charged lipids into liposomes has shown to be advantageous for the encapsulation of negatively charged drugs, such as oligonucleotides, via electrostatic interaction. Despite this, cationic liposomes have shown to be toxic, induce an immune response, and show little to no improvement with respect to circulation lifetime. [47,50] The development of anionic liposomes has shown better endocytotic uptake, and overall stability compared to cationic and neutral liposomes. [51] These systems, however, can be considered more appropriate for the delivery of positively charged drugs or peptides rather than negatively charged cargo such as oligonucleotides. [51] Alternatively, pH sensitive liposomes may be used. These systems utilize amphiphilic lipids that maintain a positive charge at acidic pH but will become neutral at physiological pH. These systems will be discussed in further detail as they pertain to the presented work.

1.2.3.Potential barriers in liposomal development

Although liposomes have shown to be effective in drug delivery, they are not without their respective challenges. It has been shown that liposomes tend to accumulate in the reticuloendothelial system (RES) which includes the liver, spleen, kidneys, and bone marrow. Here, liposomes are susceptible to clearance by macrophages as well as non-specific interactions with blood plasma proteins. [46,52] This nonspecific binding (opsonization) is said to enhance the liposomes' ability to be cleared by the RES.

Particle toxicity may also restrict movement in the clinical pipeline. As briefly discussed, this may be offset through modification of the particle components. Finally, drug leakage may occur which may further a treatment's ability to act as originally intended.

1.2.4.Liposome modifications

While conventional, unmodified liposomes (Figure 1.5A) have shown success, they may be modified to increase circulation time, prevent non-specific interactions, or enhance delivery by means of ligand interactions.

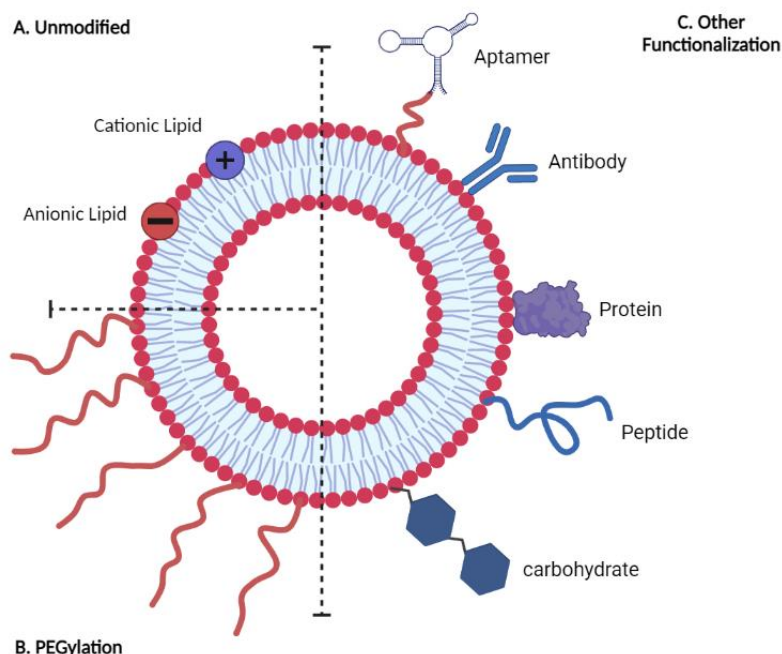


Figure 1.5. Illustration depicting the various modifications applicable to liposomal systems. Comparison of conventional liposomes, (A) containing only their respective cationic and anionic lipid components with other systems that are PEGylated, (B) or functionalized with other various agents (C) such as aptamers, antibodies, proteins, peptides, carbohydrates or other small

molecules. This figure has been modified from Sercombe et al. [46] and reprinted under the [creative commons attribution 4.0 licence](#). Image was constructed using BioRENDER™.

The conjugation of PEG groups to lipid components is one of the most commonly used liposome modifications (Figure 5B). Such steric stabilization allows for reduced immunogenicity from interaction with non-specific targets while simultaneously preventing rapid clearance by the RES. [46,53] This modification is advantageous in terms of stabilization but may interfere with the particles ability to interact with the desired target, and may cause undesired toxicity (i.e. immunogenic reactions) in some patients. [46]

Cholesterol can be argued to be one of the most important liposomal components due to its various functions. First, cholesterol contributes to the overall structural integrity of the liposomal membrane by providing elasticity and stiffness. [54] A finding by Semple et al suggested that because of cholesterol's ability to stabilize the membrane and provide fluidity, it can reduce various membrane imperfections, resulting in less opportunity for non-specific protein binding. [52] Based on the space cholesterol occupies in the lipid bilayer and the interactions it can form with other membrane lipids, it can aid to increase the overall packing of the membrane and help to prevent drug leakage. [54]

While passive targeting of liposomes is sufficient for delivery to many malignant tumor sites, [55,56] active targeting resulting from ligand conjugation can further enhance the existing passive targeting. [57] Ligands such as antibodies, small molecules, or peptides may be functionalized to the particle to act as targeting agents to specific cellular receptors (Figure 5C). [46,57] In combination with a functionalized imaging agent — such as a fluorophore — this approach can allow the particle to act as a theranostic. The internalized cargo acts as the therapeutic and the functionalized imaging agent can allow for the detection of cellular biomarkers. [46,58] The ability for liposomes to be modified in a manner such that their functional properties can be improved speaks to their overall versatility as a drug delivery method.

1.2.5.Mechanism of action

The targeting of liposomes to in vivo sites of interest can either be passive or active. The difference between the two lies in whether the liposome is linked with a targeting agent. Using cancer as an example, liposomes may exploit a phenomenon known as the enhanced permeability and retention (EPR) effect for tumor targeting. [55,56] The vasculature of typical tumor sites contains imperfections and irregularities in the endothelial lining of tumor capillaries leading to gaps where liposomes and other large carriers may enter the interstitial space of the tumor tissue. [55,56] This parameter may vary between different cancer types but allows for accumulation of liposomes and other high molecular weight molecules at the tumor site. [55] Due to their tendency to diffuse back into blood circulation, lower molecular weight species do not typically accumulate in the tumor space via EPR. [55]

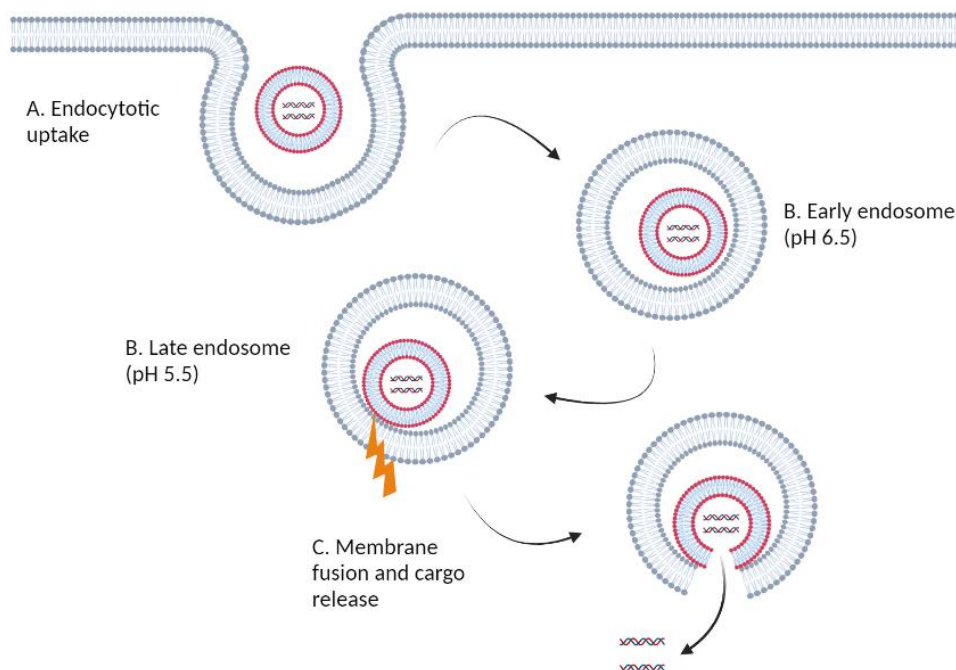


Figure 1.6. Illustration outlining the process of liposomal endosomal escape. After endocytotic uptake (A), the maturation and associated acidification of the endosome leads to the release of internalized cargo. Figure adapted from Degors et al. [59] under the [creative commons attribution license](#).

Contrary to passive targeting, active targeting relies on the functionalization of a targeting ligand to the surface of the liposome. These ligands include small molecules,

aptamers, antibodies, or small peptides (Section 1.2.4.). [55] This approach is used to target overexpressed biomarkers such as cell surface receptors, membrane proteins and can even facilitate organelle-specific targeting. [55] The specific targeting achieved from functionalization can allow for the reduction of off-target effects as well as selectivity towards “undruggable” targets such as intermembrane or intracellular proteins. [60]

When in the tumor interstitial space, the liposome must enter the cell before the internalized cargo may be released. In the case of non-functionalized liposomes, electrostatic interaction with the cellular surface can initiate the process of endocytosis. [61] For functionalized liposomes, this process may be initiated through ligand binding with cellular biomarkers, such as membrane receptors. [59,61] In this context, the broad term of endocytosis can be used to encompass the various types including clathrin-mediated endocytosis, caveolae-mediated endocytosis, or micropinocytosis. [61]

Upon entry into the cell, the liposome-containing endosome will gradually mature. The endosomal maturation is accompanied by the acidification of its interior. As the late endosome stage is reached, the pH is lowered to approximately 5.5 to facilitate the fusion of both the liposomal and endosomal membrane [59,62] This final step in cargo release is said to follow the transient pore model which is preceded by a fusion pore. The transient pore model states that electrostatic interaction between the two membranes allows for lipid mixing, leading to the formation of pores, allowing for the release of internalized cargo into the cytosol. [59]

1.3. pH-sensitive liposomal systems

Perhaps one of the more significant advancements in liposome technology has been the development of pH-sensitive liposomes. Based on the mechanism of endosomal escape, these systems have been tailored to increase intracellular delivery of desired drug cargo. [63] pH sensitive liposomes arose from the concept wherein certain viruses could exploit the natural pH changes observed in the cell to facilitate infection, as well as the notion that tumor microenvironments are relatively acidic. [63,64,65] pH-sensitive liposomes are stable at physiological pH (7.4) but will become destabilized under acidic

conditions as the endosome progresses from its early to late stage, allowing for the release of the internalized cargo. [63]

1.3.1. Dioleoylphosphatidylethanolamine (DOPE)

It has been shown that one of the most critical components of pH sensitive liposomes is the phospholipid phosphatidylethanolamine, or more specifically, its derivative DOPE. This zwitterionic lipid possesses a small head group which occupies a smaller volume in solution than its hydrocarbon tail, giving it an inverted cone shape. [63] In contrast, other lipids such as phosphatidylcholine (and derivatives) or lysophosphatidylcholine have larger head groups which occupy more volume, giving them either a normal cone, or cylindrical shape. [63]

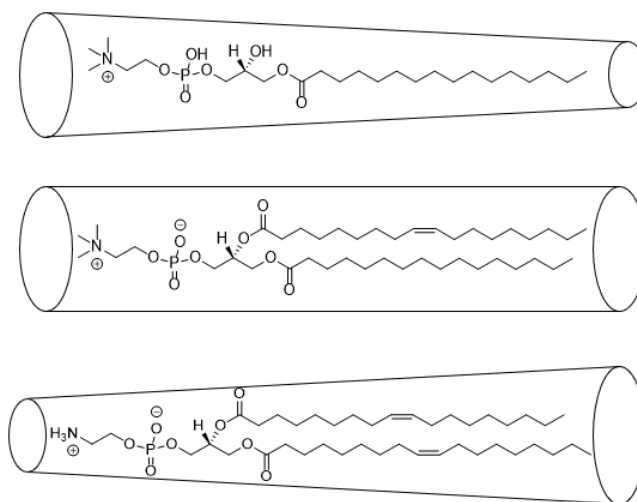


Figure 1.7. Structures of lysophosphatidylcholine occupying a conical shape (top), palmitoyl-2-oleoyl-sn-glycero-3-phosphocholine (POPC) occupying a cylindrical shape (middle) and DOPE occupying an inverted conical shape (bottom). Figure adapted with permission from Karanth et al. [63] with an appropriate copyright licence (Oxford University Press).

The unique inverted cone shape of PE and its derivatives gives it a tendency to form an inverted hexagonal phase (H_{II}) above its phase transition temperature (10°C for DOPE) under slightly acidic conditions. [63] When DOPE is formulated into liposomes with cholesteryl hemisuccinate (CHEMS), the negative charge of CHEMS at pH 7.4 has shown to stabilize DOPE through electrostatic repulsion between CHEMS molecules, allowing for a proper lipid bilayer to form. [63] Upon acidification, CHEMS will become protonated and neutral which will therefore lead to a decrease in electrostatic repulsion.

Consequently, DOPE will then transition to its H_{II} phase, leading to the destabilization of the liposomal membrane and associated cargo release. A study conducted in 2001 by Simoes et al. showed that the endosomal escape mechanism of these DOPE/CHEMS liposomes is more complicated than simply a decrease in pH. [66] It was later shown that endosomal proteins are critical in the process and will aid DOPE in the aggregation of the liposomes to release the internalized cargo. [67]

1.3.2.Cationic amphiphiles

Through the development of pH-sensitive liposomal systems, the introduction of pH-sensitive cationic lipids can improve cargo release existing DOPE/CHEMS system. A cationic component, rationally designed to have a pK_a between 6 and 7, will be protonated in the acidic conditions of the late endosome and tumor sites in general. [68] From this, the pH at which the liposomes destabilize can be tuned, and non-specific disruption of cellular plasma membranes can be reduced. [68,69] It has been proposed that when protonated, the cationic lipid forms electrostatic interactions with anionic lipids found in the endosomal membrane which is in accordance with the transient pore endosomal escape model. [59] This interaction forms a cone shape comprised of the two lipids, similar to that of DOPE. [68] The formation of the “pseudo” H_{II} phase by liposomal cations and endosomal anions leads to the formation of pores between the two membranes, allowing for the cargo to be released into the cytosol. [59]

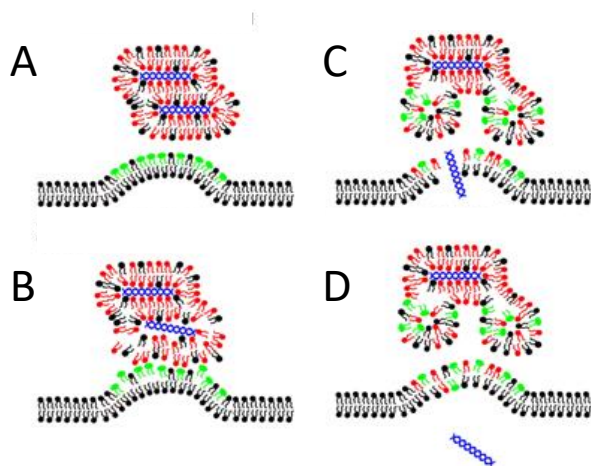


Figure 1.8. Illustration of the endosomal escape process according to the transient pore model. (A) lipid-based vehicle and endosomal membrane in close proximity, which leads to (B)

electrostatic interaction and rearrangement of lipids between the two respective membranes and the delivery vehicle begins its dissociation. This leads to the formation of a pore in the endosomal membrane (C), allowing the nucleic acid cargo to escape into the cytosol (D). Figure reprinted and adapted from Degors et al. [59] under the [creative commons attribution license](#).

Another advantage to the inclusion of a cation in pH-sensitive liposomes related to the encapsulation of nucleic acids. These systems may be formulated at acidic pH. Because of this, nucleic acids and other negatively charged molecules will form electrostatic interactions with the positively charged lipids to increase the overall encapsulation before the pH is raised in a second step. Collectively, the contributions of both DOPE and cationic amphiphiles to pH-sensitive liposomes creates a stable system, capable of selectively delivering cargo in large quantities to respective cellular targets.

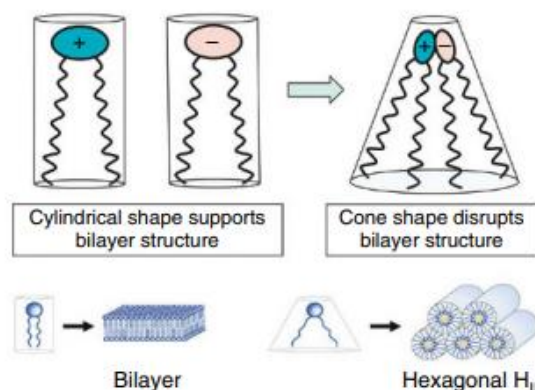


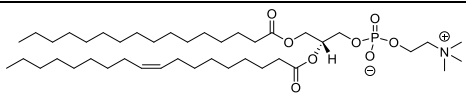
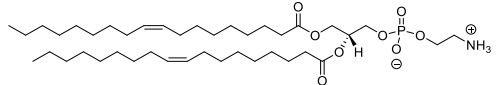
Figure 1.9. Illustration of lipid shape as it pertains to higher order membrane structure. The natural cylindrical nature of some lipids results in the formation of a bilayer. The electrostatic interaction with their oppositely charged counterparts supports the formation of an inverted hexagonal phase, which can lead to pore formation during the endosomal escape process, allowing for cargo release. Figure adapted with permission from Semple et al [68] and an appropriate copyright licence.

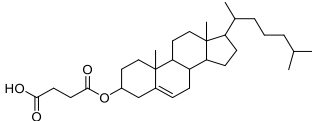
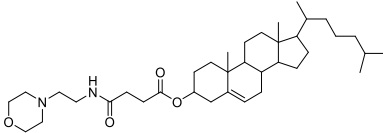
Cationic amphiphiles have become prevalent in pH-sensitive liposomal systems for RNA delivery. As mentioned previously, the integration of cationic amphiphilic lipids has already been observed in the clinically approved liposomal drug carrier, Onpattro. [70] It is described that the ionizable lipid DLin-MC3-DMA contains an ionizable nitrogen with a suitable pK_a value around 6.5. [70] This allows for the electrostatic interaction with lipids containing a negative charge, such that the resulting complexed lipids can facilitate the formation of an H_{II} phase to release the internalized contents from the liposome. [70]

1.3.3.NOV340

The NOV340 liposomal particles are a formulation of POPC, DOPE, CHEMS and MoChol in a molar ratio of 6:24:23:47 respectively. These particles are currently used to encapsulate CEBPA-51 saRNA's to give the product MTL-CEBPA. [65] The individually selected components used in MTL-CEBPA and NOV340 in general, have proven to generate, robust and effective liposomal particles for oligonucleotide delivery. As previously discussed, the behaviours of DOPE and CHEMS when formulated in liposomes allows for a system that can readily destabilize when met by the acidic conditions of the endosome. [71] The carboxylic acid group of CHEMS will maintain a negative charge at physiological pH, allowing DOPE to be stabilized in the membrane. When the pH drops to 5.2 in the late endosome, the negative charge of CHEMS is lost, and with it, the interaction with DOPE. [71] DOPE may then enter its H_{II} phase, allowing for the formation of pores in the liposomal and endosomal membranes, resulting in the release of the internalized cargo. Further, MoChol is designed such that the tertiary nitrogen of the morpholine ring will have a pK_a of around 6.5. As such, this molecule will be protonated at acidic pH and neutral at physiological pH. [71] Cationic charge at acidic pH is advantageous for two reasons; first, as previously stated, the encapsulation of negatively charged cargo — such as oligonucleotides— can be increased through the generation of electrostatic interactions. Second, electrostatic interactions between MoChol and negative charges on other lipids (such as POPC) or DOPE can aid in pore formation. [68,71]

Table 1.1. Composition of the MTL-CEBPA liposomal and saRNA formulation. [71]

Name	Structure	Concentration
CEBPA-51	5'-Abasic cap-GCGGUCAUUGUCACUGGUCUU-3' 3'-UUCGCCAGUAACAGUGACCAG	2.5 mg/mL
POPC		4.65 mg/mL
DOPE		18.0 mg/mL

CHEMS		11.3 mg/mL
MoChol		27.0 mg/mL

The main contributor to the overall surface charge of the NOV340 liposomes are the two ionizable lipids in the formulation. At physiological pH, the predominant charge of the particles is anionic due to CHEMS. This anionic charge provides the particles with an overall negative zeta potential (ζ), which is a representation of the actual surface charge. [49,71] As previously discussed, positively charged particles are generally toxic and generate an immune response in comparison to negatively charged particles. Charge is also a measure of the overall colloidal stability of the particles in solution. More specifically, as the surface charge (or ζ representation) approaches neutrality, the lower the colloidal stability will be. This means that the particles will have a tendency to aggregate. Consequently, it is desired that the overall charge be negative, and further away from zero (neutral) such that particle stability can be maintained. [49]

1.4. The fluororous effect

The fluorine atom has a high electronegativity, low polarizability, and relatively small size. [72] These characteristics may be exploited to further optimize small molecule therapeutic drugs by increasing their potency, membrane permeability and metabolic stability. [73,74] Further, the addition of this fluorine may influence structure, conformation, and pK_a . [73] Fluorine in small molecule drugs can offer an increased potency through engaging in protein interactions. An example of this is the small molecule fluorstrol, a dihydropyrimidine inhibitor. [73,75] This molecule has two fluorine atoms that form interactions with arginine and glycine residues of the human Eg5 binding pocket. [73,75] Comparison of fluorinated analogues versus non-fluorinated showed an overall increased potency. Fluorine may also contribute to the permeability of a given drug. This is owed to fluorine's ability to decrease the LogP (partition

coefficient) of the molecule, thereby increasing the lipophilicity and increasing its cellular permeability. [73] Labile hydrogens (either aryl or aliphatic) on a given molecule may be replaced with fluorine. The inherent strength of the carbon-fluorine bond can increase metabolic stability. Further, this moiety may be added to electron rich phenyl rings or heterocycles to serve the same purpose. [73] As previously mentioned, the addition of fluorine the 2' position of a nucleotide can contribute to its overall stability as well.

One of the less commonly discussed characteristics of fluorine is its behaviour when found in perfluorinated compounds. Fluorine is known to preferentially form interactions with itself over other atoms in PFCs. [72] When introduced to aqueous and hydrocarbon solutions, the PFC solution will form a distinct phase with a higher density than that of the aqueous and hydrocarbon solutions, resulting in a triphasic system. [72] This phenomenon of preferential interaction of fluorine in PFCs is denoted as the fluorous effect. While a relatively new concept in the context of therapeutic development, the fluorous effect has been applied to various systems including mass spectrometry, microarrays, and F^{19} MRI. [72] More notably, this effect has been seen in the development of lipoplexes containing fluorinated lipids for gene delivery. Systems containing fluorinated lipids showed a higher transfection efficiency compared to the non-fluorinated controls. [76,77] Studies such as these have shown the potential for fluorine into delivery systems and provides appropriate motivation for further investigation to its role in liposomal systems.

2. Development and characterization of pH-sensitive liposomes for encapsulation of oligonucleotide cargo

2.1. Design and characterization of cationic lipids

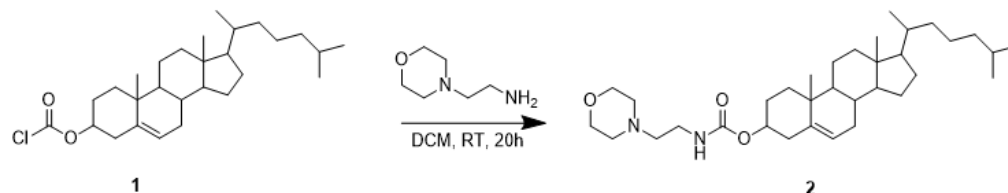
2.1.1. Rationale and objectives

The use of the MoChol cationic amphiphile in the NOV340 particles has shown to be a practical and effective choice. As such, we aimed to synthesize derivatives possessing similar properties to that of MoChol. These candidates were designed to maintain the general lipid amphiphilic architecture while also containing a quaternary protonated nitrogen in the polar head region ($pK_a = \sim 6.5$). Such a characteristic would allow for a predominantly protonated state under the acidic conditions of liposomal formulation and endosomal escape. [59,71] At physiological pH, the charge state is predominantly neutral. The given characteristics of these lipids should ideally contribute to the downstream liposome properties.

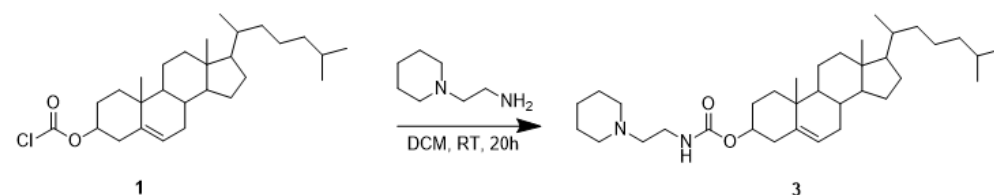
2.1.2. Synthesis and characterization of lipid candidates

Collectively, five different cholesteryl carbamate lipids were synthesized, alongside MoChol (**8**). The first of the set was a 2-aminoethyl morpholine derivative MCLM (**2**), similar to MoChol (**8**), but utilizing a carbamate linkage rather than a succinyl linkage (Scheme 1). The second derivative used was a 2-aminoethyl piperidine, MCLP (**3**) as a control containing a slightly less polar and much more basic head group. (Scheme 2)

Scheme 1. Synthesis of MCLM (**2**) (Figure S1, S2, S15).

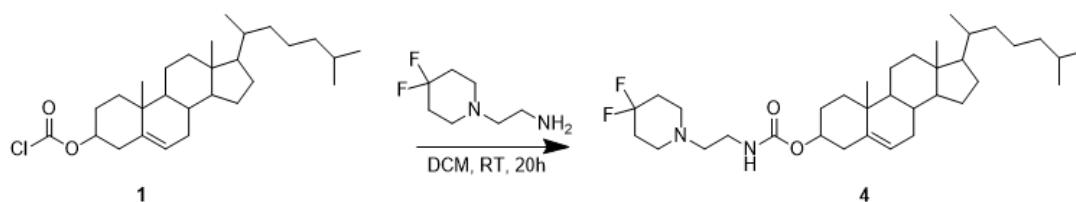


Scheme 2. Synthesis of MCLP (**3**) (Figure S3, S4, S16)

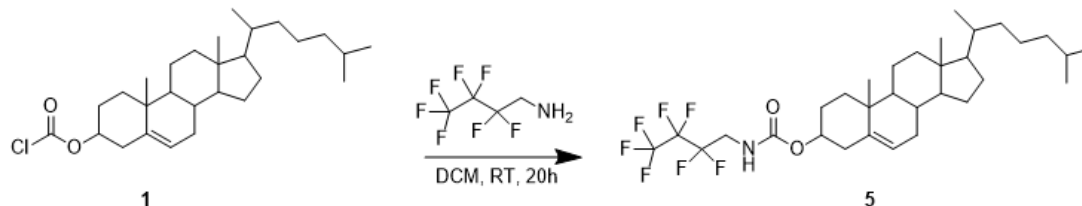


In an effort to assess the fluororous effect, two fluororous lipids were generated (Scheme 3 and 4), the first using 4,4-difluoroaminoethylpiperidine, MCLF (**4**) and the second using 2,2,3,3,4,4,4-heptafluorobutylamine, MCLH (**5**) to serve as a more heavily fluorinated comparison for downstream particle characterization. An additional, non-fluorinated control using butylamine was made, MCLB (**6**). Of note, MCLH and MCLB are not ionizable, but were developed to serve as heavily fluorinated, and non-fluorinated controls to analyze the relative contributions of cationic and fluororous effects in terms of particle uptake and endosomal escape.

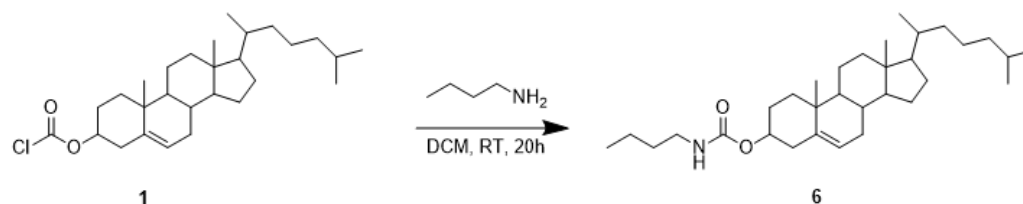
Scheme 3. Synthesis of MCLF (**4**) (Figure S5, S6, S7, S17).



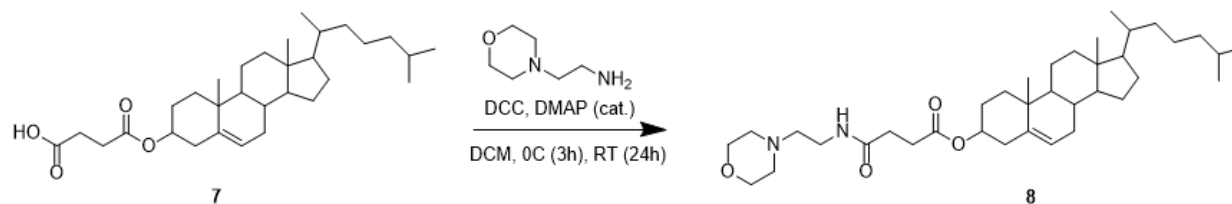
Scheme 4. Synthesis of MCLH (**5**) (Figure S8, S9, S10, S18).



Scheme 5. Synthesis of MCLB (**6**) (Figure S11, S12, S19).



Scheme 6. Synthesis of MoChol (**8**) (Figure S13, S14, S20).



An important characteristic for these lipids is their solubility properties. While each is readily soluble in halogenated solvents such as methylene chloride or chloroform, it is crucial for a lipid candidate to be fully soluble in ethanol. The chosen method of liposomal formulation involves microfluidic mixing of an aqueous solution and ethanol solution wherein the lipid components are dissolved in ethanol. Immediately, the candidates MCLM **(2)**, MCLP **(3)**, MCLF **(4)**, MCLH **(5)** and MoChol **(8)** showed favourable solubility in ethanol after brief sonication and/or heating. Conversely, MCLB **(6)** did not show any solubility in ethanol even with prolonged sonication and heating. At this stage, the differing solubility properties between MCLH **(5)** and its non-fluorinated counterpart, MCLB **(6)**, were of interest. The property of solubility is predominantly due to polarity and the ability for a compound to form interactions with its surrounding solvent. It can be proposed that the heavy fluorination seen with MCLH **(5)** could be accredited to the formation of non-classical F-H bonds in ethanol. [78,79] By contrast, MCLB is simply contains a short, non-polar chain in the region which should be representative of a “polar” head when referring to the general structure of a lipid. From this, it could be said head group polarity of the lipid is important for its solubility. Due to this negative result from MCLB **(6)**, it was excluded from further studies.

2.2. Liposomal formulation and Characterization

2.2.1.Rationale and objectives

We sought to introduce the newly synthesized lipid components into liposomal systems. In doing so, several comparisons could be made with respect to (1) Differences in particle characteristics such as diameter, zeta potential, polydispersity, and RNA encapsulation efficiency when using a carbamate versus a succinyl linkage in the cationic amphiphile, (2) The impact of fluorinated lipids on particle characteristics, and (3) Changes in particle characteristics when formulating fluorinated versus unmodified RNA into liposomes containing fluorous lipids.

The aforementioned NOV340 system has shown to be robust and effective as it relates to oligonucleotide delivery. This, coupled with the design of our amphiphiles, was indicative that this system was appropriate to use for further formulation and

characterization. Accordingly, the formulation procedures, lipid components, and lipid ratios were maintained with some modifications from previous literature. [71] Each of the presented liposomal formulations uses the formula of POPC, DOPE, CHEMS and the ionizable lipid in a 6:24:23:47 ratio respectively.

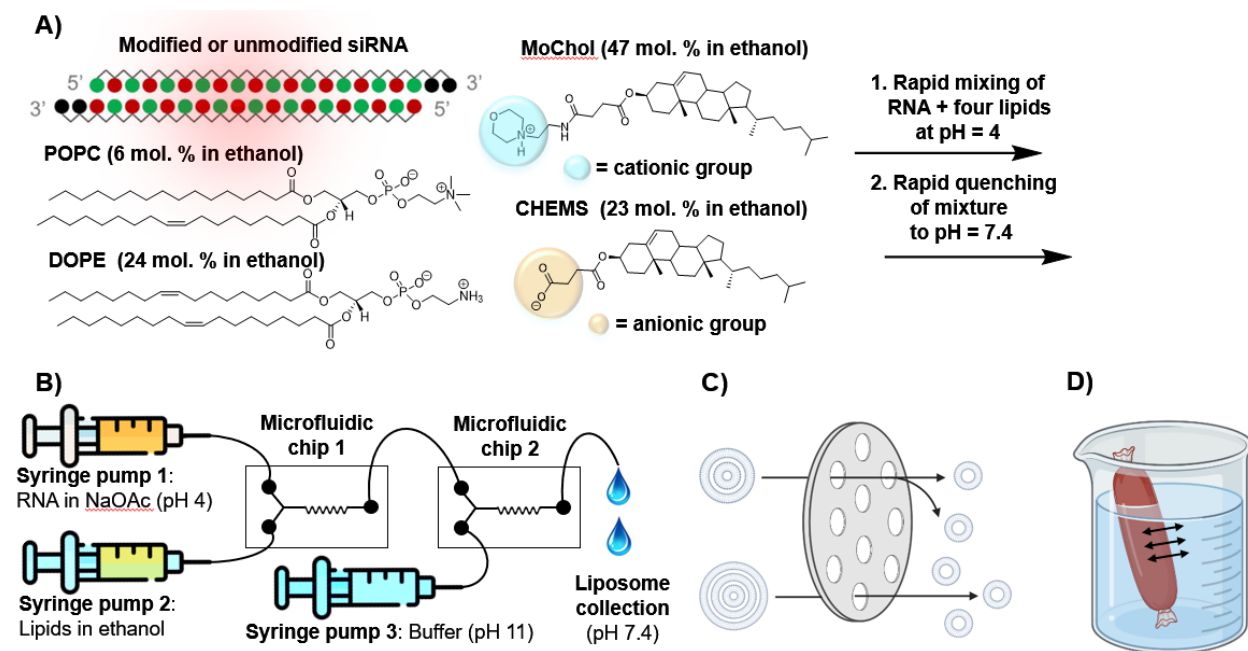


Figure 2.1. Illustration depicting the utilized liposome formulation process. (A) siRNA of sequence in combination with lipids in ethanol using the 6:24:47:23 ratio. (B) Microfluidic mixing of RNA in aqueous solution and lipids in ethanol followed by subsequent rapid pH adjustment. (B) Extrusion of liposomal solution through 0.2 µm polycarbonate filters. (D) Dialysis of liposomal solution to facilitate buffer exchange. Components of this figure were printed from BioRENDER™.

Our adapted formulation process occurs in three main steps. The desired RNA and lipid components are dissolved in aqueous NaOAc and absolute ethanol respectively.

(Figure 2.1A) Each solution is loaded onto a syringe pump where it is forced through a microfluidic chip containing an internal herringbone structure to facilitate rapid, turbulent mixing (Figure 2.1B). This solution is met in a secondary mixing chip by a buffer used to increase the pH to physiological conditions and to dilute existing ethanol (Figure 2.1B). The resulting liposomal solution is then extruded through 0.2 µm polycarbonate filters to reduce the lamellarity of the particles and to decrease polydispersity (Figure 2.1C). Finally, this solution is subjected to dialysis against a solution of 20% sucrose in 1X PBS as its final storage and usage medium (Figure 2.1D)

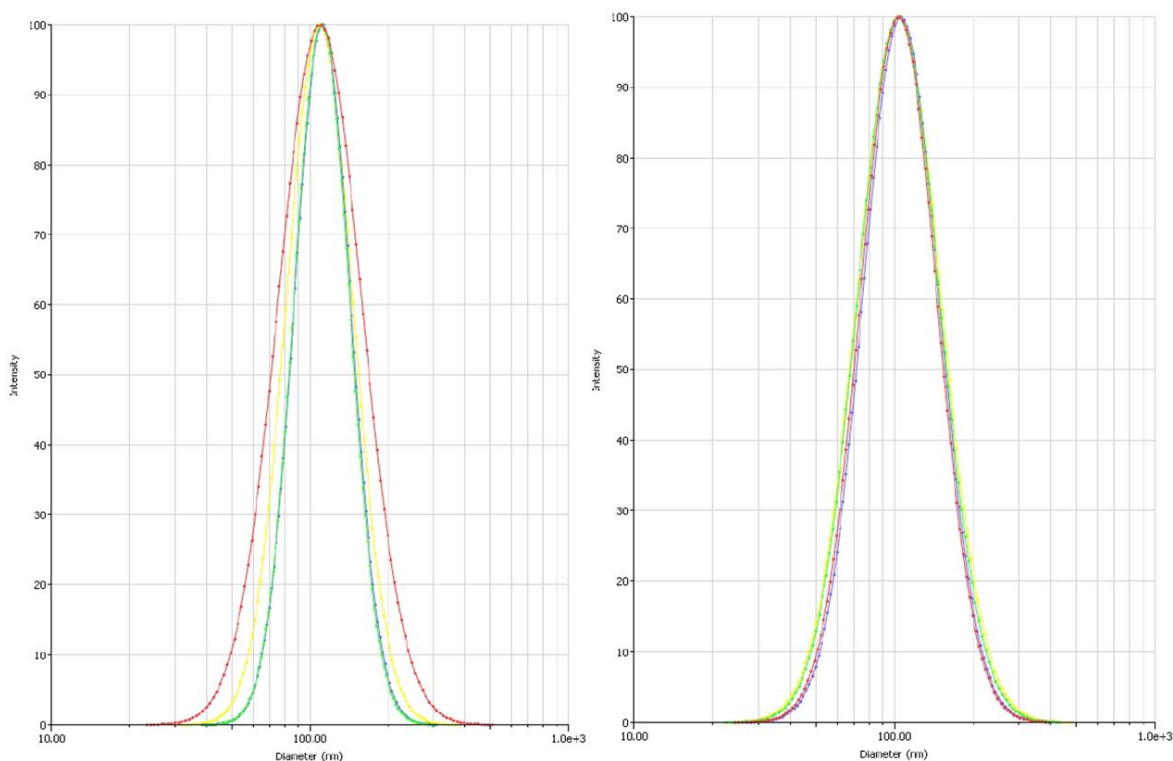


Figure 2.2. Lognormal distribution of particle diameter measurements for liposomes containing the MCLM (**2**, left) or the MoChol (**8**, right) lipids (Figure S21, S22). Data are plotted as effective diameter (nm) vs scattering intensity. Measurements were obtained using the NanoBrook OMNI (Brookhaven Instruments) and data were transformed using the CONTIN algorithm for size distribution.

These particles were then analyzed using DLS and PALS to determine particle properties such as their effective diameter, polydispersity index and zeta potential. Observed scattering intensities may be fitted to lognormal distributions from which, the effective diameter of the particle may be taken. Data obtained using PALS may be used to determine zeta potential of each of the given particle types as a representation of the liposome surface charge. In addition, the encapsulated siRNA cargo may be quantified using fluorescent probes of a RiboGreen (Invitrogen) assay for further in vitro applications (Section 3.2).

2.2.2. Comparison of carbamate and succinyl linkages in cationic amphiphiles

The previously generated lipids all contain a carbamate linkage that differs slightly from the succinyl linkage of MoChol (**8**). Therefore, our first interest was to investigate the

effect of the linkage type on liposome properties. Should the observed differences in particle characteristics be negligible, the cholesteryl carbamate derivatives could serve as a favorable alternative to their succinyl linkage counterparts due to their ease of synthesis. For this purpose, a previously validated siRNA sequence targeting fluorescent proteins such as mVenus and eGFP was used for all generated sequences. [80] For our studies, we used both an unmodified, and a fully (2') fluorinated siRNA sequence denoted as mVG and mVG-F respectively (Figure S25-S32). Sense (passenger) strand: 5'-GCACGACUUCUUCAAGUCCGCCA[dT][dT]-3' and Antisense (guide) strand: 5'-phos-UGGCGGACUUGAAGAAGUCGUGC[dT][dT] - 3'. Use of this sequence enabled in vitro assessment of developed particles (Section 3.2).

Table 2.1. Comparison of particle characteristics between MCLM and MoChol-based liposomes using mVG siRNA.

<i>Cationic Amphiphile</i>	<i>Effective diameter (nm)</i>	<i>Polydispersity index (PDI)</i>	<i>Zeta potential (mV)</i>	<i>siRNA encapsulation efficiency</i>
<i>MCLM (2)</i>	110	0.092	-30	80%
<i>MoChol (8)</i>	104	0.131	-31	76%

The main liposome properties of interest included particle diameter, polydispersity index, zeta potential and RNA encapsulation efficiency. The particles prepared using MCLM **(2)** and MoChol **(8)** exhibited nearly identical characteristics (Table 2.1). The effective diameter under 200 nm of these particles renders them ideal for long-circulating applications such as brain or tumour delivery, which is ideal for the downstream application to be further discussed (Figure S21, S22). [81] For the purposes of liposomes in drug delivery applications, polydispersity values should ideally be below 0.3. [81] Here, we observe values close to 0.1 which is indicative of a highly monodisperse liposomal population. Both samples show high encapsulation efficiencies of mVG siRNA with values of 80 % and 76 % respectively (Table 2.1). Control particles encapsulating tRNA show encapsulation values for MoChol-based particles that are within 2% of MCLM particles (Table S37), showing that the consistent performance of these of these two lipids is independent of the exact cargo contained within. All encapsulation efficiencies were quantified using a RiboGreen intercalating dye whereby

unknown liposomal-RNA samples were compared to standard curves generated with the respective RNA type.

The particles prepared using MCLM **(2)** and MoChol **(8)** have a predominant negative charge at physiological pH, due to the pK_a of both the carboxylic acid group of CHEMS and the basic nitrogen of MCLM **(2)** and MoChol **(8)**. The estimated pK_a of said nitrogen on the morpholine ring of MoChol **(8)** is approximately 6.5. Because the approximate pK_a of MoChol **(8)** is known, differences in the zeta potential between MoChol-based particles and other particles can be used to estimate the nitrogen pK_a of our synthesized lipids with respect to MoChol **(8)**. [82] The similarity in zeta potential measurements between MoChol-based particles and MCLM-based particles (Table 2.1) suggests that the pK_a values of the ionizable nitrogen on both molecules are very similar to each other.

The characterization of both MoChol and MCLM-based liposomes revealed minimal differences for the particle size, polydispersity, zeta potential and encapsulation efficiency measurements. Pending further investigation into other properties such as particle stability, biocompatibility and toxicity, these preliminary results suggest that the carbamate and succinyl linkages could be interchangeable in the context of sterol-based lipids in liposomal systems. This would be advantageous in this application due to the ease of synthesis of carbamate derivatives when compared to succinyl linkage counterparts.

2.2.3. Further particle synthesis and characterization

The study was broadened to include liposomal formulations utilizing the MCLP **(3)**, MCLF **(4)** and MCLH **(5)** lipids that contain the same carbamate linkage as MCLM. Using the same formulation procedure as previously described (Figure 2.1), we aimed to assess each liposomal formulation to determine whether their properties would be suitable for further investigation. In addition to the listed properties, cryo-TEM was conducted to gain understanding of the physical particle morphology, general size distribution and lamellarity.

During attempted liposome formulation, visible aggregation was observed in liposomal samples containing the MCLP **(3)** lipid. This was confirmed by DLS particle sizing measurements (Table 2.2). Perhaps the most rational explanation for the observed aggregation relates to the polarity of the lipid head group. Unlike the morpholine head structure seen in MCLM **(2)** and MoChol **(8)**, the piperidine head of MCLP **(3)** is likely too non-polar, with the nitrogen being too basic to change its charge state in the working pH conditions. Due to this result from MCLP **(3)** formulations, further characterization such as zeta potential measurement and encapsulation efficiency were not conducted and MCLP was excluded from further formulations and evaluation.

Table 2.2. Comparison of liposome characteristics encapsulating mVG siRNA, using each of the synthesized lipids.

<i>Cationic Amphiphile</i>	<i>Effective diameter (nm)</i>	<i>Polydispersity index (PDI)</i>	<i>Zeta potential (mV)</i>	<i>siRNA encapsulation efficiency</i>
<i>MCLM (2)</i>	110	0.092	-30	80.0%
<i>MCLP (3)</i>	>1000	0.255	N/A	N/A
<i>MCLF (4)</i>	137	0.169	-24	55%
<i>MCLH (5)</i>	219	0.256	-44	47%
<i>MoChol (8)</i>	104	0.131	-31	76%

MCLF and MCLH-based particles showed a trend of increasing size and polydispersity is observed with increased lipid fluorination (Table 2.2). The measured diameter for MCLF particles (137 nm) was slightly higher than MoChol and MCLM-based particles but remains under the threshold for use with tumour systems (Table 2.2, Figure S23). [81] The observed polydispersity for these particles (0.169) falls within the acceptable range for particles of this type and is still representative of a relatively monodisperse particle population (Table 2.2). To the contrary, the observed particle size for MCLH-based particles (219 nm) fell just outside the acceptable range for tumor applications, and the polydispersity of 0.256 approaches the upper threshold for liposomes in drug delivery applications (Table 2.2, Figure S24). [81] The zeta potential value for MCLF-based particles of -24 mV revealed that the pK_a of the MCLF basic nitrogen likely sits slightly higher than 6.5. Should the pK_a be higher, more positive charge from MCLF would be present, therefore skewing the zeta potential in the positive direction. While

this zeta potential value lies slightly within the range of lower colloidal stability (-30 mV to +30 mV). [83] appropriate suspension in solution has been observed with these samples over time with no indication of aggregation. Zeta potential is not a direct measurement of particle net charge but rather a representation of particle charge based upon the surrounding environment and is therefore not the only variable to be considered when determining particle stability. [84] Should particles of this type continue to show promise then alteration of the lipid ratios could be considered such that the molar ratio of CHEMS is increased and MCLF is decreased to give the zeta potential a more negative value. The zeta potential for MCLH-based particles (-44 mV) acted as a proof of concept (Table 2.2). Due to MCLH's lack of a positive charge, the negative charge contribution from CHEMS at physiological pH will not be offset which results in an increasingly negative observed zeta potential value.

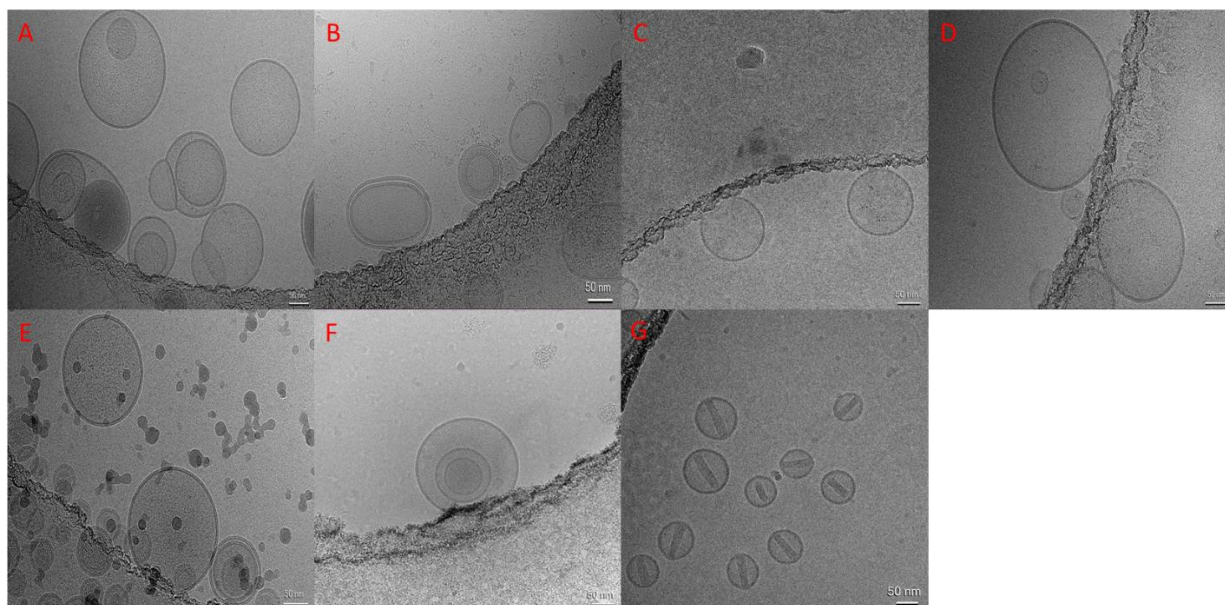


Figure 2.3. Cryo-TEM microscopy images of liposomal samples based on (A) MCLM **(2)**, (B) MoChol **(8)**, (C) MCLF **(4)**, and (D) MCLH **(5)**. (E) Commercial NOV340 liposomes. (F) Moderna mRNA liposomal formulation against SARS-CoV2. (G) Doxove liposomes encapsulating doxorubicin.

The use of Cryo-TEM allowed for the physical observation of the liposomal membrane to determine the lamellarity of each particle formulated using different cationic amphiphiles. Immediately, similarities between MCLM and MoChol-based particles can be seen. Interestingly, both particle samples showed a relatively heterogenous mixture

of various liposome morphologies including unilamellar vesicles, MVV's, and MLV's (Figure 2.3A,B). Theoretically, the formulated MoChol-based particles should show characteristics similar to the commercial NOV340 particles. Cryo-TEM images from MTL-CEBP α particles (Figure 2.3E) were also obtained. Heterogeneity in particle lamellarity in said images confirmed that this property was also appropriately observed for the in-house MoChol and MCLM particles. It has also been suggested that heterogeneity with respect to liposome lamellarity can be attributed partially to microfluidic formulation methods, which may provide some explanation in these cases. [84] With this method, the chance for fluctuations in homogenous mixing may be the culprit for changes in liposome lamellarity. [85] Further, this characteristic may also be attributed to the distribution and size of the herringbone structure within the PDMS microfluidic chips. Because particle characteristics are dependent on many factors, the difference in lipid components between samples here may contribute to the overall differences in lamellarity. The images obtained for MCLF-based liposomes (Figure 2.3C) surprisingly revealed the presence of unilamellar particles <200 nm in diameter in all cryo-TEM grids. This observation did not align with the reported heterogeneous lamellarity observed for MCLM and MoChol particles. Furthermore, this property was also seen for MCLH-based particles (Figure 2.3D), suggesting that perhaps the abundance of fluorine has some influence on liposome lamellarity.

During the formulation process, liposomal samples are subjected to manual extrusion through 0.2 μ m polycarbonate membranes to decrease both polydispersity and lamellarity. Obtained results suggest that MCLM and MoChol-based liposomes may require additional extrusion for the reduction of lamellarity when compared to fluorinated counterparts. Looking closer at MCLH-based particles (Figure 2.3D), particle diameters exceeding 200 nm could be explained by the phenomenon known as reversible elastic deformation. [86] Because the used extrusion membranes are 0.2 μ m in pore diameter, this should theoretically produce particles that are smaller pore size, as indicated by all other samples. The observed diameters larger than 200 nm could therefore suggest that this phenomenon is in effect whereby the formulated liposomes are able to deform in order to pass through the inherently smaller extrusion pores. The collective particle size, polydispersity, zeta potential, encapsulation efficiency, and cryo-TEM results coupled

with the poor reproducibility of MCLH-based particles lead to the lipids dismissal from further study. With this in mind, there are some potential explanations to worsening particle properties with increased fluorination state. We first observed with MCLF **(4)** particles that the effective particle diameter increased when compared to non-fluorinated counterparts (Table 2.2.). This characteristic was exacerbated with the increased fluorination state of MCLH **(5)** particles. The potential trend of increasing size with fluorination state could suggest that altering the lipid ratio such that the cationic amphiphile (MCLF **(4)** or MCLH **(5)**) is in lower abundance than the 47 % that was used in the established procedure. This may also help to offset the proposed reversible elastic deformation as it was a characteristic seen when MCLH **(5)** was used. Further, in microfluidic liposome formulation, it has been shown that increasing flow rate ratio of aqueous (RNA containing) to organic (lipid containing) media leads to decreased particle size. [87] In the case of MCLH **(5)** particles (and potentially other heavily fluorinated particles) increasing the flow rate ratio could help to achieve the desired particle size and perhaps make the procedure more reproducible for formulations containing MCLH **(5)**. Lastly, increasing the temperature at which the formulation is carried out can lead to the formation of smaller particles. Increased temperature allows the lipids to enter phase-transition more readily to form the liposome rather than remaining as “bilayer disks”. [88] Alternatively, liposome formulations using heavily fluorinated lipids have been conducted using the more traditional method of lipid film hydration. [89] For our purposes, MCLH **(5)** was designed as a heavily fluorinated control, however these procedural improvements could be implemented upon the design of a heavily fluorinated, and cationic lipid for this application.

In addition to the formulated liposomes and commercial NOV340 particles, we have obtained images of the SPIKEVAX vaccine against SARS-CoV2 (Moderna Therapeutics) and Doxoves liposomes encapsulating doxorubicin (Formumax Scientific). The images of SPIKEVAX (Figure 2.3F) show MLV character similar to liposomes containing the MCLM **(2)**, or MoChol **(8)**, lipids (Figure 2.3A,B). Additional images of this sample indicated the presence of unilamellar liposomes as well. Doxove particles (Figure 2.3G) show a very homogenous size distribution and consistent

unilamellar membrane character that aligns with the observations of MCLF-based liposomes (Figure 2.3C).

2.2.4.Evaluation of the fluorous effect through the use of fluorinated siRNA

It has been previously stated that one of the common modifications to siRNAs and other therapeutic oligonucleotides is the introduction of a fluorine at the 2' position of the nucleotide. To evaluate the fluorous effect on a practical level, we sought to formulate mVG-F siRNA into liposomes to observe potential changes in particle characteristics such as diameter, polydispersity, zeta potential and encapsulation efficiency. Based on the underlying principle of the fluorous effect, it may be expected that fluorinated RNA encapsulation could increase when formulated into fluorinated liposomes due to preferential fluorine interaction.

Table 2.3. Comparison of particle characteristics between MCLM, MoChol and MCLF-based liposomes encapsulating mVG or mVG-F siRNA.

<i>Cationic Amphiphile</i>	<i>Effective diameter (nm)</i>	<i>Polydispersity index (PDI)</i>	<i>Zeta potential (mV)</i>	<i>siRNA encapsulation efficiency</i>
MCLM (2)	104	0.104	-24	67%
MCLM (2)*	110	0.092	-30	80%
MoChol (8)	106	0.157	-20	75%
MoChol (8)*	104	0.131	-31	76%
MCLF (4)	152	0.173	-30	55%
MCLF (4)*	137	0.169	-24	55%

*Unmodified siRNA formulation

The effective diameters remained relatively constant with only some slight deviation between mVG to mVG-F siRNA formulations. MCLF-based particles showed the largest difference with a 16 nm increase in the particle diameter (Table 2.3). Polydispersity values when changing from mVG to mVG-F siRNA showed a small, and perhaps negligible increase. When switching from mVG to mVG-F siRNA, the zeta potential values for MCLM (2), and MoChol (8) samples showed a 6-11 mV increase while MCLF (4) sample zeta potential moved in the negative direction to -30 mV (Table 2.3).

Based on the principle of the fluorous effect, it could be expected that the RNA encapsulation efficiency could increase when using a fluorinated liposomal system coupled with fluorinated RNA. Here, however, we observe no significant change in encapsulation values between MCLF **(4)** particles when using mVG vs mVG-F siRNA. However, with the decrease in RNA encapsulation with MCLM **(2)**-based particles, it could be suggested that because MCLF **(4)** particles did not show the same decrease in encapsulation for fluorinated RNA, that we are observing some fluorous interaction which helps maintain RNA encapsulation. Perhaps it is more likely that the level of fluorination on the MCLF **(4)** lipid is not sufficient to generate a fluorous phase with fluorinated RNA within the particles aqueous core. Should the DLS and PALS results from MCLH **(5)** particles been more favourable in the context of delivery, it possibly could have shown some differences due to its increased fluorination state (7 compared to 2 fluorine's). The ideal alternative in this scenario would be a lipid that is designed to have an ionizable character as well as a heavier fluorination state. This could allow for the further investigation of the fluorous effect in liposomal systems without sacrificing the essential activity that the ionizable lipid offers with respect to RNA encapsulation and endosomal escape. In summary, we have succeeded in the synthesis and characterization of liposomal nanoparticles containing fluorinated lipids and fluorinated siRNA cargos. Next, these formulations were applied to living cells for the observation of cellular uptake and gene silencing (Section 3.1-3.2).

3. In vitro assessment of liposomal formulations

3.1. Liposome uptake studies

3.1.1. Rationale and objectives

To further examine the functional properties of our formulated liposomes, we first aimed to functionalize tRNA with a cell-impermeable fluorescent dye. This functionalized RNA was then formulated into liposomes which were then incubated with cells. The use of a cell-impermeable dye in this context was crucial to unambiguously demonstrate that uptake was associated with delivery by liposomes. Upon incubation, the fluorescent RNA provided insight into whether the particles were being internalized by cells and the overall distribution of the particles within the cell.

3.1.2. Synthesis of fluorescently labelled tRNA

Initial efforts to formulate a cell-impermeable dye (propidium iodide) into liposomes using only a solution of the dye combined with tRNA resulted in particle aggregation, likely due to the hydrophobicity and positive charge of the dye. In lieu of this approach, we opted to functionalize tRNA with a cell-impermeable dye to quantify cellular uptake.

The dye of choice for this process was ethidium bromide monoazide (EMA) which is cell-impermeable primarily due to positive charge and extended aromaticity. This molecule also possesses an accessible azide moiety for reaction with alkene groups of RNA bases. The use of a light catalyzed crosslink reaction to generate highly reactive nitrene intermediates allowed for multiple irreversible insertion products with tRNA (Scheme 8). [90] After irradiating a sample of tRNA in the presence of EMA with blue light for 2.5 hours, a notable red shift in the ethidium fluorescence maxima was observed. This shift from 590 nm for the non-irradiated sample to 600 nm served as the first potential indicator of reaction completion (Figure 3.1A). The azide group of EMA is electron withdrawing. Following nitrene formation, the resulting amine group would be electron-donating which would result in a red-shifted fluorescence. [90]

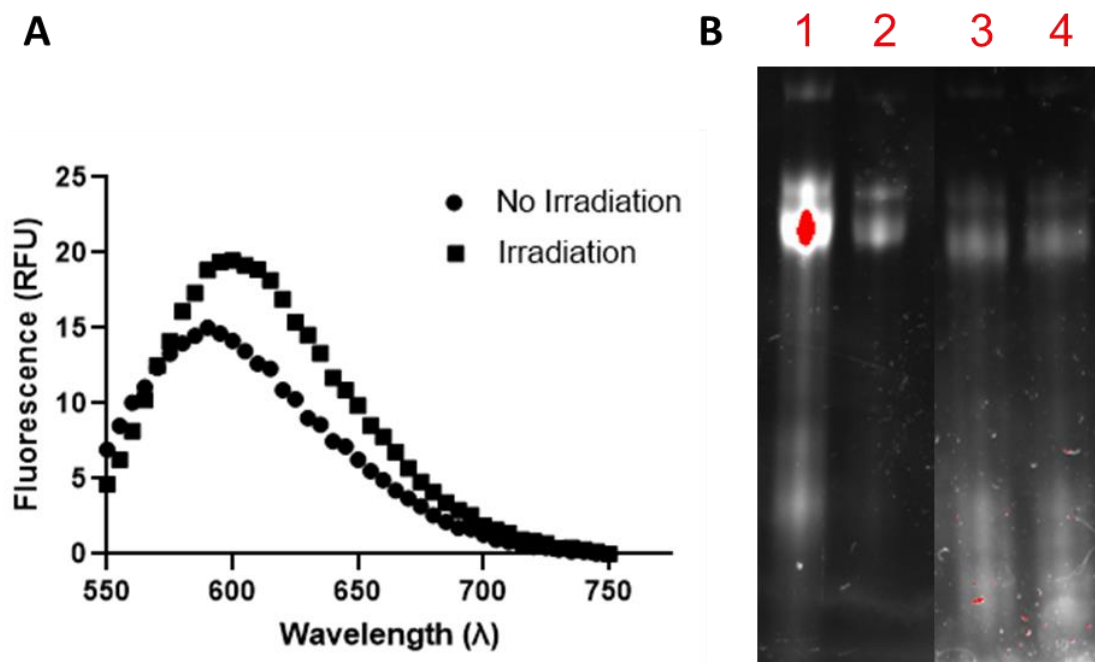


Figure 3.1. (A) Fluorescence spectra of irradiated and non-irradiated samples of the light catalyzed crosslink reaction (B) 15% polyacrylamide denaturing gel images showing ethidium bromide (lanes 1 and 2), and SYBR Gold (lanes 3 and 4) intensities. Lanes 1 and 3 show non-purified samples while lanes 2 and 4 show spin column treated, irradiated samples.

To further confirm the completion of the reaction, RNA samples were run on a denaturing polyacrylamide gel before and after being subjected to purification using a spin filtration column. It was expected that filtration would remove any excess of free ethidium bromide monoazide. As a result, gel images under these conditions should only show functionalized RNA. We can see that prior to filtration, SYBR gold staining (Figure 3.1B, lane 3) confirms the presence of RNA while ethidium bromide measurement indicates a high intensity of the fluorophore in the sample (Figure 3.1B, lane 1). Post-filtration, we observe a relatively constant concentration of RNA based on SYBR gold intensity (Figure 3.1B, lane 4). However, a reduced ethidium bromide monoazide signal was seen (Figure 3.1B, lane 2), and was indicative that the irradiation was able to facilitate the crosslinking reaction to a measurable extent. Collectively, the red shift in fluorescence observed after the reaction, coupled with the ethidium bromide monoazide gel signal were sufficient to suggest that the tRNA was indeed successfully modified and could be carried forward for liposome formulation.

3.1.3. Visualization of liposome uptake by confocal microscopy

One important functional property of liposomes is their ability to be taken up by cells and deliver their internalized cargo that can then exert its desired biological activity.

Therefore, investigation of the uptake properties of our liposomes was of high priority. Liposomes encapsulating the previously synthesized ethidium bromide monoazide tRNA were formulated and incubated with MDA-MB-231 breast cancer cells. This cell line was previously transformed by lentiviral transfection to stably express eGFP.

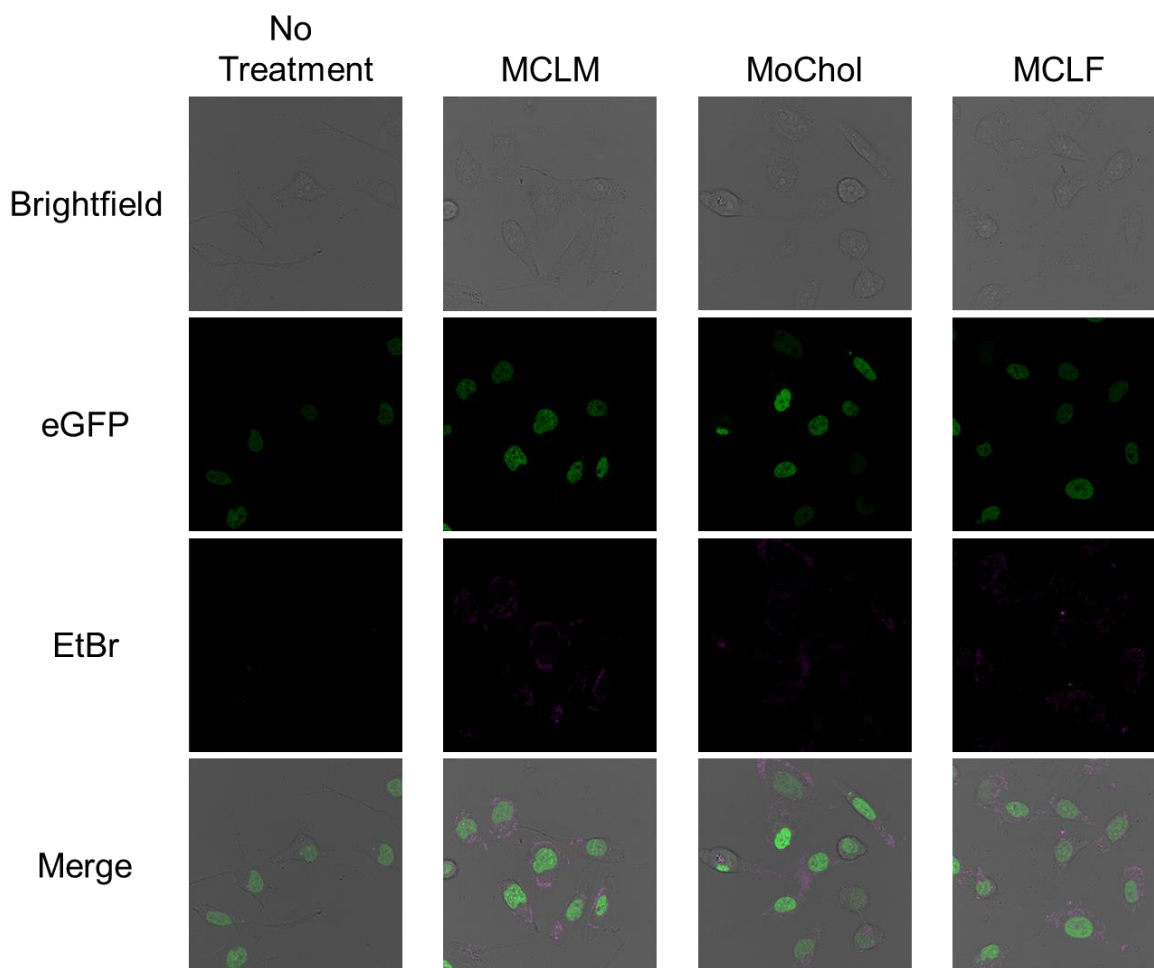


Figure 3.2. Confocal microscopy images showing the presence of eGFP (green) and distribution of EMA-tRNA formulated liposomes (magenta) in MDA-MB-231 cells. Images were obtained using a 488 nm laser for eGFP and 561 nm laser for ethidium bromide detection.

In comparison with untreated samples, cells treated with liposomal particles using MCLM, MoChol or MCLF all appeared to show cellular uptake (Figure 3.2). The ethidium bromide fluorescent signal (magenta) is dispersed predominantly throughout

the cytosol and is clearly distinguishable from the eGFP signal (green) arising from the nucleus of each cell. The localization of liposomal cargo and its punctuated pattern in the cytosol is in accordance with the known mechanism of liposome uptake whereby foreign bodies, such as liposomes, are taken up by cells and are carried through the endosomal maturation and escape process. [55]

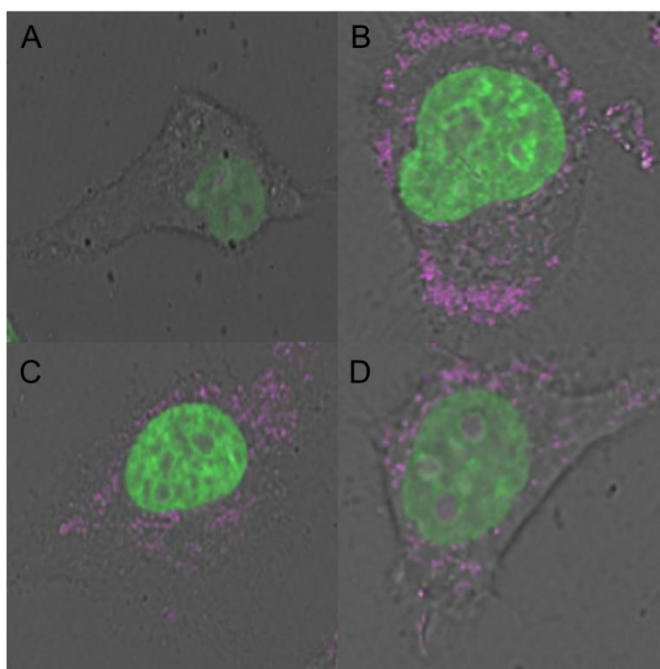


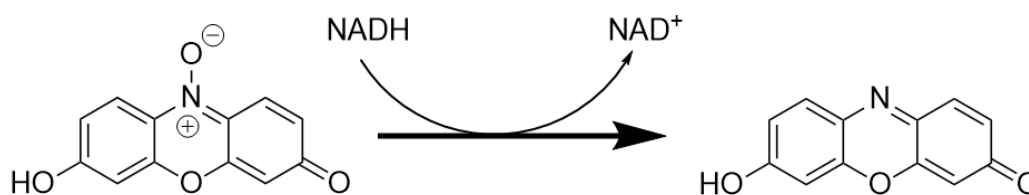
Figure 3.3. Zoomed confocal microscopy images of the merged channel showing (A) untreated, (B) MCLM-based liposome, (C) MoChol-based liposome, and (D) MCLF-based liposomes encapsulating EMA-tRNA. eGFP fluorescent signal is presented in green and modified fluorescent tRNA is presented in magenta. Images were obtained using a 488 nm laser for eGFP and 561 nm laser for ethidium bromide detection.

Looking in more detail at the merged images obtained from confocal microscopy (Figure 3.3), we can more clearly see the distribution of EMA-tRNA formulated liposomes in the cytosol of treated cells. In accordance with previous studies, the observable small clusters of EMA-tRNA signal suggest endosomal localization of the liposomes as they proceed with maturation. [91] Collectively, the observed signals and localization of the EMA-tRNA liposomes is indicative of effective liposome uptake over the course of 4 hours. Further, this result justified further investigation of these developed carriers for delivery of biologically active siRNAs.

3.2. Knockdown and toxicity assessment of liposome formulations

3.2.1. Rationale and objectives

To complement liposome uptake studies, we sought to utilize liposome formulated siRNAs targeting mVenus and eGFP fluorescent proteins to evaluate knockdown activity. For this purpose, MOLM-14 cells stably expressing mVenus and luciferase were used along with the previously described MDA-MB-231-eGFP cells. The MOLM-14 cell line was chosen as a model for acute myeloid leukemia (AML) for the purposes of an ongoing collaboration using siRNAs for AML treatment. Because the various liposome formulations are able to enter cells, information obtained from gene knockdown assessment could be used to make inferences on the liposomes' ability to release cargo by endosomal escape pathways.



Scheme 7. Conversion of resazurin to resorufin from reduction by NADH during cellular respiration in the mitochondria.

To assess particle toxicity from lipid components, liposomes encapsulating unmodified tRNA were formulated. To quantify toxicity, a resazurin assay was employed (Scheme 7) whereby resazurin is reduced by one of the various players in cellular respiration (NADH, NADPH, FADH₂, etc.) to resorufin. [92] The fluorescent character of the resorufin product may be quantified using standard fluorimetry and used as a measure of overall viability. [92,93]

3.2.2. siRNA knockdown and liposomal toxicity assessment

To assess the delivery efficiency of the developed liposomes, siRNA sequences were encapsulated targeting the mVenus and eGFP fluorescent proteins. Each formulation containing a different ionizable lipid were incubated with MOLM-14 and MDA-MB-231 cell lines. Previous literature has reported a concentration of 80 nM siRNA was

sufficient to observe knockdown activity of GFP. [94] Due to discrepancies in the used cell lines, we deemed it necessary apply a concentration gradient to determine which concentration would be optimal for our applications.

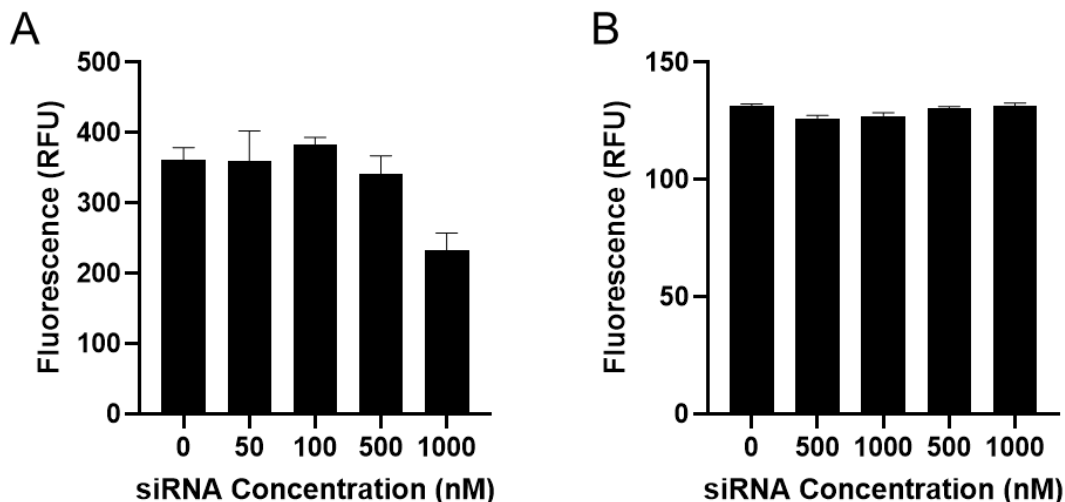


Figure 3.4. Gene knockdown efficiency of MCLF-based liposomes encapsulating mVG siRNA. Fluorescence (RFU) measurements for (A) mVenus expressing MOLM-14 cells and (B) eGFP expressing MDA-MB-231 cells taken 72 hours post-incubation with siRNA encapsulated liposomes. Fluorescence was measured at 530 nm for both cell lines and error bars represent S.E.M. Fluorescence for mVenus (MOLM-14) was measured at excitation: 480 nm, emission: 500-620 nm, cutoff: 515 nm, while eGFP (MDA-MB-231) was measured at excitation: 460 nm, emission: 500-600 nm, cutoff: 495 nm.

At first glance, these initial experiments gave us various insights into activity. First, incubation with MOLM-14 cells revealed a ~40% reduction in mVenus fluorescence while others did not differ greatly from the non-treated sample (Figure 3.4A). Results obtained from the resazurin assay of these samples revealed a visible reduction in cell viability for the 50 nM incubation, indicating some cellular toxicity at this concentration point (Figure 3.5A). Based on the decrease in mVenus fluorescence from 1000 nM siRNA and the lower viability seen with 50 nM siRNA, we looked to evaluate these concentrations further. It was later clear that the toxicity (Figure 3.5A) at 50 nM was likely due to external factors such as the utilized buffer or other contaminants in the specific sample as there were no further indications that the 50 nM siRNA concentration was toxic (Figure 3.6B). The same effect on eGFP fluorescence was not seen when the same siRNA concentrations were incubated with MDA-MB-231 cells (Figure 3.4B). Only

minimal differences in eGFP fluorescence were observed and overall viability aligned with control samples (Figure 3.5B). Additionally, results obtained from the resazurin assay of MDA-MB-231 cells showed comparable viabilities between liposomal incubations and the non-treated sample. Although we have previously reported uptake of liposomes using this cell line, it appears that eGFP expression in this cell line remains unaltered using the selected siRNA sequence. This could potentially be attributed to compatibility of the siRNA sequence with the cell line. With this said, we opted to proceed using the MOLM-14 cell line for further knockdown experiments.

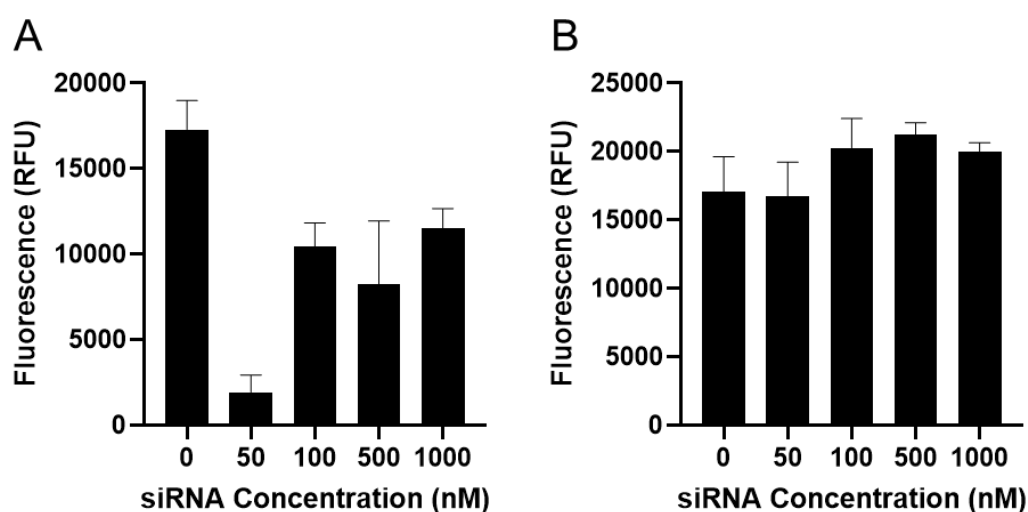


Figure 3.5. Toxicity of MCLF-based liposomes encapsulating mVG siRNA. Fluorescence (RFU) measurements for the resazurin assay of (A) mVenus expressing MOLM-14 cells and (B) eGFP expressing MDA-MB-231 cells taken 76 hours post-incubation with siRNA encapsulated liposomes. Fluorescence values are taken at 595 nm. Resorufin fluorescence excitation: 560 nm, emission: 575-700 nm, and cutoff: 590 nm.

After evaluating the various siRNA concentrations, we proceeded with 50 nM and 1000 nM concentrations for observation of mVenus knockdown in MOLM-14 cells. The study broadened to include formulations using MCLM, MoChol, and MCLF encapsulating mVG siRNA. Further, the same particle types encapsulating fully fluorinated siRNA's were also tested. The newly obtained data (Figure 3.6A) showed minimal differences in knockdown activity for all samples at both concentrations when compared to the non-treated sample, indicating little to no siRNA activity. Thankfully, the resazurin assay showed no significant toxicity compared to the untreated control for the majority of investigated samples (Figure 3.5). The notable exception to this was the MCLF-based

liposomes encapsulating mVG-F siRNA. One might suspect that fluorinated siRNA is the culprit for this toxicity, however, this would not align with results seen from other particles encapsulating the same modified siRNA (Figure 3.6B). Further, it does not appear that the toxicity arises from the MCLF-based particles. These particles encapsulating mVG siRNA showed viability that was similar to the non-treated sample.

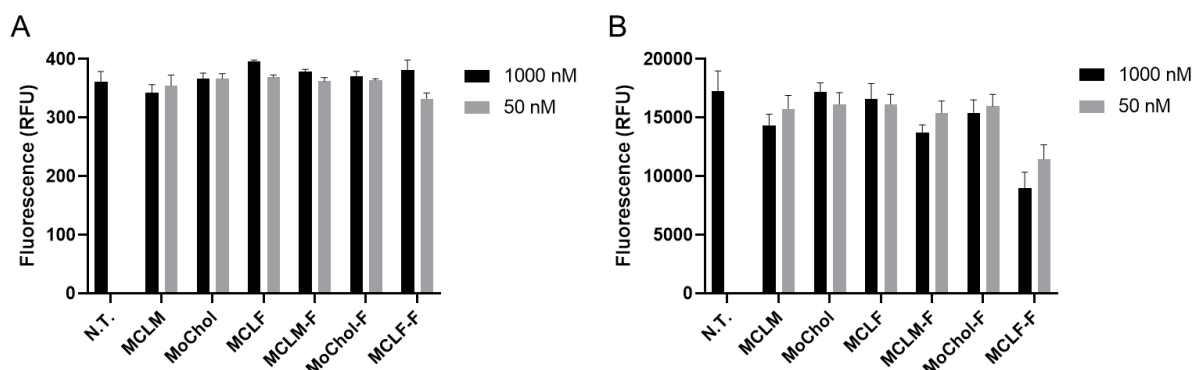


Figure 3.6. Fluorescence (RFU) measurements for (A) mVenus expressing MOLM-14 cells taken 72 hours post-incubation with siRNA encapsulated liposomes containing the MCLM, MoChol and MCLF ionizable lipids, (B) resorufin fluorescence as a function of cell viability. Samples marked with “-F” are indicative of liposomes encapsulating mVG-F siRNA with unmarked samples encapsulating mVG siRNA. Fluorescence was measured at 530 nm for mVenus and 595 nm for resorufin. Error bars represent S.E.M. Fluorescence for mVenus (MOLM-14) was measured at excitation: 480 nm, emission: 500-620 nm, cutoff: 515 nm, resorufin fluorescence excitation: 560 nm, emission: 575-700 nm, and cutoff: 590 nm.

To measure the relative toxicity of the liposomal formulations themselves, particles encapsulating unmodified tRNA were produced so we could gain a better understanding of the origin of cellular toxicity. We have shown that tRNA encapsulated in liposomes does not influence mVenus activity in a manner that aligns with gene knockdown (Figure 3.7A). The data received by means of resorufin fluorescence indicate that none of the tRNA-liposomes show toxicity when compared to non-treated cells (Figure 3.7B). This trend aligns with what was previously seen with all particles encapsulating mVG siRNAs but does not provide clarity for the observed toxicity for MCLF particles encapsulating fully fluorinated siRNA.

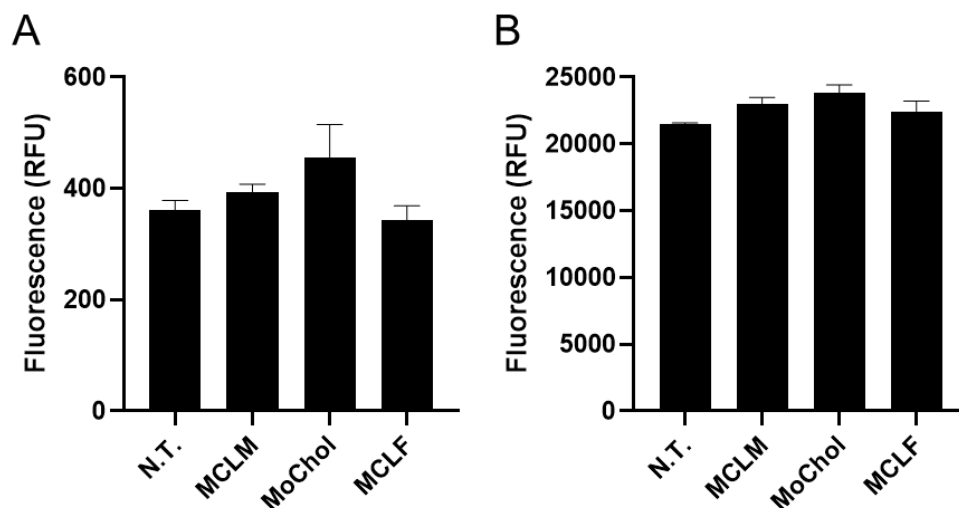


Figure 3.7. Cellular toxicity measurements using each synthesized lipid and encapsulating tRNA. Fluorescence (RFU) measurements for (A) mVenus expressing MOLM-14 cells taken 72 hours post-incubation (B) resorufin fluorescence 76 hours post-incubation as a function of cell viability. Fluorescence was measured at 530 nm for mVenus and 595 nm for resorufin. Error bars represent S.E.M. Fluorescence for mVenus (MOLM-14) was measured at excitation: 480 nm, emission: 500-620 nm, cutoff: 515 nm, resorufin fluorescence excitation: 560 nm, emission: 575-700 nm, and cutoff: 590 nm.

Liposomes using the MCLF **(4)** ionizable lipid and encapsulating fluorinated siRNA likely require further investigation into cellular toxicity. Our results showed that particles containing the MCLF lipid are non-toxic when encapsulating either unmodified siRNA or tRNA, indicating that the particles themselves are not the origin of the observed toxicity. Conversely, other particle types (containing MCLM **(2)** or MoChol **(8)** lipids) did not show the same toxicity as MCLF-based particles. This, coupled with the general stability and non-toxic nature of fluorinated oligonucleotides suggests that toxicity did not arise from the mVG-F siRNA either. These results further justify the continued investigation of the MCLF-particle and fluorinated siRNA combination to make more conclusive claims with respect to their toxicity. Based on our reported data, we can describe our liposome formulations as generally non-toxic which is consistent with the classification of liposomes. [95] While we were unable to see significant gene knockdown for mVenus or eGFP, we have shown that these liposomes are taken into cells. One suggestion apart from a random inconsistent result would be incompatibility of the siRNA sequences with the cell lines of choice. [96] It has been previously reported that the cell line of choice could play an important role in mRNA cleavage and subsequent gene knockdown. [96]

In our case, this is certainly plausible as our siRNA sequence was obtained from previous literature and was used with different cell types including astrocytes and microglial cells. [94] To offset this, a sequence designed and used for cancer cell lines would be more appropriate.

3.3. Conclusions and future perspectives

In summary, we have successfully synthesized several cholesteryl carbamate derivatives and implemented each into liposomes using a previously established protocol and formula. We have characterized each particle type with respect to their size, zeta potential and polydispersity index using dynamic light scattering. Further, particle physical morphologies were evaluated using Cryo-TEM. We have also shown that our formulated liposomes are capable of being taken up by cells and are generally non-toxic. One of our main goals was to evaluate the fluororous effect using particles containing fluorinated lipids. Particles containing the MCLF lipid **(4)** showed slightly larger diameters, lower RNA encapsulation efficiencies and more consistent unilamellar morphology than non-fluorinated counterparts (Section 2.2). Implementation of mVG-F siRNA into liposome systems with MCLF **(4)** revealed negligible changes with respect to particle size, polydispersity, and RNA encapsulation (Section 2.2.). From the perspective of physical characteristics, we were unable to generate sufficient evidence to support the presence of the fluororous effect. Liposomes of this type showed cellular uptake similar to non-fluorinated counterparts and were slightly more toxic, and even more so when encapsulating mVG-F siRNA (Sections 3.1.3 and 3.2.2.). In this case, however, it cannot be concluded as to the origin of said toxicity. Based on the observed uptake, it was suggested that the chosen siRNA sequence was did not show significant knockdown activity due to incompatibility with the utilized cell lines.

The lack of significant evidence to support the presence of the fluororous effect warrants further investigation. It is likely that the level of fluorination of MCLF **(4)** is not sufficient to facilitate this effect and that a more “perfluorinated” character is necessary. As such, the synthesis of more heavily fluorinated, ionizable lipids could aid in observing this effect in liposomal systems. The lack of significant knockdown was perhaps due to the mentioned cell incompatibility. To offset this, the use of a sequence validated for the cell

lines of use would be more beneficial. Furthermore, this could be used to rule out the possibility that the liposomes are not being released from the endosomes.

4. Experimental

General experimental:

Cholesteryl chloroformate, 4-(2-aminoethyl) morpholine, 1-(2-aminoethyl)piperidine, 2,2,3,3,4,4,4-heptafluorobutylamine, butylamine, and cholesteryl hemisuccinate (Avanti Polar Lipids) were all purchased from Sigma Aldrich and used without further purification. 4,4-difluoroaminoethylpiperidine was purchased from Oakwood Chemical. NMR data was obtained using a Bruker AV500. Chemical shift values (δ) are reported in parts per million (ppm) and are relative to residual solvent peaks. Coupling constants (J) are given in Hertz (Hz). Mass spectra were obtained using a Bruker MaXis high-resolution QTOF and values are given in mass to charge ratio (m/z). DOPE, POPC, and cholesteryl hemisuccinate (Avanti Polar Lipids) were all purchased from Sigma Aldrich. Unmodified siRNA sequences (Sense: 5'-GCACGACUUCUUCAAGUCCGCCA[dT][dT]-3' and Antisense: 5'-phos-UGGCGGACUUGAAGAAGUCGUGC[dT][dT] - 3') were obtained from Integrated DNA Technologies (IDT), and tRNA (brewers yeast) was purchased from Sigma Aldrich.

(2): 10,13-dimethyl-17-(6-methylheptan-2-yl)-2,3,4,7,8,9,10,11,12,13,14,15,16,17-tetradecahydro-1H-cyclopenta[a]phenanthren-3-yl (2-morpholinoethyl) carbamate

Procedure: Cholesteryl chloroformate (**1**) (0.2 g, 0.45 mmol, 1 eq.) was dissolved in 3 mL dry DCM. To this solution, 236 μ L of 4-(2-aminoethyl) morpholine (0.263 g, 1.8 mmol, 4 eq.) was added dropwise. The reaction was stirred for ~20 hours at room temperature, under argon atmosphere. The resulting solution was extracted with dH₂O (adjusted to pH 8.0 with sat. NaHCO₃) and the organic phase was subsequently evaporated, and the product (**2**) was dried under vacuo. Yield 30%. Characterization: ¹H NMR (500 MHz, CDCl₃) δ : 5.37 (dt, J = 4.8, 2.0 Hz, 1H), 5.08 (s, 1H), 4.50 (t, J = 5.1 Hz, 1H), 3.70 (t, J = 4.7 Hz, 5H), 3.28 (q, J = 5.7 Hz, 2H), 2.50 – 2.41 (m, 4H), 2.44 (s, 4H), 2.41 – 2.24 (m, 3H), 2.04 – 1.77 (m, 5H), 1.62 – 1.29 (m, 7H), 1.29 – 0.84 (m, 24H), 0.67 (s, 3H). ¹³C NMR (126 MHz, CDCl₃) δ : 156.27, 140.00, 122.65, 77.41, 77.16, 76.91, 74.47, 67.10, 57.64, 56.84, 56.28, 53.51, 50.16, 42.46, 39.89, 39.67, 38.75, 37.16, 36.72, 36.33, 35.95, 32.06, 32.03, 28.38, 28.35, 28.17, 24.44, 23.98, 22.97,

22.71, 21.19, 19.48, 18.86, 12.01. HRMS (ESI) = 565.4334 ([M+Na]⁺ calculated 565.4417).

(3): 10,13-dimethyl-17-(6-methylheptan-2-yl)-2,3,4,7,8,9,10,11,12,13,14,15,16,17-tetradecahydro-1H-cyclopenta[a]phenanthren-3-yl (2-(piperidin-1-yl) ethyl) carbamate

Procedure: Cholesteryl chloroformate (**1**) (0.2 g, 0.45 mmol, 1 eq.) was dissolved in 3 mL dry DCM. To this solution, 255 μ L of 1-(2-aminoethyl)piperidine (0.234 g, 1.8 mmol, 4 eq.) was added dropwise. The reaction was stirred for ~20 hours at room temperature, under argon atmosphere. The resulting solution was extracted with dH₂O (adjusted to pH 8.0 with sat. NaHCO₃) and the organic phase was subsequently evaporated and the product (**3**) was dried under vacuo. Yield 31%. Characterization: ¹H NMR (500 MHz, CDCl₃) δ : 5.37 – 5.32 (m, 1H), 5.21 (d, J = 6.3 Hz, 1H), 4.47 (tt, J = 11.6, 5.0 Hz, 1H), 3.22 (s, 2H), 2.38 (t, J = 6.3 Hz, 2H), 2.34 (s, 5H), 2.33 (s, 1H), 2.26 (t, J = 12.4 Hz, 1H), 2.02 – 1.94 (m, 2H), 1.94 – 1.86 (m, 1H), 1.57 (d, J = 10.0 Hz, 1H), 1.56 – 1.44 (m, 9H), 1.41 (dt, J = 12.6, 6.2 Hz, 4H), 1.36 – 1.29 (m, 4H), 1.26 – 1.20 (m, 1H), 1.18 – 1.02 (m, 7H), 1.02 – 0.87 (m, 9H), 0.87 – 0.81 (m, 7H), 0.65 (s, 3H). ¹³C NMR (126 MHz, CDCl₃) δ : 156.25, 140.00, 125.32, 122.47, 122.39, 77.41, 77.16, 76.91, 74.21, 62.22, 57.83, 56.78, 56.23, 54.86, 54.44, 50.11, 42.40, 39.84, 39.61, 38.71, 37.62, 37.12, 36.65, 36.28, 35.89, 32.00, 31.97, 28.33, 28.29, 28.10, 26.06, 24.51, 24.38, 23.93, 22.92, 22.67, 21.14, 19.43, 18.81, 11.95. HRMS (ESI) = 541.4729 ([M+H]⁺ calculated 541.4728).

(4): 10,13-dimethyl-17-(6-methylheptan-2-yl)-2,3,4,7,8,9,10,11,12,13,14,15,16,17-tetradecahydro-1H-cyclopenta[a]phenanthren-3-yl (2-(4,4-difluoropiperidin-1-yl) ethyl) carbamate

Procedure: Cholesteryl chloroformate (**1**) (0.2 g, 0.45 mmol, 1 eq.) was dissolved in 3 mL dry DCM. To this solution, 266 μ L 4,4-difluoroaminoethylpiperidine (0.296g, 1.8 mmol, 4 eq.) was added dropwise. The reaction was stirred for ~20 hours at room temperature, under argon atmosphere. The resulting solution was extracted with dH₂O (adjusted to pH 8.0 with sat. NaHCO₃), and the organic phase was subsequently evaporated, and the product (**4**) was dried under vacuo. Yield 22%. Characterization: ¹H NMR (500 MHz, CDCl₃) δ : 5.37 (dt, J = 5.6, 2.1 Hz, 1H), 5.03 (s, 1H), 4.51 (td, J = 10.5,

5.2 Hz, 1H), 3.26 (t, $J = 5.8$ Hz, 2H), 2.61 – 2.48 (m, 7H), 2.37 (ddd, $J = 13.0, 5.1, 2.1$ Hz, 1H), 2.33 – 2.23 (m, 1H), 1.98 (tdd, $J = 17.4, 6.7, 4.1$ Hz, 7H), 1.92 – 1.77 (m, 2H), 1.62 – 1.34 (m, 7H), 1.37 – 1.15 (m, 5H), 1.18 – 1.11 (m, 2H), 1.14 – 1.06 (m, 2H), 1.01 (s, 3H), 1.08 – 0.95 (m, 2H), 0.95 (q, $J = 5.5$ Hz, 1H), 0.92 (s, 2H), 0.92 – 0.84 (m, 8H), 0.67 (s, 3H). ^{13}C NMR (126 MHz, CDCl_3) δ : 156.24, 139.97, 122.67, 122.04, 77.41, 77.16, 76.91, 74.50, 56.83, 56.34, 56.28, 50.16, 49.97, 42.46, 39.88, 39.66, 38.74, 37.90, 37.15, 36.72, 36.33, 35.94, 34.30, 34.11, 33.93, 32.06, 32.02, 29.85, 28.38, 28.34, 28.16, 24.44, 23.98, 22.97, 22.71, 21.19, 19.48, 18.86, 12.00. ^{19}F NMR (471 MHz, CDCl_3) δ : -97.84. HRMS (ESI) = 577.4526 ($[\text{M}+\text{H}]^+$ calculated 577.4539).

(5): 10,13-dimethyl-17-(6-methylheptan-2-yl)-2,3,4,7,8,9,10,11,12,13,14,15,16,17-tetradecahydro-1H-cyclopenta[a]phenanthren-3-yl (2,2,3,3,4,4,4-heptafluorobutyl) carbamate

Procedure: Cholesteryl chloroformate (**1**) (0.2 g, 0.45 mmol, 1 eq.) was dissolved in 3 mL dry DCM. To this solution, 246 μL of 2,2,3,3,4,4,4-heptafluorobutylamine (0.358 g, 1.8 mmol, 4 eq.) was added dropwise. The reaction was stirred for ~20 hours at room temperature, under argon atmosphere. The resulting solution was extracted with dH_2O (adjusted to pH 8.0 with sat. NaHCO_3), and the organic phase was subsequently evaporated, and the product (**5**) was dried under vacuo. Yield 91%. Characterization: ^1H NMR (500 MHz, CDCl_3) δ : 5.38 (dt, $J = 5.3, 2.1$ Hz, 1H), 4.93 (t, $J = 6.6$ Hz, 1H), 4.53 (tt, $J = 9.4, 3.8$ Hz, 1H), 3.90 (td, $J = 15.4, 6.6$ Hz, 2H), 2.41 – 2.25 (m, 3H), 2.05 – 1.77 (m, 5H), 1.63 – 1.23 (m, 9H), 1.26 – 0.84 (m, 25H), 0.68 (s, 3H). ^{13}C NMR (126 MHz, CDCl_3) δ : 155.85, 139.61, 122.97, 118.88, 116.59, 114.88, 77.41, 77.16, 76.91, 75.79, 56.83, 56.30, 50.14, 42.46, 41.22, 41.03, 40.84, 39.88, 39.67, 38.45, 37.05, 36.68, 36.34, 35.95, 32.04, 32.01, 28.38, 28.16, 28.11, 24.43, 23.99, 22.96, 22.70, 21.19, 19.45, 18.86, 12.00. ^{19}F NMR (471 MHz, CDCl_3) δ : -80.78, -119.82, -127.81. HRMS (ESI) = 634.3483 ($[\text{M}+\text{Na}]^+$ calculated 634.3470).

(6): 10,13-dimethyl-17-(6-methylheptan-2-yl)-2,3,4,7,8,9,10,11,12,13,14,15,16,17-tetradecahydro-1H-cyclopenta[a]phenanthren-3-yl butylcarbamate

Procedure: Cholesteryl chloroformate (**1**) (0.2 g, 0.45 mmol, 1 eq.) was dissolved in 3 mL dry DCM. To this solution, 178 μL of butylamine (1.8 mmol, 4 eq.) was added dropwise. The reaction was stirred for ~20 hours at room temperature, under argon

atmosphere. 5 mL of H₂O (adjusted to pH 8.0 with sat. NaHCO₃) was added to quench the reaction for 2 minutes. The solution was extracted with DCM and the aqueous layer was washed with 3x 5 mL of DCM. The organic layers were isolated, dried over Mg₂SO₄ and subsequently evaporated under vacuo. Yield: 72%. ¹H NMR (500 MHz, CDCl₃) δ: 5.37 – 5.31 (m, 1H), 4.70 (t, *J* = 5.9 Hz, 1H), 4.46 (tt, *J* = 11.0, 4.2 Hz, 1H), 3.13 (q, *J* = 6.8 Hz, 2H), 2.38 – 2.30 (m, 1H), 2.23 (t, *J* = 12.5 Hz, 1H), 2.02 – 1.86 (m, 2H), 1.86 – 1.75 (m, 3H), 1.60 – 1.37 (m, 6H), 1.39 – 1.26 (m, 5H), 1.22 (tt, *J* = 15.3, 10.2 Hz, 1H), 1.18 – 1.07 (m, 7H), 1.07 – 1.01 (m, 1H), 0.98 (s, 5H), 1.01 – 0.90 (m, 2H), 0.93 – 0.81 (m, 15H), 0.65 (s, 3H). ¹³C NMR (126 MHz, CDCl₃) δ: 156.24, 139.93, 122.47, 77.41, 77.16, 76.90, 74.14, 56.76, 56.23, 50.08, 42.38, 40.68, 39.82, 39.60, 38.68, 37.09, 36.62, 36.27, 35.89, 32.19, 31.97, 31.95, 28.32, 28.28, 28.08, 24.36, 23.94, 22.91, 22.65, 21.13, 20.00, 19.41, 18.80, 13.83, 11.93. HRMS (ESI) = 508.4121 ([M+Na]⁺ calculated 508.4130).

(7): 4-(2-(4-((10,13-dimethyl-17-(6-methylheptan-2-yl)-2,3,4,7,8,9,10,11,12,13,14,15,16,17-tetradecahydro-1*H*-cyclopenta[*a*]phenanthren-3-yl)oxy)-4-oxobutanamido)ethyl)morpholin-4-ium

Procedure: In a dry round bottom flask, cholesterol hemi succinate (**7**) (1.0g, 2.05mmol, 2 equiv.) and DMAP (12 mg, cat.) were dissolved in CH₂Cl₂ (10 ml) under argon. In a separate dry round bottom flask, DCC (0.212g, 1.025 mmol, 1 equiv.) was dissolved in CH₂Cl₂ (5ml) and then added to the stirring solution at 0°C and left for 3h. Following this, 4-(2-Aminoethyl)morpholine (135ul, 1.025 mmol, 1 equiv.) was added *in situ* at 0°C under argon and left for 24h at rt. The reaction was quenched with excess aqueous base (pH = 10.0). The organic and aqueous layers were allowed to separate, and the aqueous phase was extracted three times with CH₂Cl₂. The combined organic layers were washed three times with saturated NaCl, three times with K₂CO₃, and dried with MgSO₄. CH₂Cl₂ was evaporated off under reduced pressure affording the crude product. The crude product was isolated by column chromatography (DCM/ethyl acetate 4:1) to yield the final product (**8**). 79% yield. Characterization: ¹H NMR (500 MHz, CDCl₃) δ: 6.15 (s, 1H, alkene), 5.38 (s, 1H), 4.67-4.6 (m, 1H), 3.75-3.73 (5, *J* = 4.6Hz, 4H), 3.4-3.6 (q, *J* = 5.2, 11.5Hz, 2H), 2.68-2.66 (t, *J* = 7.1Hz, 2H), 2.516-2.45 (m, 7H), 2.354-2.31 (d, *J* = 7.1Hz, 2H), 2.06-1.96 (m, 2H), 1.91-1.81 (m, 3H), 1.62-1.22

(m, 12H), 1.22-0.85 (m, 22H), 0.69 (s, 3H). ^{13}C NMR (500 MHz, CDCl_3) δ : 172.41, 171.46, 139.62, 122.71, 74.36, 66.94, 57.03, 56.70, 56.14, 53.35, 50.03, 42.32, 39.74, 39.53, 38.11, 36.98, 36.61, 36.19, 35.80, 35.71, 31.92, 31.86, 31.14, 29.96, 28.24, 28.03, 27.78, 24.29, 23.84, 22.83, 22.58, 21.04, 19.32, 18.73, 11.87. HRMS (ESI) = 599.4812 ($[\text{M}+\text{H}]^+$ calculated 599.4782).

mVG-F siRNA synthesis and purification

mVG siRNA sequences were purchased from IDT as standard desalting products. RNA phosphoramidites, solid supports and other reagents were purchased from ChemGenes and Glen Research. Fluorinated siRNAs were synthesized on a 1.0 μmol scale using a Bioautomation Co. Mermade 4 DNA synthesizer according to the DMT-on procedure. All amidites were dissolved in ACN prior to use. RNA synthesis was monitored by DMT deprotection. Upon synthesis completion, RNA sequences were cleaved from the CPG solid support and deprotected using 1 mL of AMA at room temperature for 2 hours. The products were diluted with 1 mL of 100 mg/mL (aq) methylamine and sodium hydroxide (1:1) before purification with Glen-Pak columns to remove synthesis failures and to remove the 5'-DMT group. The resulting solutions were again concentrated and purified by ion exchange HPLC using the Agilent 1200 series HPLC system (DNAPac 063000 4 x 250 mm). The conditions used were 0-30% Buffer B over 30 minutes (Buffer A: 15 mM NaOAc, 25% ACN. Buffer B: 15 mM NaOAc, 25% ACN, 0.5 M LiClO_4) at a flow rate of 1 mL/min. Elution was monitored by UV absorption at 260 nm and products were dried, resuspended in water, and desalted using NAP-10 desalting columns (Glen Research) before quantification and further use.

Liposome formulation

30 nmol of siRNA sense and antisense strands were suspended in 0.6 mL of 200 mM sodium acetate solution at pH 5.5. This solution was heated to 70°C for mVG siRNAs and 80°C for mVG-F siRNAs. The used siRNA sequences was obtained from previous literature with slight modification (Sense: 5'-GCACGACUUCUUCAAGUCCGCCA[dT][dT]-3' and Antisense: 5'-phos-UGGCGGACUUGAAGAAGUCGUGC[dT][dT] - 3'). [3] Temperatures were maintained

for 5 minutes, and solutions were allowed to cool to room temperature for 1.5 hours before storage at 4°C. Before use, the pH of the solution was adjusted to 4.0 using ~0.25 mL of 0.84 M acetic acid, 0.2 M NaCl and adjusted to a final volume of 1.2 mL using 200 mM sodium acetate solution at pH 4.0. Lipids were weighed and dissolved in 0.4 mL of absolute ethanol to give a molar ratio of 6:24:23:47 for POPC, DOPE, CHEMS and one of the MCL- lipids respectfully. The lipid concentration was based upon the initial working volume of 1.6 mL. The two solutions in syringes were placed on syringe pumps to enter a PDMS microfluidic chip (Wunderlichips GmbH) with a herringbone structure to facilitate rapid and turbulent mixing. The aqueous RNA solution was set to a flow rate of 30 mL/hour while the ethanol lipid solution was set to 10 mL/hour to give a flow rate ratio of 3:1. The resulting liposomal suspension is met in a secondary mixing chip by ~0.5 mL of a 0.425 M sodium phosphate, 0.1 M NaCl solution, at pH 11 to raise the overall pH of the solution to pH 7.4-7.5 and to dilute the concentration of ethanol. Additional solution was added as necessary to achieve the desired pH value. The liposomal suspension was then extruded 15-17 times through a 0.2 µm polycarbonate membrane at 50°C and subsequently dialyzed overnight against 20% sucrose in 1X PBS, pH 7.5 using 100 kDa MWCO dialysis tubing.

Dynamic light scattering

Dynamic light scattering (DLS) and phase analysis light scattering (PALS) analyses were conducted using the NanoBrook OMNI (Brookhaven Instruments). Measurements of liposomal solutions in 1X PBS, pH 7.5 (20% sucrose) were completed at 20°C using a 90° scattering angle with a viscosity of 1.970 cP, auto baseline normalization, applied dust filter and a CONTIN size distribution. In the event of a poor baseline index, samples were filtered using a 0.2 µm PES sterile filter for bioburden reduction.

RNA encapsulation efficiency

RNA encapsulation efficiency was measured using the Quant-it RiboGreen RNA Assay Kit (Invitrogen). RNA samples of interest (siRNA or tRNA) were prepared, quantified and diluted to a concentration of 2 µg/mL using 1X TE buffer made from a 20X stock (200 mM Tris-HCl, 20 mM EDTA, pH 7.5 in DEPC H₂O). Further dilutions were made to generate stock standard solutions to give final concentrations (after dye addition) of 0,

0.02, 0.1, 0.5 and 1 µg/mL. RiboGreen dye in DMSO was diluted 200X in TE buffer in accordance with the high range standard curve protocol. Liposomal solutions were diluted 100X in 1X TE buffer (0.1% Triton X-100) and sonicated for 2 minutes to facilitate liposome rupture. 100 µL of all stock and liposome solutions were plated with 100 µL of diluted dye solution and incubated in the dark for 5 minutes before reading. Fluorescence measurements were taken using 480 nm excitation with a 500-620 nm emission output and an excitation cutoff of 495 nm. Fluorescence (RFU) maxima at 530 nm were used for standard curve generation and unknown RNA concentration determination. Unknown liposomal sample RNA fluorescence values were adjusted according to manufacturer instructions for triton X-100 interference.

Cryogenic transmission electron microscopy

Cryo-TEM images were obtained by Dr. Amal Seffouh (Department of Anatomy and Cell Biology, McGill University) using a FEI Titan Krios 300 kV Cryo-STEM.

tRNA reaction with ethidium bromide monoazide

In a 1.5 mL Eppendorf, 2 mg of ethidium bromide monoazide (4.7 µmol, 14 eq) was combined with 10 mg of tRNA from brewer's yeast (0.33 µmol, 1 eq) in 0.5 mL 1X PBS. The solution was subjected to 450 nm blue light for 2 hours to facilitate a photo-induced crosslink reaction. The irradiated sample was subjected to spin filtration using 3000 Da MWCO Amicon spin-filter with the addition of DEPC H₂O to remove any excess ethidium bromide monoazide. Reaction completion was observed by fluorescence spectroscopy and the resulting product was analyzed by analyzed by 15% denaturing polyacrylamide gel electrophoresis to confirm reaction completion.

Cell culture

Suspension MOLM-14 cells were cultivated at 37 °C, 5% CO₂ in 1X RPMI 1640 media (Gibco) containing 4.5 g/L glucose, 10% fetal bovine serum (Gibco), 50,000 units of Penicillin, and 50 mg of streptomycin (Sigma Aldrich). Cells were grown to confluency and passaged every 4 days 1:10 in fresh media. MDA-MB-231-eGFP cells were obtained from the lab of Professor Hanadi Sleiman. These cells were cultivated at 37 °C, 5% CO₂ using 1X DMEM (Gibco) containing 4.5 g/L glucose, 10% fetal bovine

serum (Gibco), 50,000 units of Penicillin, 50 mg of streptomycin (Sigma Aldrich) and 1% MEM non-essential amino acids (Sigma Aldrich). The cells were passaged 1:5 every 3 days in fresh media. Cells were counted using a BIO RAD TC20 cell counter to determine seeding density.

Cellular uptake visualization by confocal microscopy

Prior to visualization, and incubation, each well of an 8-well microscopy slide was coated in 150 μ L of 1 μ g/mL of fibronectin and incubated for at least 2 hours. Each well was washed 3X with 1X PBS (pH 7.5) after removing the fibronectin. MDA-MB-231 cells were pelleted at 300 xg for 5 minutes and resuspended in 1 mL of fresh 1X DMEM media (10% FBS and 1% antibiotic/antimycotic). Cells were seeded at 20,000 cells/mL and incubated overnight to allow for cell adherence. The following day, the existing media was aspirated, the cells were washed 3X with 1X PBS (pH 7.5) before the addition of 180 μ L of fresh media (no FBS). Liposome stock solutions containing ethidium bromide monazide modified tRNA were diluted to 20 μ M according to their RNA encapsulation efficiencies. 20 μ L of each sample was added to their respective wells to give a final RNA concentration of 2 μ M. The plate was incubated for 4 hours before visualization of uptake by confocal microscopy. Images were obtained using the Stellaris 5 LIAchroic confocal microscope (Leica Microsystems) equipped with a HC PL APO 20x multi-immersion objective (0.5 IMM CORR CS2), and a HC PL APO 63x/1.40 oil CS2 (FWD: 0.14 mm). For the observation of eGFP, a 488 nm excitation laser was used, and emission was measured from 500-550 nm. For the observation of ethidium bromide modified tRNA, a 561 nm excitation laser was used, and emission was measured from 575-700 nm.

siRNA Knockdown assay.

MOLM-14 and MDA-MB-231 cells expressing mVenus and eGFP respectively, were pelleted at 300xg for 5 minutes and resuspended in 4 mL of fresh 1X RPMI 1640 (1% antibiotic/antimycotic). The cells were plated in 90 μ L at a concentration of 100,000 cells/well for MOLM-14 and 10,000 for MDA-MB-231. This was followed by the addition of 10 μ L of liposomal solutions using varying concentrations of siRNA. The plate was incubated for 6 hours before the addition of 10 μ L of fetal bovine serum to each well.

Incubation continued for 66 hours and at 72 hours, 30 μ L of cell lysis buffer was added to each well and the plate was incubated for 5 minutes before fluorescence measurement. Fluorescence for mVenus (MOLM-14) was measured at excitation: 480 nm, emission: 500-620 nm, cutoff: 515 nm, while eGFP (MDA-MB-231) was measured at excitation: 460 nm, emission: 500-600 nm, cutoff: 495 nm.

Resazurin assay

MOLM-14 and MDA-MB-231 cells expressing mVenus and eGFP respectively, were pelleted at 300xg for 5 minutes and resuspended in 4 mL of fresh 1X RPMI 1640 (1% antibiotic/antimycotic). The cells were plated in 90 μ L at a concentration of 100,000 cells/well for MOLM-14 and 10,000 for MDA-MB-231. This was followed by the addition of 10 μ L of liposomal solutions using varying concentrations of siRNA. Additional wells were reserved for incubation with unmodified tRNA encapsulated liposomes (at maximum concentration) to observe any toxicity. The plate was incubated for 6 hours before the addition of 10 μ L of fetal bovine serum to each well. At the 72-hour time point 11 μ L of resazurin dye (870 μ M in 1X PBS) was added to well and the plate was incubated for an additional 4 hours, at which time fluorescence was read at excitation: 560 nm, emission: 575-700 nm, and cutoff: 590 nm.

5. Supplementary information

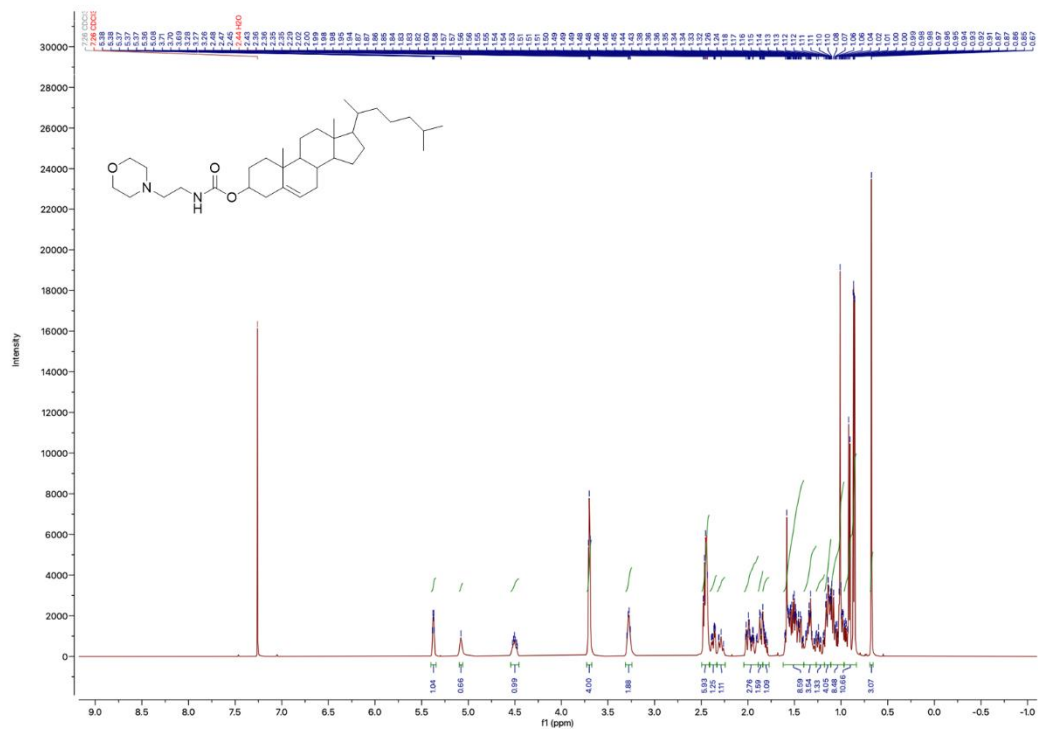


Figure S1. ^1H NMR (500 MHz, CDCl_3) for MCLM (**2**).

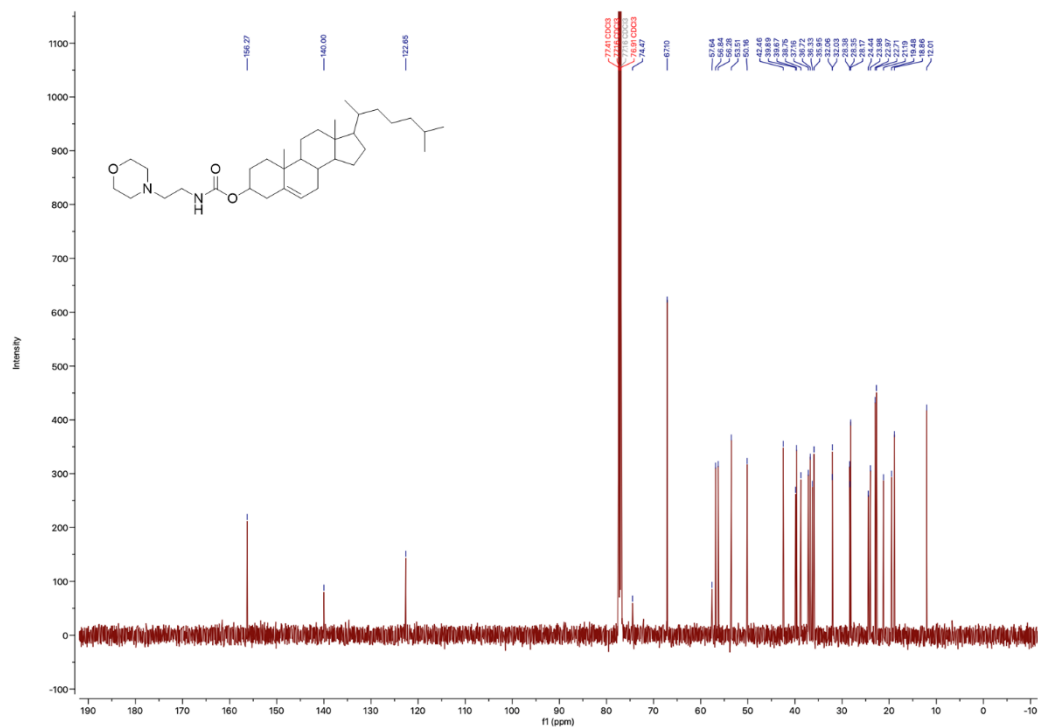


Figure S2. ^{13}C NMR (126 MHz, CDCl_3) for MCLM (**2**).

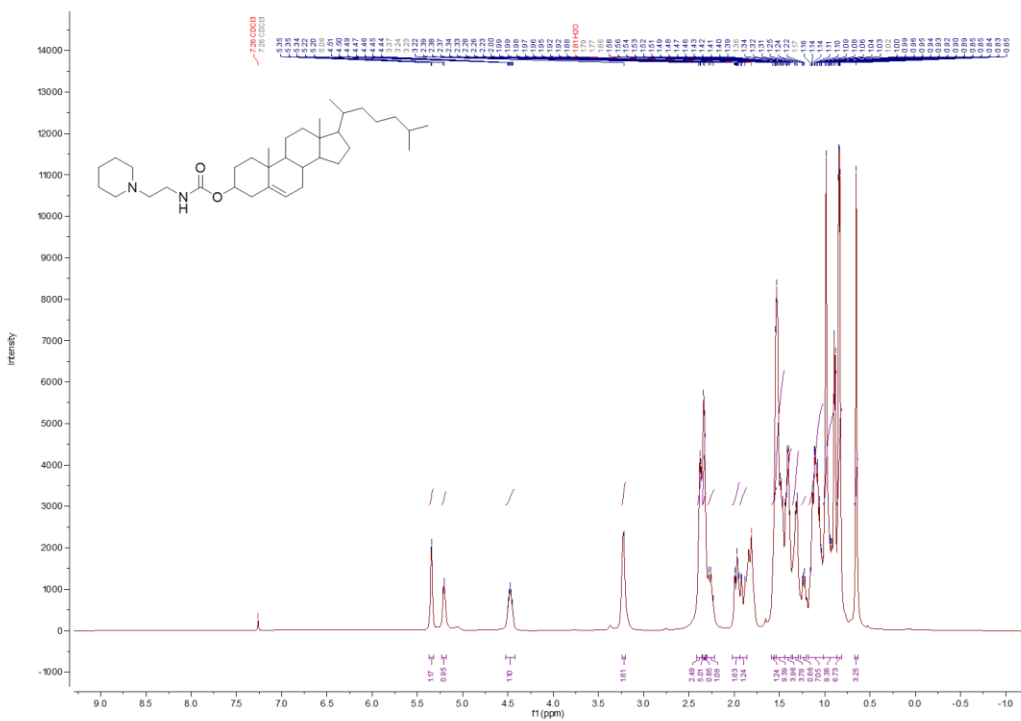


Figure S3. ¹H NMR (500 MHz, CDCl₃) for MCLP (3).

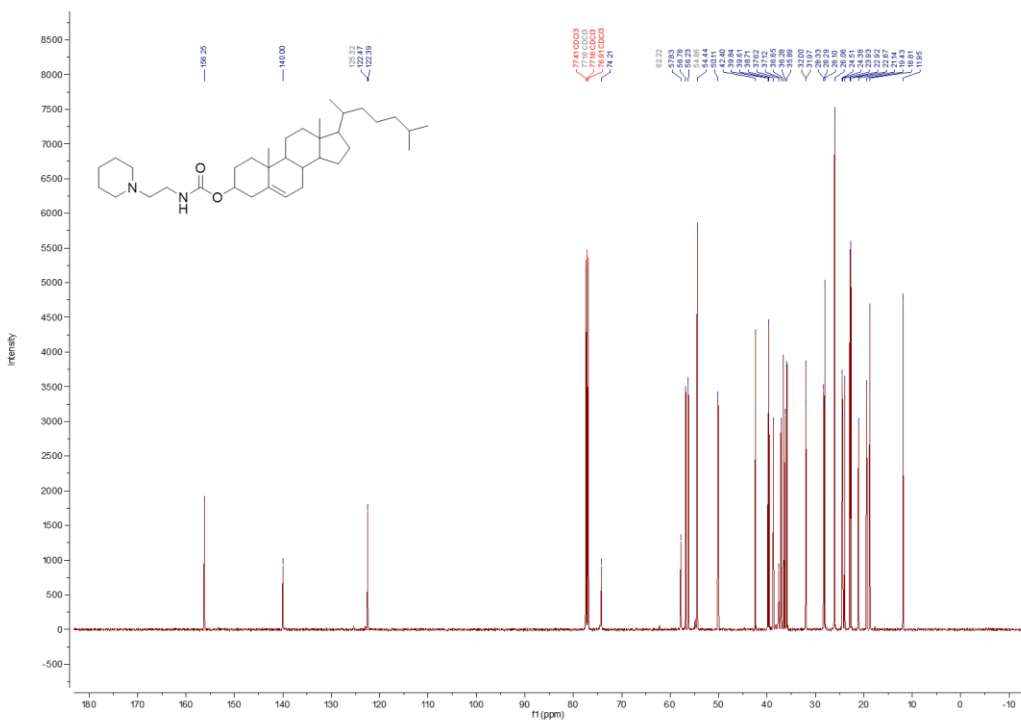


Figure S4. ¹³C NMR (126 MHz, CDCl₃) for MCLP (3).



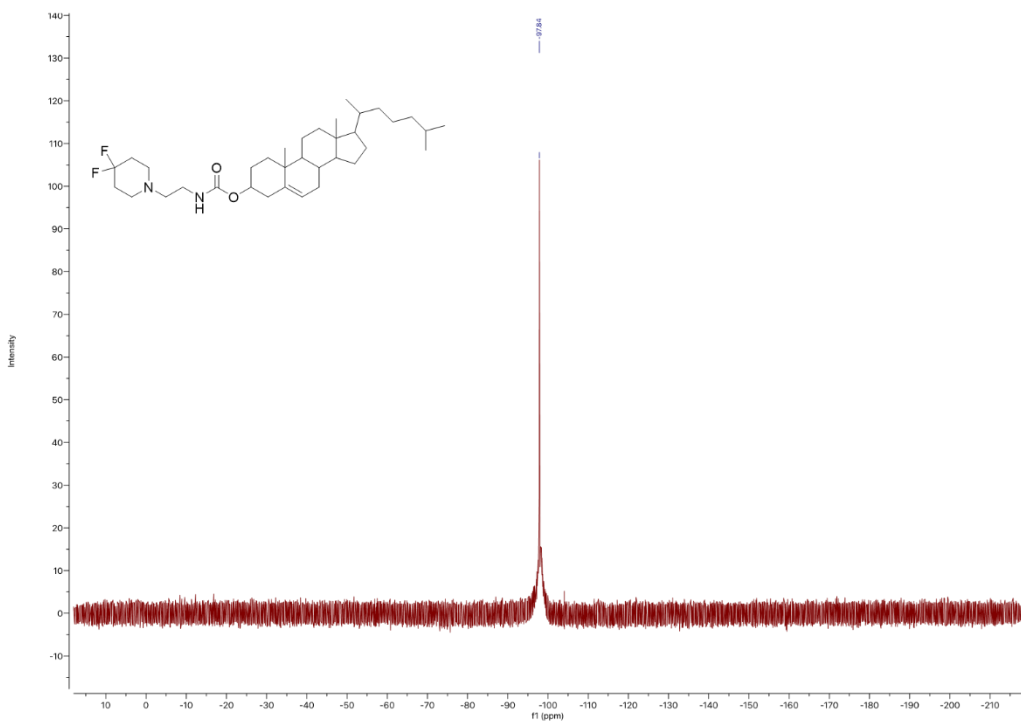


Figure S7. ^{19}F NMR (471 MHz, CDCl_3) for MCLF (4).

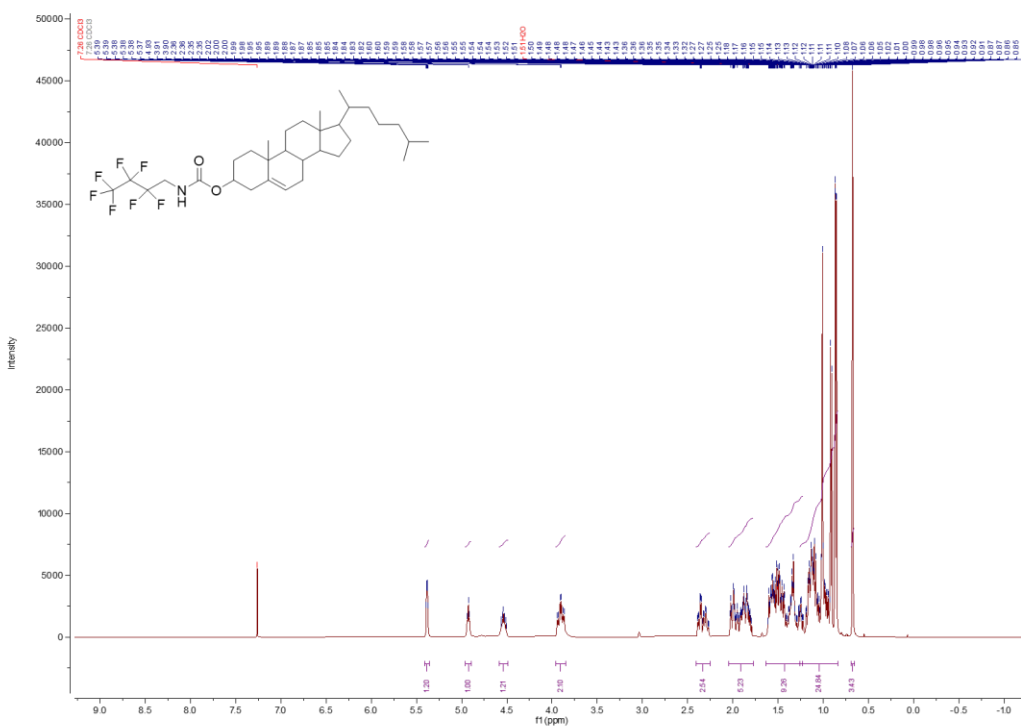


Figure S8. ^1H NMR (500 MHz, CDCl_3) for MCLH (5).

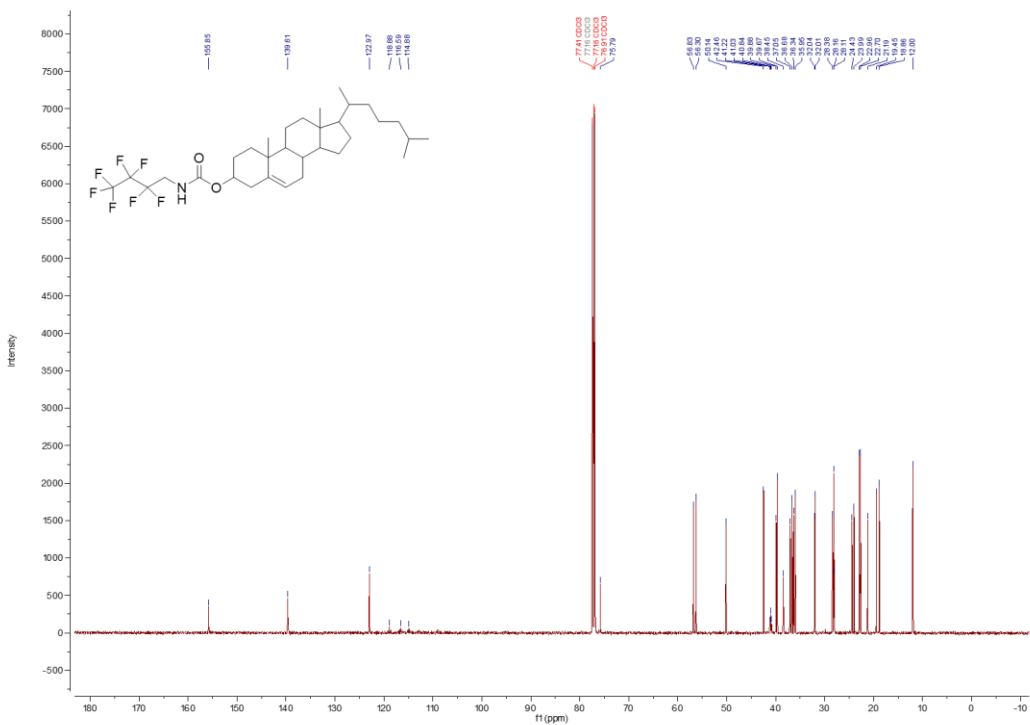


Figure S9. ¹³C NMR (126 MHz, CDCl₃) for MCLH (5).

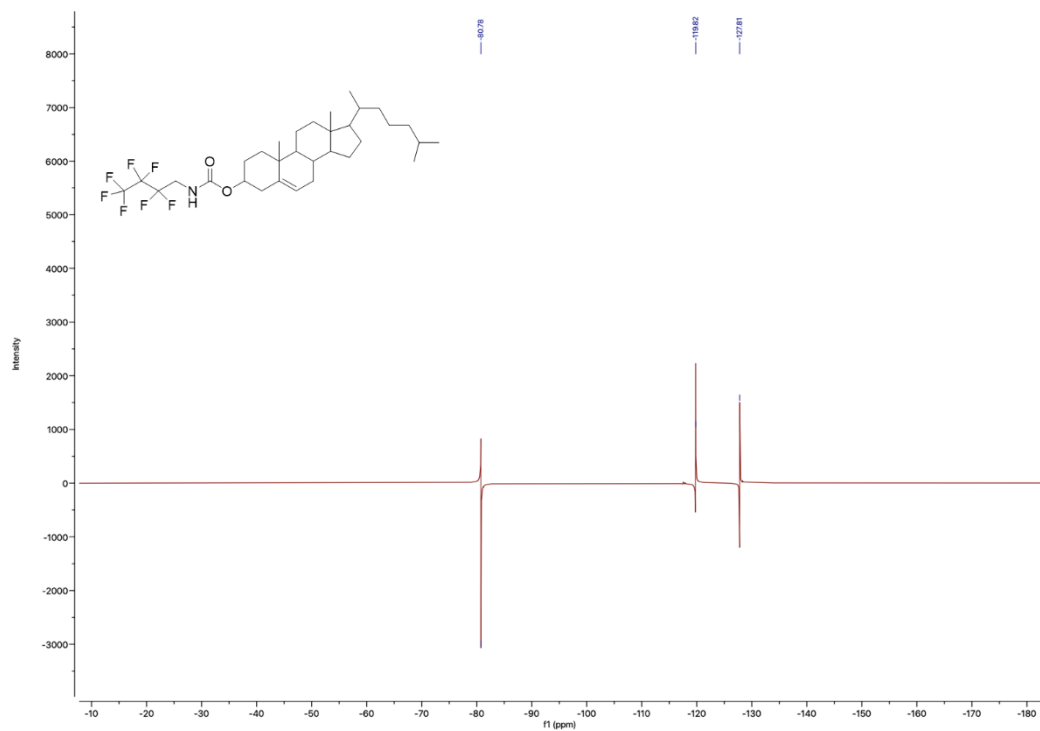
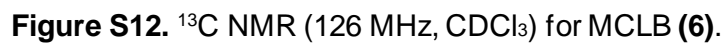


Figure S10. ¹⁹F NMR (471 MHz, CDCl₃) for MCLH (5).



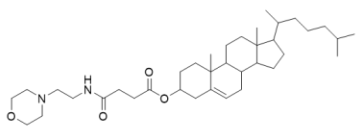


Figure S13. ^1H NMR (500 MHz, CDCl_3) for MoChol (**8**).

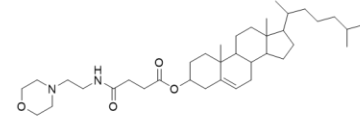


Figure S14. ^{13}C NMR (126 MHz, CDCl_3) for MoChol (**8**).

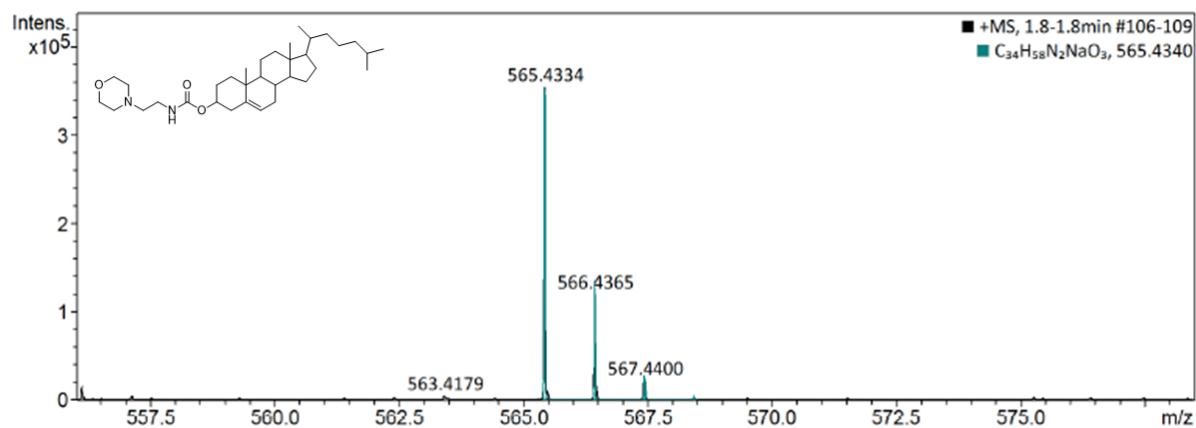


Figure S15. Deconvoluted HRMS spectrum for MCLM (2). Data was collected and analyzed by Dr. Alexander Wahba (McGill University).

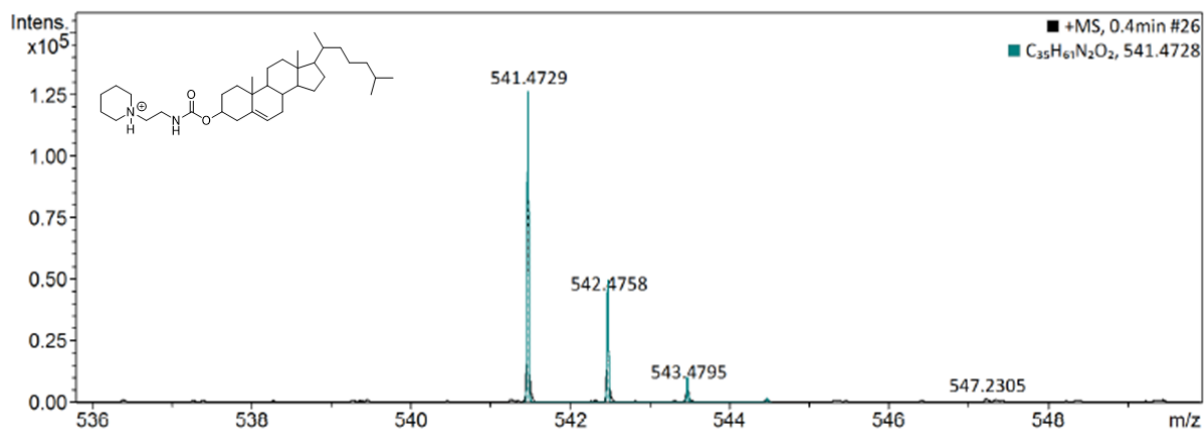


Figure S16. Deconvoluted HRMS spectrum for MCLP (3). Data was collected and analyzed by Dr. Alexander Wahba (McGill University).

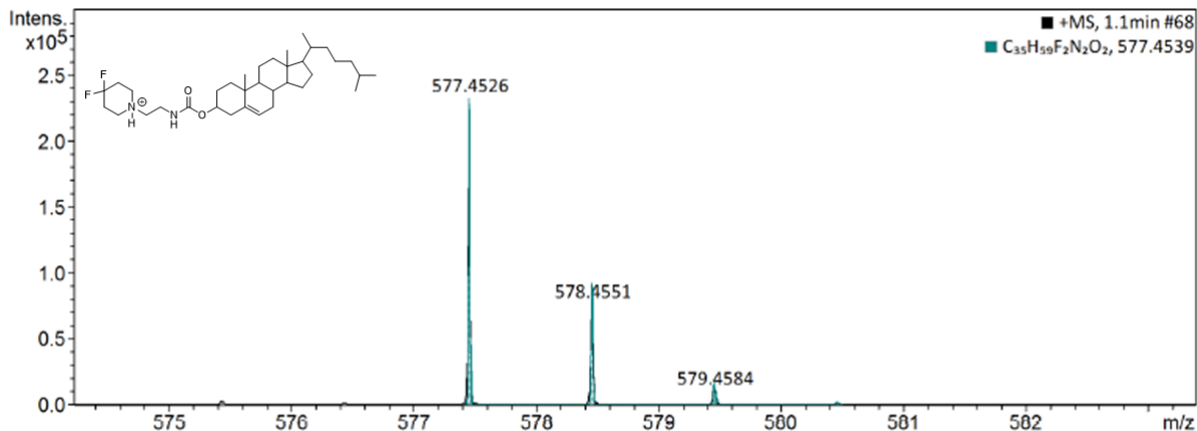


Figure S17. Deconvoluted HRMS spectrum for MCLF (4). Data was collected and analyzed by Dr. Alexander Wahba (McGill University).

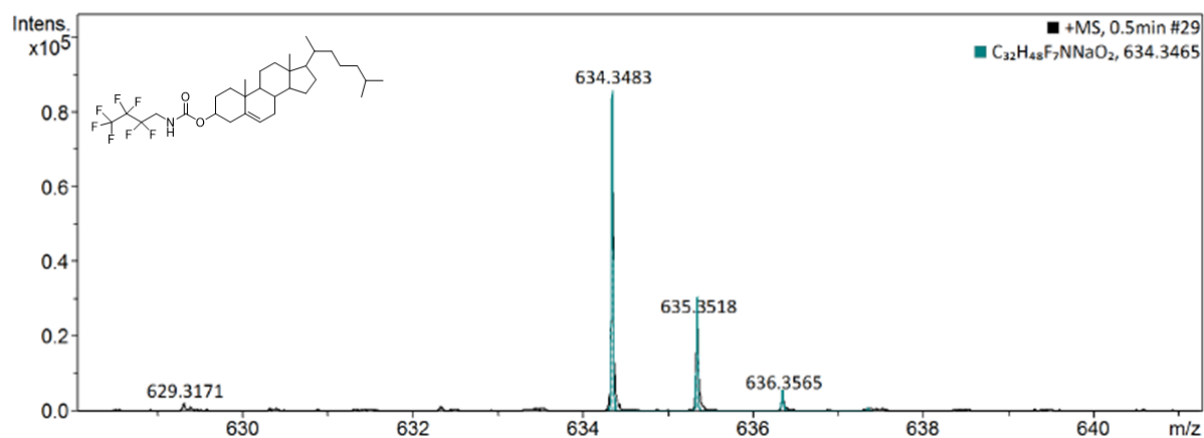


Figure S18. Deconvoluted HRMS spectrum for MCLH (5). Data was collected and analyzed by Dr. Alexander Wahba (McGill University).

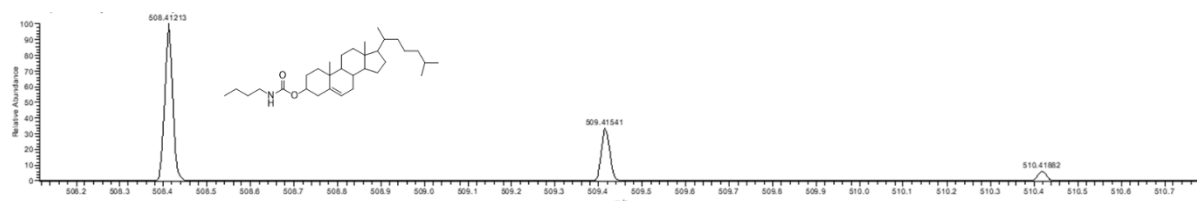


Figure S19. Deconvoluted HRMS spectrum for MCLB (6). Data was collected and analyzed by Nadim Saadeh (McGill University).

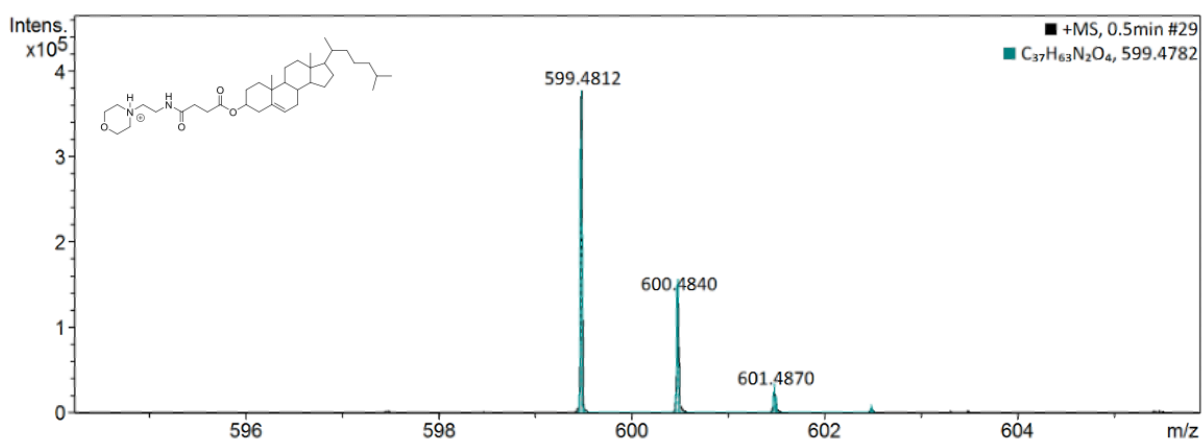


Figure S20. Deconvoluted HRMS spectrum for MoChol (8). Data was collected and analyzed by Dr. Alexander Wahba (McGill University).

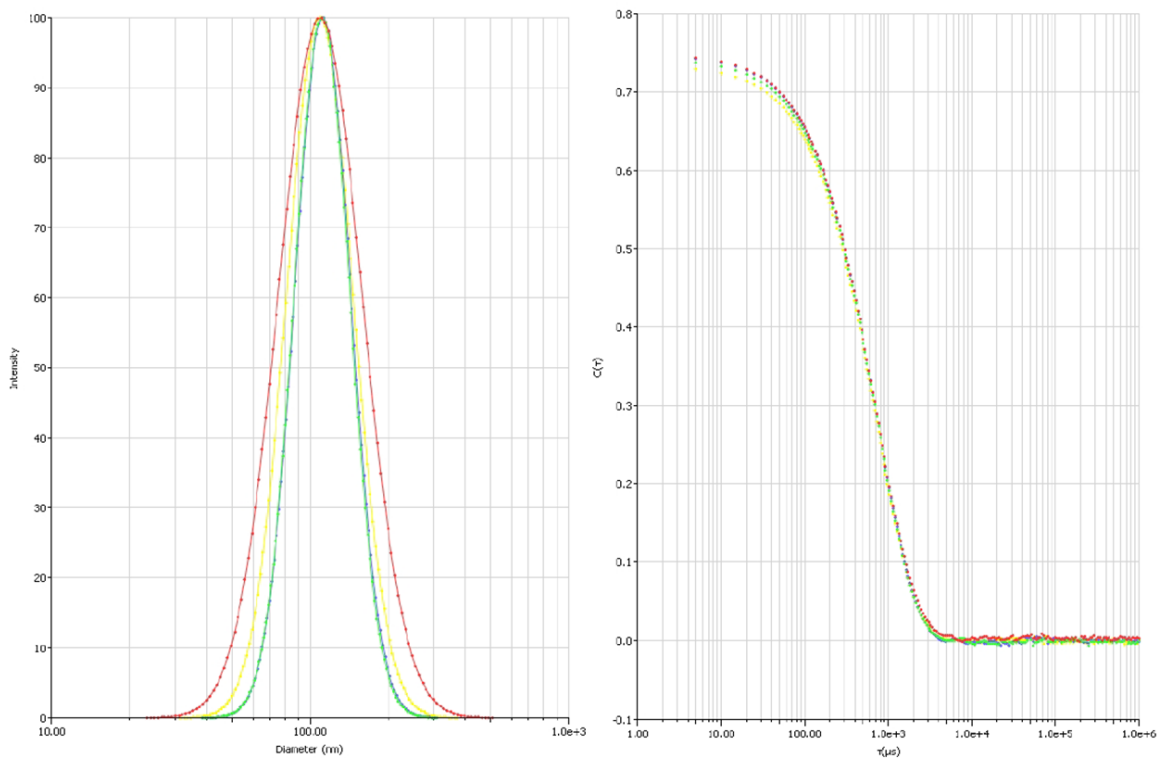


Figure S21. MCLM-based liposome particle sizing lognormal distribution (left) and correlation function (right).

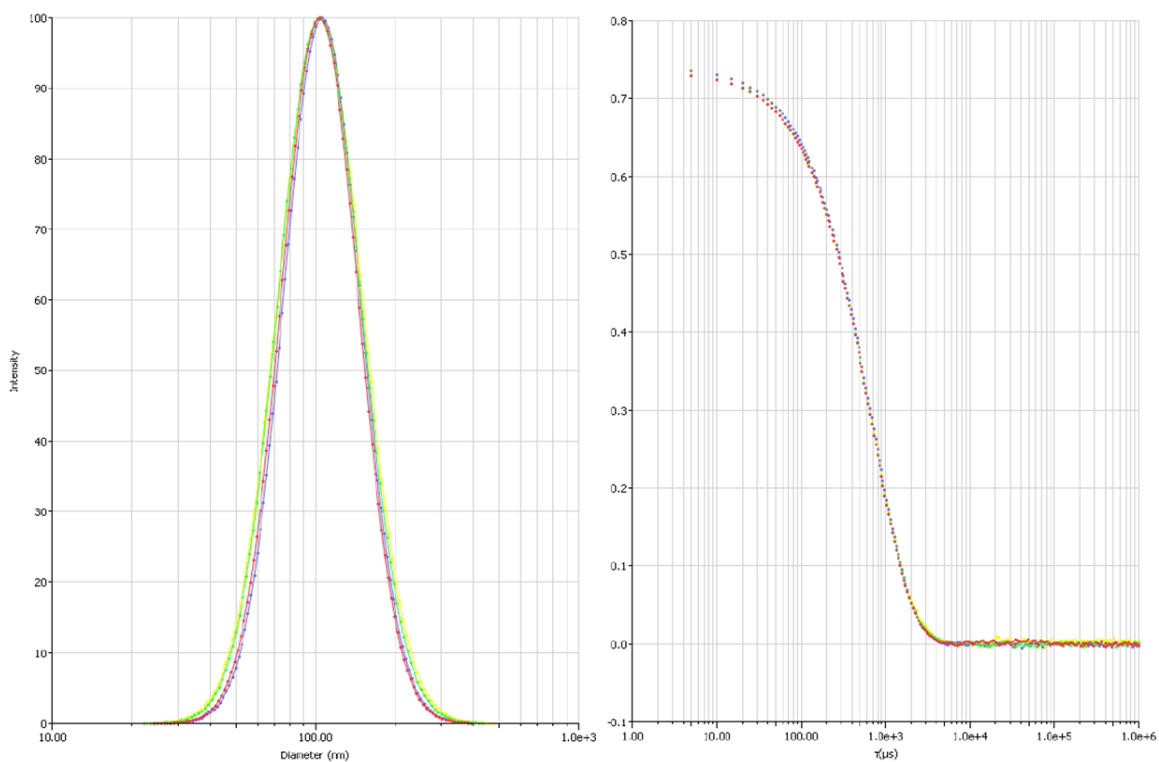


Figure S22. MoChol-based liposome particle sizing lognormal distribution (left) and correlation function (right).

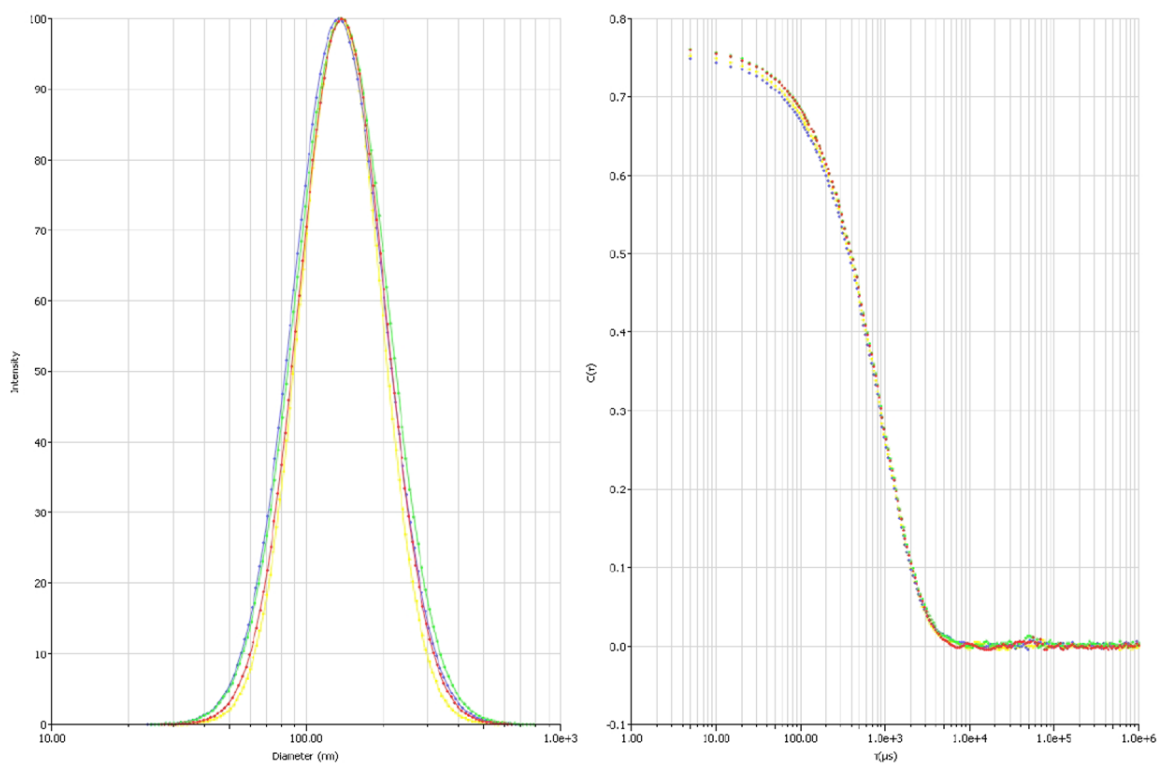


Figure S23. MCLF-based liposome particle sizing lognormal distribution (left) and correlation function (right).

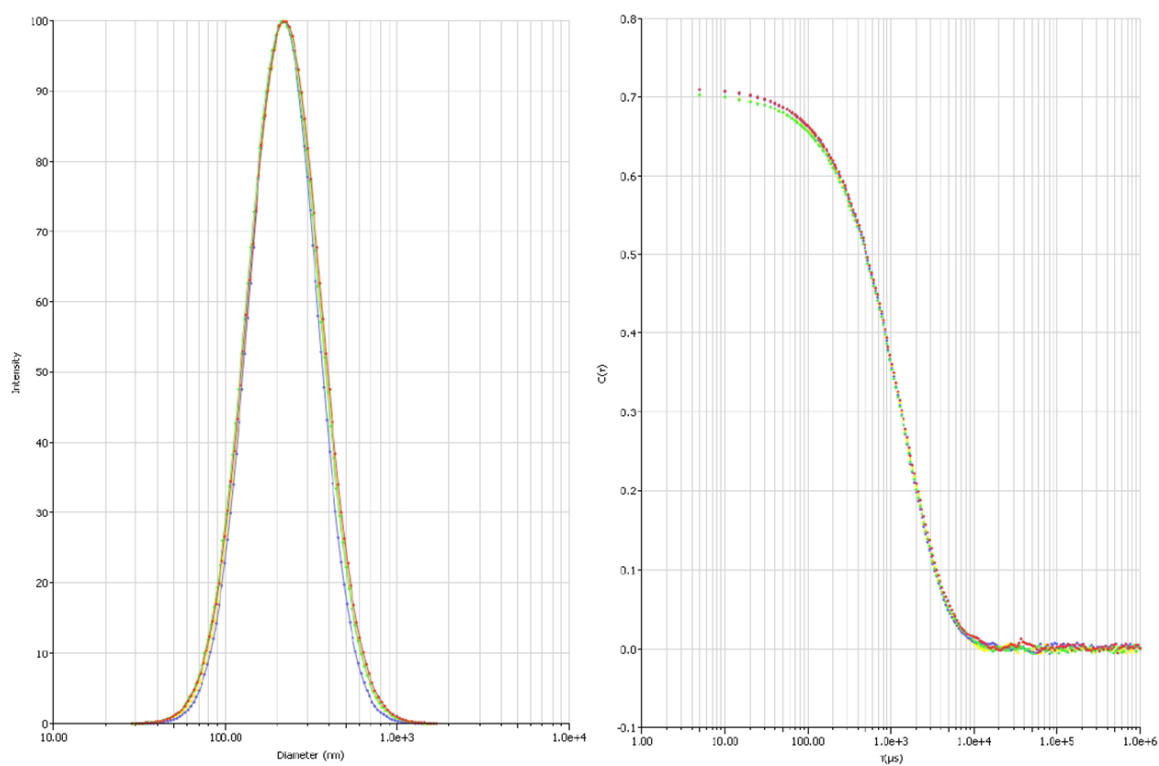


Figure S24. MCLH-based liposome particle sizing lognormal distribution (left) and correlation function (right).

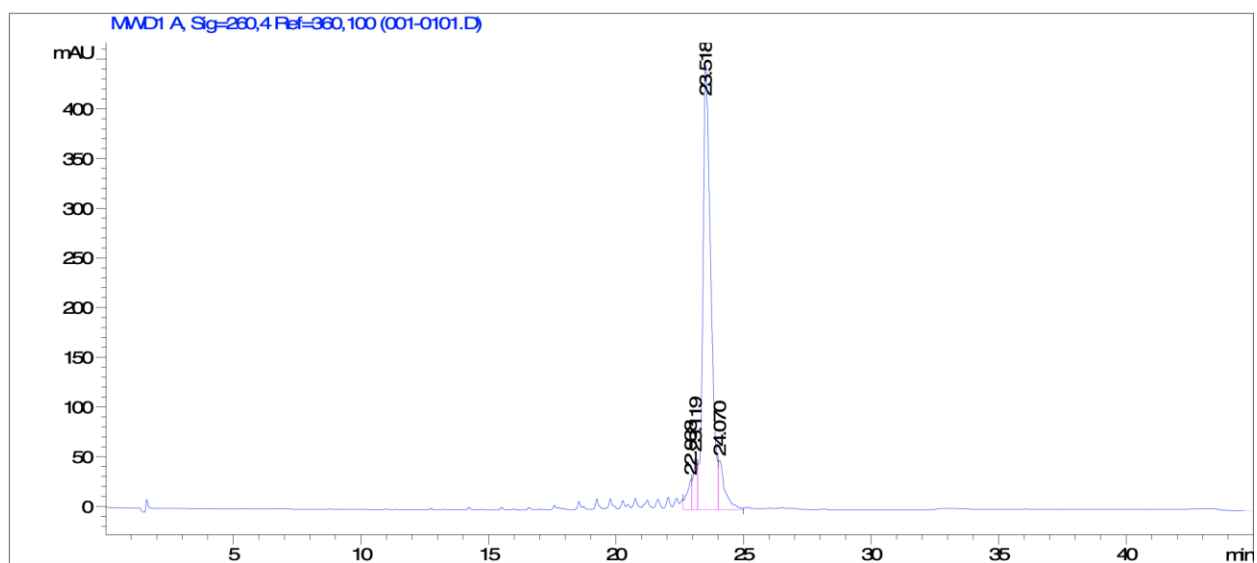


Figure S25. Analytical HPLC trace of unmodified siRNA sense strand Sense: 5'-GCACGACUUCUUCAAGUCCGCCA[dT][dT]-3'.

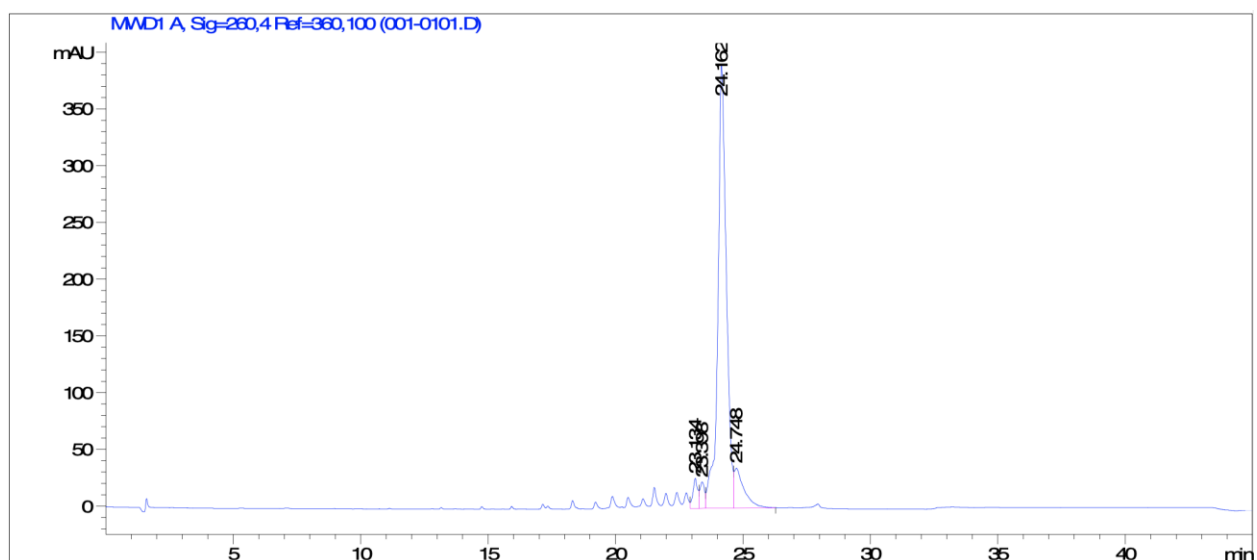


Figure S26. Analytical HPLC trace of unmodified siRNA antisense strand 5'-phos-UGGCGGACUUGAAGAAGUCGUGC[dT][dT] - 3'.

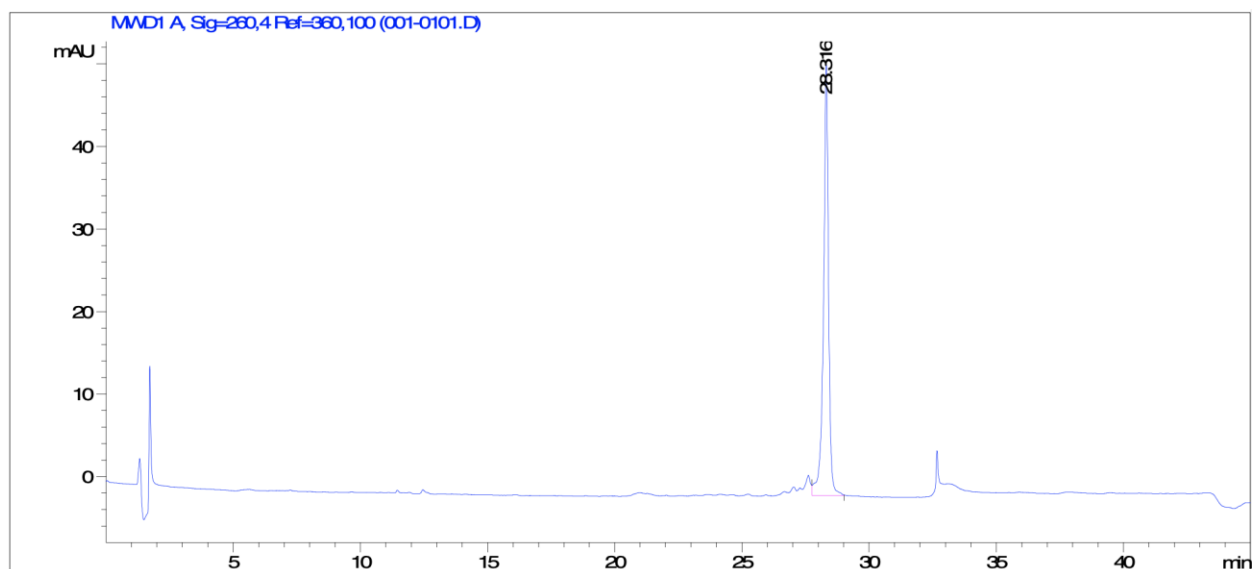


Figure S27. Analytical HPLC trace of fluorinated sense strand 5'-GCACGACUUCUUCAAGUCCGCCA[dT][dT]-3'.

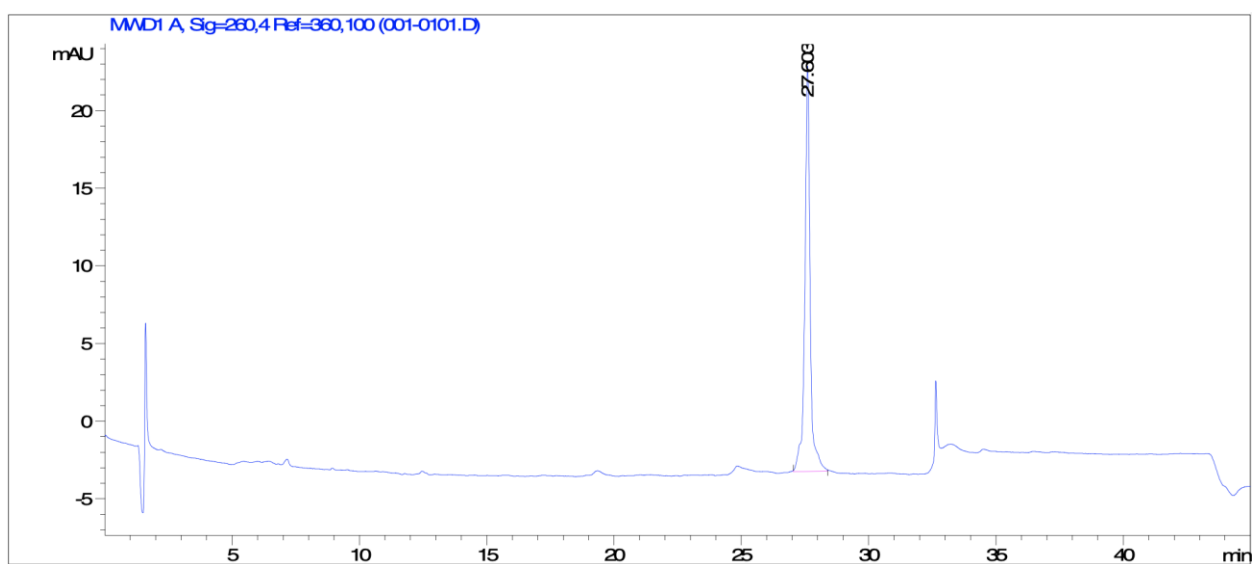


Figure S28. Analytical HPLC trace of fluorinated antisense strand 5'-phos-UGGCGGACUUGAAGAAGUCGUGC[dT][dT]-3'.

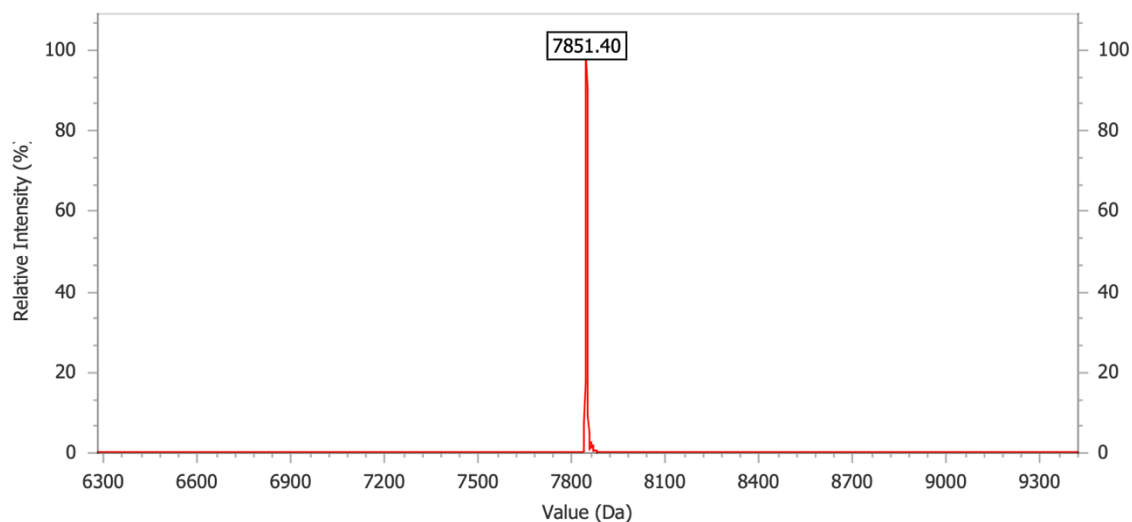


Figure S29. MS spectrum (ESI: MS-IALTQ-05) for unmodified siRNA sense strand 5'-GCACGACUUCUUCAAGUCCGCCA[dT][dT]-3'. Spectrum provided by IDT.

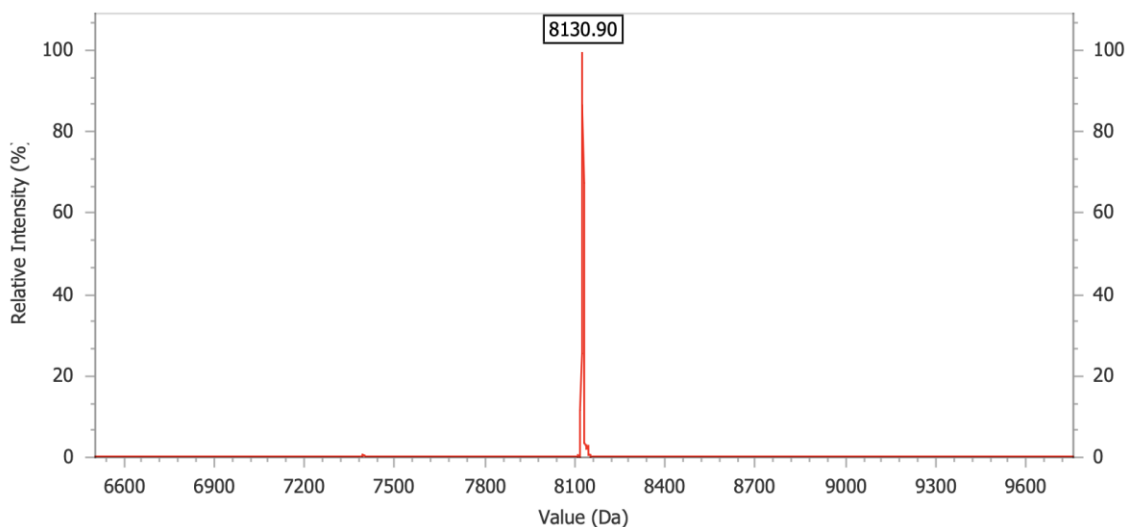


Figure S30. MS spectrum (ESI: MS-IALTQ-05) for unmodified siRNA antisense strand 5'-phos-UGGCGGACUUGAAGAAGUCGUGC[dT][dT] - 3'. Spectrum provided by IDT.

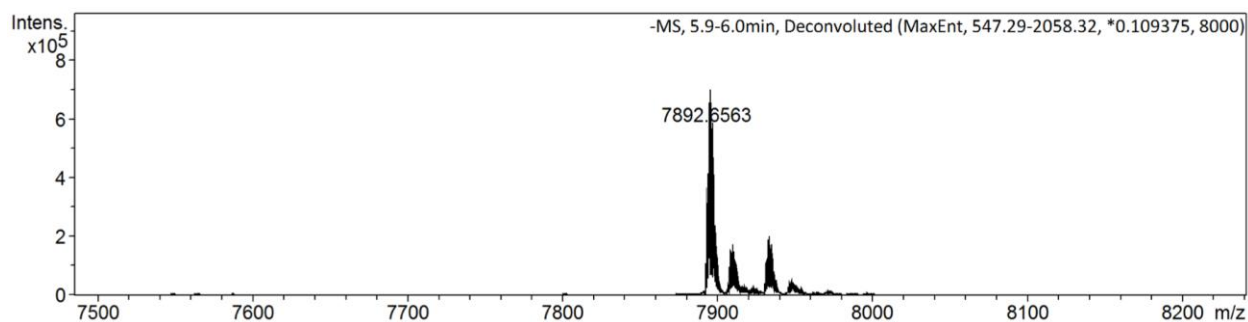


Figure S31. HRMS (ESI) of fluorinated siRNA sense strand 5'-GCACGACUUCUUCAAGUCCGCCA[dT][dT]-3'. Data was collected and analyzed by Dr. Alexander Wahba (McGill University)

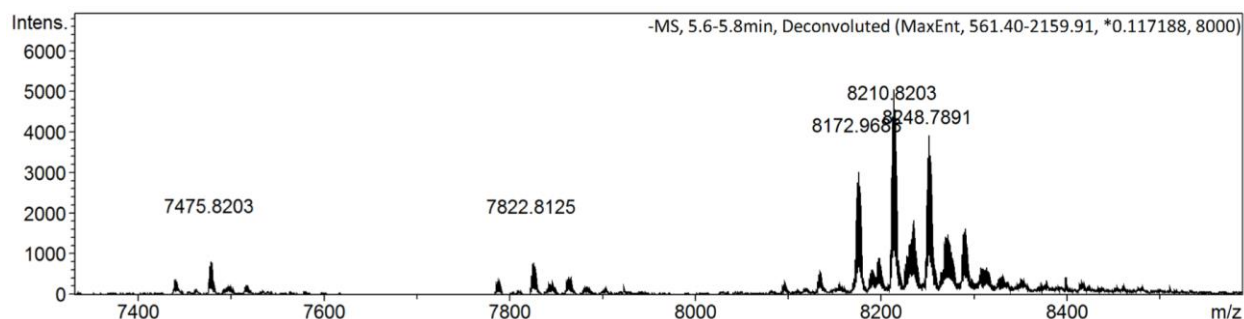


Figure S32. Deconvoluted HRMS (ESI) of fluorinated siRNA antisense strand 5'-phos-UGGCGGACUUGAAGAAGUCGUGC[dT][dT] - 3'. Spectrum shows the presence of potassium adducts in the gas phase. Data was collected and analyzed by Dr. Alexander Wahba (McGill University)

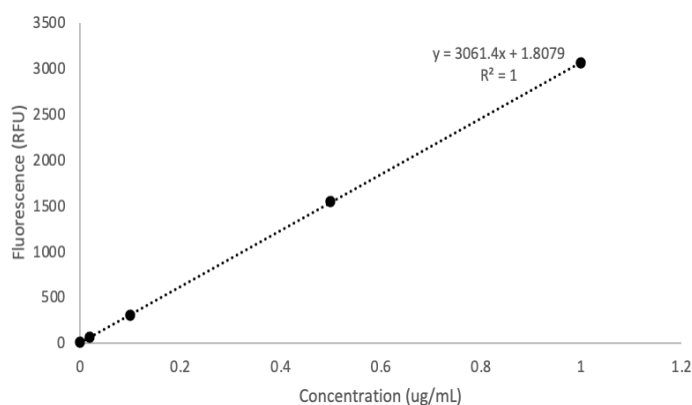


Figure S33. Standard curve for unmodified siRNA duplex generated using the RiboGreen Assay. Values are plotted concentration (µg/mL) vs fluorescence (RFU) at 530 nm.

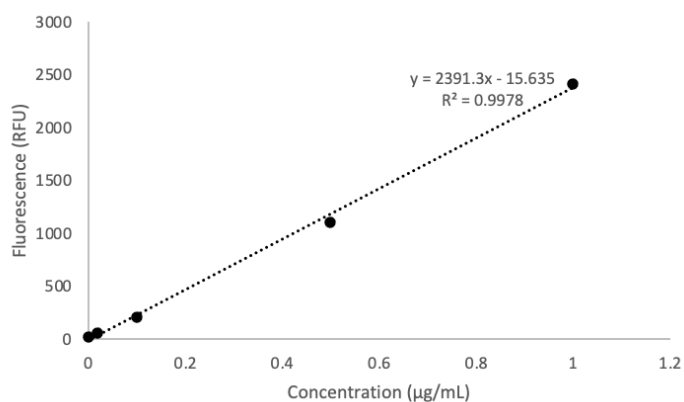


Figure S34. Standard curve for fluorinated siRNA duplex generated using the RiboGreen Assay. Values are plotted concentration (µg/mL) vs fluorescence (RFU) at 530 nm.

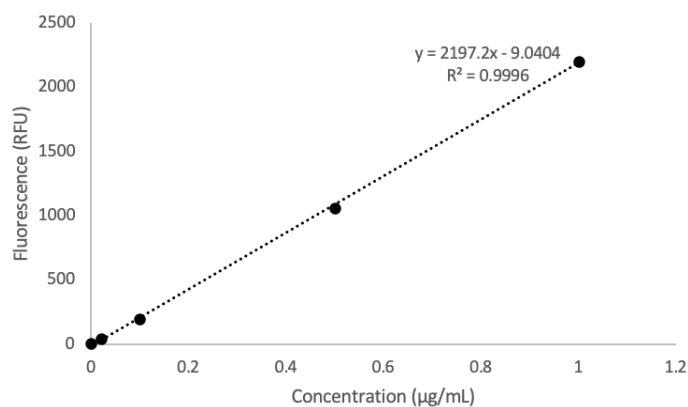


Figure S35. Standard curve for unmodified tRNA generated using the RiboGreen Assay. Values are plotted concentration (µg/mL) vs fluorescence (RFU) at 530 nm.

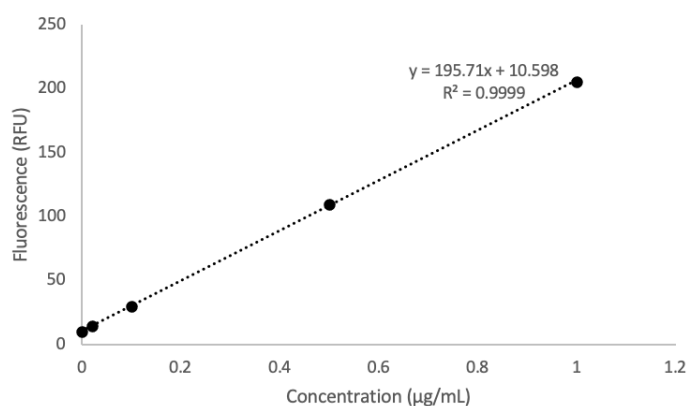


Figure S36. Standard curve for EMA-modified tRNA generated using the RiboGreen Assay. Values are plotted concentration (µg/mL) vs fluorescence (RFU) at 530 nm.

Table S37. DLS, PALS and encapsulation data for control liposomes encapsulating tRNA

Lipid	Diameter (nm)	Polydispersity	Zeta Potential (mV)	RNA encapsulation efficiency
MCLM (2)	146 ± 1.07	0.093 ± 0.023	-21 ± 6.02	80%
MCLP (3)	>1000	0.205 ± 0.077	N/A	N/A
MCLF (4)	137 ± 0.75	0.122 ± 0.011	-25 ± 6.62	52%
MCLH (5)	98 ± 0.93	0.212 ± 0.09	-32 ± 5.63	71%
MoChol (8)	107 ± 0.65	0.148 ± 0.003	-17 ± 9.76	81%

6. References

1. Igarashi, J.; Niwa, Y.; Sugiyama, D. Research and Development of Oligonucleotide Therapeutics in Japan for Rare Diseases. *Future Rare Diseases* **2022**, *2* (1).
2. Paunovska, K.; Loughrey, D.; Dahlman, J. E. Drug Delivery Systems for RNA Therapeutics. *Nature Reviews Genetics* **2022**, *23* (5), 265–280.
3. Yamada, Y. Nucleic Acid Drugs—Current Status, Issues, and Expectations for Exosomes. *Cancers* **2021**, *13* (19), 5002.
4. Hu, B.; Zhong, L.; Weng, Y.; Peng, L.; Huang, Y.; Zhao, Y.; Liang, X.-J. Therapeutic SiRNA: State of the Art. *Signal Transduction and Targeted Therapy* **2020**, *5* (1).
5. Fire, A.; Xu, S. Q.; Montgomery, M. K.; Kostas, S. A.; Driver, S. E.; Mello, C. C. Potent and Specific Genetic Interference by Double-Stranded RNA in *Caenorhabditis Elegans*. *Nature* **1998**, *391* (6669), 806–811.
6. Elbashir, S. M.; Harborth, J.; Lendeckel, W.; Yalcin, A.; Weber, K.; Tuschl, T. Duplexes of 21-Nucleotide RNAs Mediate RNA Interference in Cultured Mammalian Cells. *Nature* **2001**, *411* (6836), 494–498.
7. Martinez, J.; Patkaniowska, A.; Urlaub, H.; Lührmann, R.; Tuschl, T. Single-Stranded Antisense SiRNAs Guide Target RNA Cleavage in RNAi. *Cell* **2002**, *110* (5), 563–574.
8. Bernstein, E.; Caudy, A. A.; Hammond, S. M.; Hannon, G. J. Role for a Bidentate Ribonuclease in the Initiation Step of RNA Interference. *Nature* **2001**, *409* (6818), 363–366.
9. Setten, R. L.; Rossi, J. J.; Han, S.-ping. The Current State and Future Directions of Rnai-Based Therapeutics. *Nature Reviews Drug Discovery* **2019**, *18* (6), 421–446.
10. Setten, R. L.; Lightfoot, H. L.; Habib, N. A.; Rossi, J. J. Development of MTL-CEBPA: Small Activating RNA Drug for Hepatocellular Carcinoma. *Current Pharmaceutical Biotechnology* **2018**, *19* (8), 611–621.
11. Snead, N. M.; Wu, X.; Li, A.; Cui, Q.; Sakurai, K.; Burnett, J. C.; Rossi, J. J. Molecular Basis for Improved Gene Silencing by Dicer Substrate Interfering RNA Compared with Other Sirna Variants. *Nucleic Acids Research* **2013**, *41* (12), 6209–6221.
12. Hammond, S. M.; Bernstein, E.; Beach, D.; Hannon, G. J. An RNA-Directed Nuclease Mediates Post-Transcriptional Gene Silencing in *Drosophila* Cells. *Nature* **2000**, *404* (6775), 293–296.
13. Cifuentes, D.; Xue, H.; Taylor, D. W.; Patnode, H.; Mishima, Y.; Cheloufi, S.; Ma, E.; Mane, S.; Hannon, G. J.; Lawson, N. D.; Wolfe, S. A.; Giraldez, A. J. A Novel Mirna Processing Pathway Independent of Dicer Requires argonaute2 Catalytic Activity. *Science* **2010**, *328* (5986), 1694–1698.
14. Lee, H. Y.; Zhou, K.; Smith, A. M.; Noland, C. L.; Doudna, J. A. Differential Roles of Human Dicer-Binding Proteins TRBP and Pact in Small RNA Processing. *Nucleic Acids Research* **2013**, *41* (13), 6568–6576.

15. Whitehead, K. A.; Langer, R.; Anderson, D. G. Knocking down Barriers: Advances in Sima Delivery. *Nature Reviews Drug Discovery* **2009**, 8 (2), 129–138.
16. Urits, I.; Swanson, D.; Swett, M. C.; Patel, A.; Berardino, K.; Amgalan, A.; Berger, A. A.; Kassem, H.; Kaye, A. D.; Viswanath, O. A Review of Patisiran (ONPATTRO®) for the Treatment of Polyneuropathy in People with Hereditary Transthyretin Amyloidosis. *Neurology and Therapy* **2020**, 9 (2), 301–315.
17. Li, L.-C.; Okino, S. T.; Zhao, H.; Pookot, D.; Place, R. F.; Urakami, S.; Enokida, H.; Dahiya, R. Small Dsrnas Induce Transcriptional Activation in Human Cells. *Proceedings of the National Academy of Sciences* **2006**, 103 (46), 17337–17342.
18. Li, L.-C.; Dahiya, R. Modified Small Activating RNA Molecules and Methods of Use, March 29, 2016.
19. Sui, M.; Sakurai, F.; Elbashir, S.; Foster, D. J.; Manoharan, M.; Corey, D. R. Activation of LDL Receptor Expression by Small RNAS Complementary to a Noncoding Transcript That Overlaps the LDLR Promoter. *Chemical Biology* **2010**, 17 (12), 1344–1355.
20. Corey, D. R.; Shames, D. S.; Janowski, B. A.; Minna, J. D. Modulation of Gene Expression by Oligomers Targeted to Chromosomal DNA, December 4, 2012.
21. Kwok, A.; Raulf, N.; Habib, N. Developing Small Activating RNA as a Therapeutic: Current Challenges and Promises. *Therapeutic Delivery* **2019**, 10 (3), 151–164.
22. Weinmann, L.; Höck, J.; Ivacevic, T.; Ohrt, T.; Mütze, J.; Schwille, P.; Kremmer, E.; Benes, V.; Urlaub, H.; Meister, G. Importin 8 Is a Gene Silencing Factor That Targets Argonaute Proteins to Distinct Mnas. *Cell* **2009**, 136 (3), 496–507.
23. Schwartz, J. C.; Younger, S. T.; Nguyen, N.-B.; Hardy, D. B.; Monia, B. P.; Corey, D. R.; Janowski, B. A. Antisense Transcripts Are Targets for Activating Small RNAS. *Nature Structural & Molecular Biology* **2008**, 15 (8), 842–848.
24. Hicks, J. A.; Li, L.; Matsui, M.; Chu, Y.; Volkov, O.; Johnson, K. C.; Corey, D. R. Human GW182 Paralogs Are the Central Organizers for RNA-Mediated Control of Transcription. *Cell Reports* **2017**, 20 (7), 1543–1552.
25. Lu, G. D.; Leung, C. H. W.; Yan, B.; Tan, C. M. Y.; Low, S. Y.; Aung, M. O.; Salto-Tellez, M.; Lim, S. G.; Hooi, S. C. C/EBPA Is up-Regulated in a Subset of Hepatocellular Carcinomas and Plays a Role in Cell Growth and Proliferation. *Gastroenterology* **2010**, 139 (2).
26. Voutila, J.; Reebye, V.; Roberts, T. C.; Protopapa, P.; Andrikakou, P.; Blakey, D. C.; Habib, R.; Huber, H.; Saetrom, P.; Rossi, J. J.; Habib, N. A. Development and Mechanism of Small Activating RNA Targeting CEBPA, a Novel Therapeutic in Clinical Trials for Liver Cancer. *Molecular Therapy* **2017**, 25 (12), 2705–2714.
27. Reebye, V. Abstract LB-306: A Novel RNA Oligonucleotide Improves Liver Function and Inhibits Liver Carcinogenesis in Vivo. *Experimental and Molecular Therapeutics* **2013**.
28. Yang, W. Nucleases: Diversity of Structure, Function and Mechanism. *Quarterly Reviews of Biophysics* **2010**, 44 (1), 1–93.
29. Chu, L.-Y.; Hsieh, T.-J.; Golzarroshan, B.; Chen, Y.-P.; Agrawal, S.; Yuan, H. S. Structural Insights into RNA Unwinding and Degradation by RNase R. *Nucleic Acids Research* **2017**, 45 (20), 12015–12024.

30. Dupureur, C. M. One Is Enough: Insights into the Two-Metal Ion Nuclease Mechanism from Global Analysis and Computational Studies. *Metallomics* **2010**, 2 (9), 609.
31. Juliano, R.; Bauman, J.; Kang, H.; Ming, X. Biological Barriers to Therapy with Antisense and Sirna Oligonucleotides. *Molecular Pharmaceutics* **2009**, 6 (3), 686–695.
32. Shen, X.; Corey, D. R. Chemistry, Mechanism and Clinical Status of Antisense Oligonucleotides and Duplex RNAs. *Nucleic Acids Research* **2017**, 46 (4), 1584–1600.
33. Roberts, T. C.; Langer, R.; Wood, M. J. Advances in Oligonucleotide Drug Delivery. *Nature Reviews Drug Discovery* **2020**, 19 (10), 673–694.
34. Hu, B.; Zhong, L.; Weng, Y.; Peng, L.; Huang, Y.; Zhao, Y.; Liang, X.-J. Therapeutic Sirna: State of the Art. *Signal Transduction and Targeted Therapy* **2020**, 5 (1).
35. Phelps, K. J.; Ibarra-Soza, J. M.; Tran, K.; Fisher, A. J.; Beal, P. A. Click Modification of RNA at Adenosine: Structure and Reactivity of 7-Ethynyl- and 7-Triazolyl-8-Aza-7-Deazaadenosine in RNA. *ACS Chemical Biology* **2014**, 9 (8), 1780–1787.
36. Raines, R. T. Ribonuclease A. *Chemical Reviews* **1998**, 98 (3), 1045–1066.
37. Wu, S. Y.; Yang, X.; Gharpure, K. M.; Hatakeyama, H.; Egli, M.; McGuire, M. H.; Nagaraja, A. S.; Miyake, T. M.; Rupaimoole, R.; Pecot, C. V.; Taylor, M.; Pradeep, S.; Sierant, M.; Rodriguez-Aguayo, C.; Choi, H. J.; Previs, R. A.; Armaiz-Pena, G. N.; Huang, L.; Martinez, C.; Hassell, T.; Ivan, C.; Sehgal, V.; Singhanian, R.; Han, H.-D.; Su, C.; Kim, J. H.; Dalton, H. J.; Kovvali, C.; Keyomarsi, K.; McMillan, N. A.; Overwijk, W. W.; Liu, J.; Lee, J.-S.; Baggerly, K. A.; Lopez-Berestein, G.; Ram, P. T.; Nawrot, B.; Sood, A. K. 2'-Ome-Phosphorodithioate-Modified Sirnas Show Increased Loading into the RISC Complex and Enhanced Anti-Tumour Activity. *Nature Communications* **2014**, 5 (1).
38. Song, X.; Wang, X.; Ma, Y.; Liang, Z.; Yang, Z.; Cao, H. Site-Specific Modification Using the 2'-Methoxyethyl Group Improves the Specificity and Activity of Sirnas. *Molecular Therapy - Nucleic Acids* **2017**, 9, 242–250.
39. Deleavey, G. F.; Watts, J. K.; Alain, T.; Robert, F.; Kalota, A.; Aishwarya, V.; Pelletier, J.; Gewirtz, A. M.; Sonenberg, N.; Damha, M. J. Synergistic Effects between Analogs of DNA and RNA Improve the Potency of Sirna-Mediated Gene Silencing. *Nucleic Acids Research* **2010**, 38 (13), 4547–4557.
40. Frank, F.; Sonenberg, N.; Nagar, B. Structural Basis for 5'-Nucleotide Base-Specific Recognition of Guide RNA by Human AGO2. *Nature* **2010**, 465 (7299), 818–822.
41. Bangham, A. D.; Horne, R. W. Negative Staining of Phospholipids and Their Structural Modification by Surface-Active Agents as Observed in the Electron Microscope. *Journal of Molecular Biology* **1964**, 8 (5), 660–688.
42. Barenholz, Y. (C. Doxil® — the First FDA-Approved Nano-Drug: Lessons Learned. *Journal of Controlled Release* **2012**, 160 (2), 117–134.
43. Wood, H. FDA Approves Patisiran to Treat Hereditary Transthyretin Amyloidosis. *Nature Reviews Neurology* **2018**, 14 (10), 570–570.

44. Wang, Z.; Schmidt, F.; Weisblum, Y.; Muecksch, F.; Barnes, C. O.; Finkin, S.; Schaefer-Babajew, D.; Cipolla, M.; Gaebler, C.; Lieberman, J. A.; Oliveira, T. Y.; Yang, Z.; Abernathy, M. E.; Huey-Tubman, K. E.; Hurley, A.; Turroja, M.; West, K. A.; Gordon, K.; Millard, K. G.; Ramos, V.; Da Silva, J.; Xu, J.; Colbert, R. A.; Patel, R.; Dizon, J.; Unson-O'Brien, C.; Shimeliovich, I.; Gazumyan, A.; Caskey, M.; Bjorkman, P. J.; Casellas, R.; Hatzioannou, T.; Bieniasz, P. D.; Nussenzweig, M. C. mRNA Vaccine-Elicited Antibodies to SARS-COV-2 and Circulating Variants. *Nature* **2021**, 592 (7855), 616–622.
45. Tenchov, R.; Bird, R.; Curtze, A. E.; Zhou, Q. Lipid Nanoparticles—from Liposomes to Mrna Vaccine Delivery, a Landscape of Research Diversity and Advancement. *ACS Nano* **2021**, 15 (11), 16982–17015.
46. Sercombe, L.; Veerati, T.; Moheimani, F.; Wu, S. Y.; Sood, A. K.; Hua, S. Advances and Challenges of Liposome Assisted Drug Delivery. *Frontiers in Pharmacology* **2015**, 6.
47. Barba, A. A.; Bochicchio, S.; Dalmoro, A.; Lamberti, G. Lipid Delivery Systems for Nucleic-Acid-Based-Drugs: From Production to Clinical Applications. *Pharmaceutics* **2019**, 11 (8), 360.
48. Large, D. E.; Abdelmessih, R. G.; Fink, E. A.; Auguste, D. T. Liposome Composition in Drug Delivery Design, Synthesis, Characterization, and Clinical Application. *Advanced Drug Delivery Reviews* **2021**, 176, 113851.
49. Bhattacharjee, S. DLS and Zeta Potential – What They Are and What They Are Not? *Journal of Controlled Release* **2016**, 235, 337–351.
50. Lv, H.; Zhang, S.; Wang, B.; Cui, S.; Yan, J. Toxicity of Cationic Lipids and Cationic Polymers in Gene Delivery. *Journal of Controlled Release* **2006**, 114 (1), 100–109.
51. Neves, L. F.; Duan, J.; Voelker, A.; Khanal, A.; McNally, L.; Steinbach-Rankins, J.; Ceresa, B. P. Preparation and Optimisation of Anionic Liposomes for Delivery of Small Peptides and Cdna to Human Corneal Epithelial Cells. *Journal of Microencapsulation* **2016**, 33 (4), 391–399.
52. Semple, S. C.; Chonn, A.; Cullis, P. R. Interactions of Liposomes and Lipid-Based Carrier Systems with Blood Proteins: Relation to Clearance Behaviour in Vivo. *Advanced Drug Delivery Reviews* **1998**, 32 (1-2), 3–17.
53. Zylberberg, C.; Matosevic, S. Pharmaceutical Liposomal Drug Delivery: A Review of New Delivery Systems and a Look at the Regulatory Landscape. *Drug Delivery* **2016**, 23 (9), 3319–3329.
54. Nakhaei, P.; Margiana, R.; Bokov, D. O.; Abdelbasset, W. K.; Jadidi Kouhbanani, M. A.; Varma, R. S.; Marofi, F.; Jarahian, M.; Beheshtkhoo, N. Liposomes: Structure, Biomedical Applications, and Stability Parameters with Emphasis on Cholesterol. *Frontiers in Bioengineering and Biotechnology* **2021**, 9.
55. Noble, G. T.; Stefanick, J. F.; Ashley, J. D.; Kiziltepe, T.; Bilgicer, B. Ligand-Targeted Liposome Design: Challenges and Fundamental Considerations. *Trends in Biotechnology* **2014**, 32 (1), 32–45.
56. Han, Xiao-Jian.; Wei, Yong-Fang.; Wan, Yu-Ying.; Jiang, Li-Ping.; Zhang, Jian-Feng.; Xin, Hong-Bo. Development of a Novel Liposomal Nanodelivery System for Bioluminescence Imaging and Targeted Drug Delivery in erbb2-

- Overexpressing Metastatic Ovarian Carcinoma. *International Journal of Molecular Medicine* **2014**, 34 (5), 1225–1232.
57. Deshpande, P. P.; Biswas, S.; Torchilin, V. P. Current Trends in the Use of Liposomes for Tumor Targeting. *Nanomedicine* **2013**, 8 (9), 1509–1528.
 58. Wu, J. The Enhanced Permeability and Retention (EPR) Effect: The Significance of the Concept and Methods to Enhance Its Application. *Journal of Personalized Medicine* **2021**, 11 (8), 771.
 59. Degors, I. M.; Wang, C.; Rehman, Z. U.; Zuhorn, I. S. Carriers Break Barriers in Drug Delivery: Endocytosis and Endosomal Escape of Gene Delivery Vectors. *Accounts of Chemical Research* **2019**, 52 (7), 1750–1760.
 60. Singh, K.; Ejaz, W.; Dutta, K.; Thayumanavan, S. Antibody Delivery for Intracellular Targets: Emergent Therapeutic Potential. *Bioconjugate Chemistry* **2019**, 30 (4), 1028–1041.
 61. Behzadi, S.; Serpooshan, V.; Tao, W.; Hamaly, M. A.; Alkawareek, M. Y.; Dreaden, E. C.; Brown, D.; Alkilany, A. M.; Farokhzad, O. C.; Mahmoudi, M. Cellular Uptake of Nanoparticles: Journey inside the Cell. *Chemical Society Reviews* **2017**, 46 (14), 4218–4244.
 62. Hu, Y.-B.; Dammer, E. B.; Ren, R.-J.; Wang, G. The Endosomal-Lysosomal System: From Acidification and Cargo Sorting to Neurodegeneration. *Translational Neurodegeneration* **2015**, 4 (1).
 63. Karanth, H.; Murthy, R. S. Ph-Sensitive Liposomes-Principle and Application in Cancer Therapy. *Journal of Pharmacy and Pharmacology* **2007**, 59 (4), 469–483.
 64. Torchilin, V. P.; Zhou, F.; Huang, L. Ph-Sensitive Liposomes. *Journal of Liposome Research* **1993**, 3 (2), 201–255.
 65. Chu, C.-J.; Szoka, F. C. Ph-Sensitive Liposomes. *Journal of Liposome Research* **1994**, 4 (1), 361–395.
 66. Simões, S.; Slepishkin, V.; Düzgünes, N.; Pedroso de Lima, M. C. On the Mechanisms of Internalization and Intracellular Delivery Mediated by Ph-Sensitive Liposomes. *Biochimica et Biophysica Acta (BBA) - Biomembranes* **2001**, 1515 (1), 23–37.
 67. Vidal, M.; Hoekstra, D. In Vitro Fusion of Reticulocyte Endocytic Vesicles with Liposomes. *Journal of Biological Chemistry* **1995**, 270 (30), 17823–17829.
 68. Semple, S. C.; Akinc, A.; Chen, J.; Sandhu, A. P.; Mui, B. L.; Cho, C. K.; Sah, D. W.; Stebbing, D.; Crosley, E. J.; Yaworski, E.; Hafez, I. M.; Dorkin, J. R.; Qin, J.; Lam, K.; Rajeev, K. G.; Wong, K. F.; Jeffs, L. B.; Nechev, L.; Eisenhardt, M. L.; Jayaraman, M.; Kazem, M.; Maier, M. A.; Srinivasulu, M.; Weinstein, M. J.; Chen, Q.; Alvarez, R.; Barros, S. A.; De, S.; Klimuk, S. K.; Borland, T.; Kosovrasti, V.; Cantley, W. L.; Tam, Y. K.; Manoharan, M.; Ciufolini, M. A.; Tracy, M. A.; de Fougères, A.; MacLachlan, I.; Cullis, P. R.; Madden, T. D.; Hope, M. J. Rational Design of Cationic Lipids for siRNA Delivery. *Nature Biotechnology* **2010**, 28 (2), 172–176.
 69. Hafez, I. M.; Ansell, S.; Cullis, P. R. Tunable PH-Sensitive Liposomes Composed of Mixtures of Cationic and Anionic Lipids. *Biophysical Journal* **2000**, 79 (3), 1438–1446.
 70. Akinc, A.; Maier, M. A.; Manoharan, M.; Fitzgerald, K.; Jayaraman, M.; Barros, S.; Ansell, S.; Du, X.; Hope, M. J.; Madden, T. D.; Mui, B. L.; Semple, S. C.; Tam,

- Y. K.; Ciufolini, M.; Witzigmann, D.; Kulkarni, J. A.; van der Meel, R.; Cullis, P. R. The Onpattro Story and the Clinical Translation of Nanomedicines Containing Nucleic Acid-Based Drugs. *Nature Nanotechnology* **2019**, *14* (12), 1084–1087.
71. Wagner, A.; Habib, R.; Huber, H.; Saetrom, P.; Stovner, E.; Hossbach, M.; Krampert, M.; Vornlocher, H.-P. C/EBP Alpha saRNA Compositions and Methods of use, October 27, 2016.
 72. Cametti, M.; Crousse, B.; Metrangolo, P.; Milani, R.; Resnati, G. The Fluorous Effect in Biomolecular Applications. *Chem. Soc. Rev.* **2012**, *41* (1), 31–42.
 73. Gillis, E. P.; Eastman, K. J.; Hill, M. D.; Donnelly, D. J.; Meanwell, N. A. Applications of Fluorine in Medicinal Chemistry. *Journal of Medicinal Chemistry* **2015**, *58* (21), 8315–8359.
 74. Hagmann, W. K. The Many Roles for Fluorine in Medicinal Chemistry. *Journal of Medicinal Chemistry* **2008**, *51* (15), 4359–4369.
 75. Kaan, H. Y.; Ulaganathan, V.; Rath, O.; Prokopcová, H.; Dallinger, D.; Kappe, C. O.; Kozielski, F. Structural Basis for Inhibition of EG5 by Dihydropyrimidines: Stereoselectivity of Antimitotic Inhibitors Enastron, Dimethylenastron and Fluorastrol. *Journal of Medicinal Chemistry* **2010**, *53* (15), 5676–5683.
 76. Klein, E.; Ciobanu, M.; Klein, J.; Machi, V.; Leborgne, C.; Vandamme, T.; Frisch, B.; Pons, F.; Kichler, A.; Zuber, G.; Lebeau, L. “HFP” Fluorinated Cationic Lipids for Enhanced Lipoplex Stability and Gene Delivery. *Bioconjugate Chemistry* **2010**, *21* (2), 360–371.
 77. Gaucheron, J.; Boulanger, C.; Santaella, C.; Sbirrazzuoli, N.; Boussif, O.; Vierling, P. In Vitro Cationic Lipid-Mediated Gene Delivery with Fluorinated Glycerophosphoethanolamine Helper Lipids. *Bioconjugate Chemistry* **2001**, *12* (6), 949–963.
 78. Dalvit, C.; Invernizzi, C.; Vulpetti, A. Fluorine as a Hydrogen-Bond Acceptor: Experimental Evidence and Computational Calculations. *Chemistry - A European Journal* **2014**, *20* (35), 11058–11068.
 79. Marshall, J. E.; Zhenova, A.; Roberts, S.; Petchey, T.; Zhu, P.; Dancer, C. E.; McElroy, C. R.; Kendrick, E.; Goodship, V. On the Solubility and Stability of Polyvinylidene Fluoride. *Polymers* **2021**, *13* (9), 1354.
 80. Sørensen, D. R.; Leirdal, M.; Sioud, M. Gene Silencing by Systemic Delivery of Synthetic SiRNAs in Adult Mice. *Journal of Molecular Biology* **2003**, *327* (4), 761–766.
 81. Danaei, M.; Dehghankhold, M.; Ataei, S.; Hasanzadeh Davarani, F.; Javanmard, R.; Dokhani, A.; Khorasani, S.; Mozafari, M. Impact of Particle Size and Polydispersity Index on the Clinical Applications of Lipidic Nanocarrier Systems. *Pharmaceutics* **2018**, *10* (2), 57.
 82. Barbosa, J. A. C.; Abdelsadig, M. S. E.; Conway, B. R.; Merchant, H. A. Using Zeta Potential to Study the Ionisation Behaviour of Polymers Employed in Modified-Release Dosage Forms and Estimating Their PKA. *International Journal of Pharmaceutics: X* **2019**, *1*, 100024.
 83. Joseph, E.; Singhvi, G. Multifunctional Nanocrystals for Cancer Therapy: A Potential Nanocarrier. *Nanomaterials for Drug Delivery and Therapy* **2019**, 91–116.

84. Samimi, S.; Maghsoudnia, N.; Eftekhari, R. B.; Dorkoosh, F. Lipid-Based Nanoparticles for Drug Delivery Systems. *Characterization and Biology of Nanomaterials for Drug Delivery* **2019**, 47–76.
85. van Swaay, D.; deMello, A. Microfluidic Methods for Forming Liposomes. *Lab on a Chip* **2013**, 13 (5), 752.
86. Hinna, A.; Steiniger, F.; Hupfeld, S.; Stein, P.; Kuntsche, J.; Brandl, M. Filter-Extruded Liposomes Revisited: A Study into Size Distributions and Morphologies in Relation to Lipid-Composition and Process Parameters. *Journal of Liposome Research* **2015**, 26 (1), 11–20.
87. Lou, G.; Anderluzzi, G.; Woods, S.; Roberts, C. W.; Perrie, Y. A Novel Microfluidic-Based Approach to Formulate Size-Tuneable Large Unilamellar Cationic Liposomes: Formulation, Cellular Uptake and Biodistribution Investigations. *European Journal of Pharmaceutics and Biopharmaceutics* **2019**, 143, 51–60.
88. Zook, J. M.; Vreeland, W. N. Effects of Temperature, Acyl Chain Length, and Flow-Rate Ratio on Liposome Formation and Size in a Microfluidic Hydrodynamic Focusing Device. *Soft Matter* **2010**, 6 (6), 1352.
89. Paiva, D.; Martín-Molina, A.; Cardoso, I.; Quesada-Pérez, M.; Pereira, M. do; Rocha, S. The Effect of a Fluorinated Cholesterol Derivative on the Stability and Physical Properties of Cationic DNA Vectors. *Soft Matter* **2013**, 9 (2), 401–409.
90. Soejima, T.; Iida, K.-ichiro; Qin, T.; Taniai, H.; Seki, M.; Takade, A.; Yoshida, S.-ichi. Photoactivated Ethidium Monoazide Directly Cleaves Bacterial DNA and Is Applied to PCR for Discrimination of Live and Dead Bacteria. *Microbiology and Immunology* **2007**, 51 (8), 763–775.
91. Botté, A.; Lainé, J.; Xicota, L.; Heiligenstein, X.; Fontaine, G.; Kasri, A.; Rivals, I.; Goh, P.; Faklaris, O.; Cossec, J.-C.; Morel, E.; Rebillat, A.-S.; Nizetic, D.; Raposo, G.; Potier, M.-C. Ultrastructural and Dynamic Studies of the Endosomal Compartment in Down Syndrome. *Acta Neuropathologica Communications* **2020**, 8 (1).
92. Rampersad, S. N. Multiple Applications of Alamar Blue as an Indicator of Metabolic Function and Cellular Health in Cell Viability Bioassays. *Sensors* **2012**, 12 (9), 12347–12360.
93. O'Brien, J.; Wilson, I.; Orton, T.; Pognan, F. Investigation of the Alamar Blue (Resazurin) Fluorescent Dye for the Assessment of Mammalian Cell Cytotoxicity. *European Journal of Biochemistry* **2000**, 267 (17), 5421–5426.
94. Ki, K. H.; Park, D. Y.; Lee, S. H.; Kim, N. Y.; Choi, B. M.; Noh, G. J. The Optimal Concentration of siRNA for Gene Silencing in Primary Cultured Astrocytes and Microglial Cells of Rats. *Korean Journal of Anesthesiology* **2010**, 59 (6), 403.
95. Inglut, C. T.; Sorrin, A. J.; Kuruppu, T.; Vig, S.; Cicalo, J.; Ahmad, H.; Huang, H.-C. Immunological and Toxicological Considerations for the Design of Liposomes. *Nanomaterials* **2020**, 10 (2), 190.

96. Ferguson, C. M.; Echeverria, D.; Hassler, M.; Ly, S.; Khvorova, A. Cell Type Impacts Accessibility of Mrna to Silencing by RNA Interference. *Molecular Therapy - Nucleic Acids* **2020**, 21, 384–393.